Synthesis of New Thermally Activated Delayed Fluorescence (TADF) Emitters

Synthese neuartiger Emitter mit thermisch aktivierter verzögerter Fluoreszenz (TADF)

TECHNISCHE
UNIVERSITÄT
DARMSTADT

Department of Chemistry
ERNST-BERL Institute for Technical and Macromolecular Chemistry
Technische Universität Darmstadt

for the Master's degree (M.Sc.)

Master-Thesis

Written by FELIX BERNT
born in Gelnhausen

Darmstadt 2020

First reviewer: Prof. Dr. Matthias Rehahn
Second reviewer: Dr. Jasper J. Michels

MAX PLANCK INSTITUTE
FOR POLYMER RESEARCH

This project was done under the supervision of Mr. Prof. Dr. Matthias Rehahn from September 2019 until March 2020 at the department of chemistry at Ernst-Berl-Institute for Technical and Macromolecular Chemistry. As a cooperation partner, Mr. Prof. Dr. Paul Blom and his group for molecular electronics agreed to supervise this project at Max Planck Institute for polymer-research (MPI-P) in Mainz during this time.

Acknowledgments

First of all, I want to thank Mr. Prof. Dr. REHAHN for supervising this master project despite his new position at the HELMHOLTZ research center for polymers in Geesthacht. I thank you for allowing me to realize this research project outside of the university and to take the next challenging step in my academic career.

Additionally, I want to thank Mr. Prof. Dr. BLOM and Mr. Dr. MICHELS from the MAX PLANCK Institute for polymer research (MPI-P) in Mainz. I had a really great time during my research internship and my master thesis in your group. It was an enormous pleasure for me to have such an opportunity in my early stages as a scientist. I was able to gain a lot of new experiences in the field of organic semiconductors, especially about thermally activated delayed fluorescence and fabrication of OLEDs. Also, I got to know so many new and beautiful people who will definitely stay in my memory. Of course, I am also very grateful to the whole team that supported me during my time at the MPI-P. On the one hand, the people who introduced me to the fabrication process of OLEDs, and on the other hand, the people who provided a pleasant working atmosphere in the lab. At this point, special thanks go to Ms. VERONA MAUS and Mr. OSKAR SACHNIK.

Furthermore, I would like to express a very, very big thank you to Mr. KAI PILIPPS, my supervisor in the laboratory. It was a really great time under your supervision, and I am so glad we got along so well. I was able to ask all my stupid questions, whether they were related to the topic or not. You always had an open ear for me and my problems and always suggested constructive solutions. Thank you very much, and I wish you all the best for the future, both for your further career and for your happy little family. Moreover, I would like to thank Mr. BAS VAN DER ZEE and Ms. ANIE RIBÉRIO, who taught me various analytical methods during KAI's absence. It was a great pleasure to meet you and very careful that you adopted me for this time.

A special thanks go to all my friends and my family who have supported me during my studies so far. Many thanks to Ms. FRANZISKA THEISS and Mr. ALEXANDER MACION, you have become terrific friends of mine, and I have enjoyed all the time we spent together since our first meeting. All our experiences together and the time spent in the lab courses mean a lot to me, and I hope that we can maintain our friendship after this time, even if I will go to another place. Thank you very much for all your valuable advice and time together.

My biggest thanks go my better half, LISA. I am so happy that we have found together and we could solve all our problems in the past despite our long-distance relationship. You mean so much to me, and I look forward to our future together with a bright smile. Whenever I have to go through a difficult time, you are there for me and support me with all your loving way. I love you, my darling.

Zusammenfassung

Im Zuge der Entwicklung immer effizienterer Materialien für organische Leuchtdioden (OLEDs, *organic light-emitting diodes*) setzte ADACHI im Jahr 2012 erstmals solche Emittermaterialien ein, die das Prinzip der thermisch aktivierten, verzögerten Fluoreszenz (TADF, *thermally activated delayed fluorescence*) zur Erzeugung von Licht nutzen.[1] Die Synthese solcher Materialien stellt indessen eine große Herausforderung dar, da es aktuellen Forschungsarbeiten kaum gelingt die drei großen Schlagworte Effizienz, Lebensdauer und Farbe in nur einem einzigen Molekül zu vereinen.[2] Allerdings gelang es der Arbeitsgruppe von LU im Jahr 2017 die folgenden zwei kleinen Moleküle (Abbildung 0.1) herzustellen, welche sehr viele Anforderungen an einen TADF Emitter erfüllen.[3]

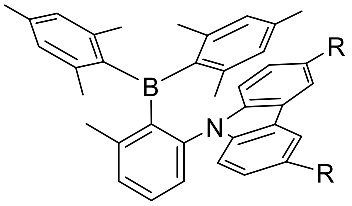

B-oCz (**8a**) R = H
B-oTC (**8b**) R = *tert*-butyl

Abbildung 0.1: Die zwei kleinen Moleküle B-oCz (**8a**) und B-oTC (**8b**), welche als blaue TADF-Emitter eingesetzt werden können.

Zu Beginn dieser Arbeit wurden die unterschiedlichen Energieniveaus beider Moleküle **8a** und **8b** mittels der (zeitabhängigen-) Dichtefunktionaltheorie (TD-DFT, *time-dependent density functional theory*) auf dem B3LYP/6-31G(d) Level der Theorie berechnet. Die daraus resultierenden Ergebnisse wurden im folgenden Energiediagramm zusammengefasst (Abbildung 0.2).

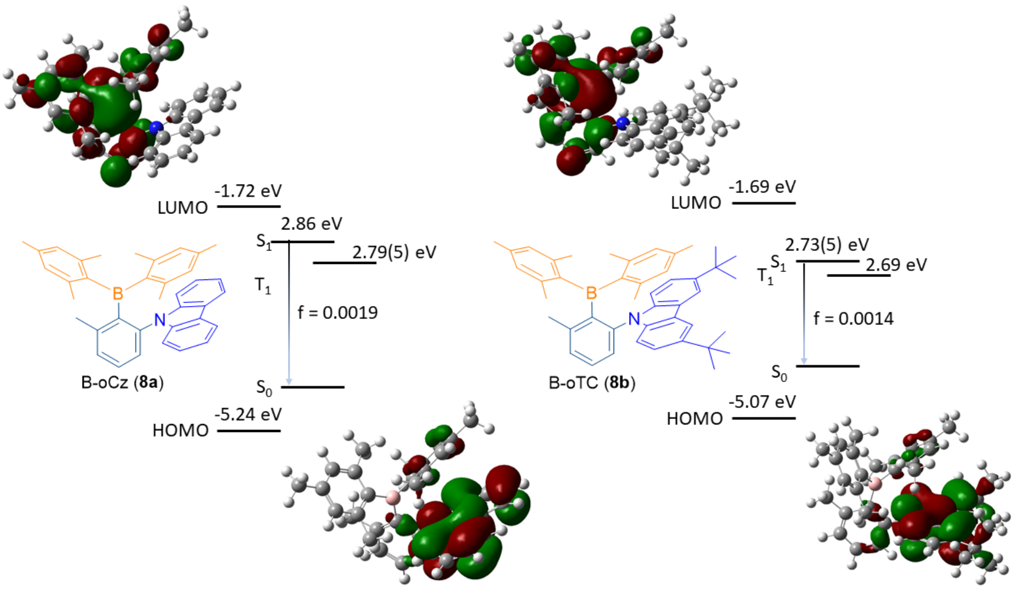

Abbildung 0.2: Energiediagramm der kleinen Moleküle B-oCz (**8a**) und B-oTC (**8b**).

Wie diesem Energiediagramm zu entnehmen ist, konnte für die niedrigen Singulet und Triplet Zustände beider Moleküle ein Energieunterschied (ΔE_{ST}) kleiner als 0.1 eV ermittelt werden. Somit wurde ein erstes Anzeichen für TADF Eigenschaften mit theoretischen Berechnungen nachgewiesen. Zusätzlich stellt der Donor-Akzeptor Aufbau der Moleküle eine häufig angewandte Designmethode von TADF Emittern dar. Dieser Molekülaufbau ermöglichte eine Separierung des höchsten besetzten Molekülorbitals (HOMO, *highest occupied molecular orbital*) von dem niedrigsten unbesetzten Molekülorbitals (LUMO, *lowest occupied molecular orbital*)[4], welche ebenfalls in Abbildung 0.2 zu erkennen ist.

Da B-oCz (**8a**) und B-oTC (**8b**) sehr vielversprechende Kandidaten für neue, auf Polymer basierenden TADF Emittermaterialien sind, wurden beide kleine organische Moleküle in einer zweistufigen Synthese hergestellt. Im Rahmen der Synthese konnten moderate Gesamtausbeuten von knapp 25 % bei sehr hohen Reinheiten für beide Moleküle erhalten werden. Mit Hilfe von UV/Vis Spektren, Photolumineszenz (PL, *photoluminescence*) Spektren und der photolumineszenten Quantenausbeute (PLQY, *photoluminescent quantum yield*) wurden **8a** und **8b** sowohl in sauerstoff-freiem Toluol als auch in Filmen auf einem Quarz Substrat unter Sauerstoffausschluss charakterisiert. Hier konnten die Ergebnisse der Literatur[3] annähernd bestätigt werden. Lediglich die PLQY der Moleküle auf den Quarz Substraten spiegelte diese Ergebnisse nicht wider.

Für eine Verwendung in den ersten eigenständig hergestellten OLEDs mussten B-oCz (**8a**) und B-oTC (**8b**) sublimiert werden. Um später eine Referenz für polymerbasierte OLEDs zu erhalten, wurden beide Moleküle **8a** und **8b** in unterschiedlichen Bauteilen für die OLEDs getestet. Dazu zählten Bauteile, welche nur eine Art von Ladungstransport untersuchen (*hole-only devices* und *electron-only devices*) und schließlich auch die OLEDs selbst. Des Weiteren konnte ein Vergleich zwischen lösungs-prozessierten und thermisch aufgedampften Bauteilen angefertigt und der Aufbau von thermisch aufgedampften OLEDs variiert werden. Allerdings erreichten alle hergestellten Bauteile nicht die in der Literatur[3] angegebenen Effizienzen, sodass an dieser Stelle noch weiterer Optimierungsbedarf besteht.

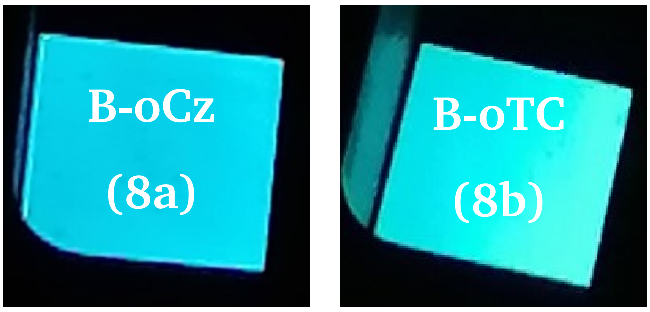

Abbildung 0.3: Fotographie einzelner Pixel der selbst hergestellten OLEDs. **Links:** B-oCz (**8a**) als Emitter. **Rechts:** B-oTC (**8b**) als Emitter.

Da kleine organische Moleküle im Allgemeinen sehr schwer zu einer OLED verarbeitet werden können, lag der Fokus dieser Arbeit auf der Synthese dieser beiden ausgewählten Moleküle und das weitere Umsetzen zu einem Polymer. Für die Synthese des Polymers wurden aufgrund der einfachen Realisierung folgende Polymerarchitekturen aus einer Vielzahl an literaturbekannten Architekturen[5–9] ausgewählt (Abbildung 0.4).

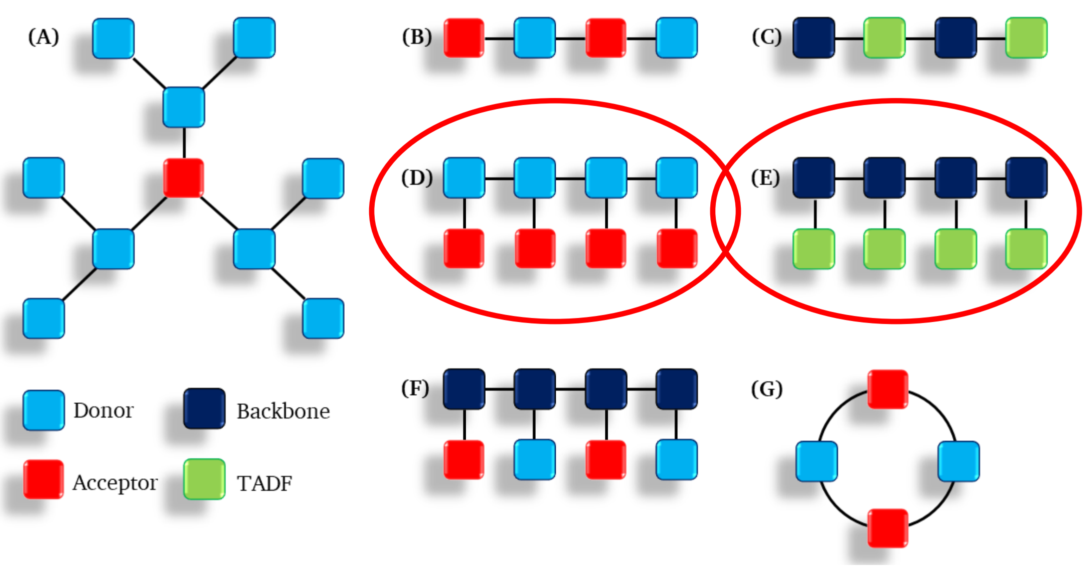

Abbildung 0.4: Unterschiedliche literaturbekannte Polymerarchitekturen[5–9]. Rote Markierung: ausgewählte Zielstrukturen für die zu synthetisierenden Polymere.

Der Realisierung beider ausgewählten Polymerarchitekturen (**D**) und (**E**) ging eine Halogenierung von B-oCz (**8a**) und B-oTC (**8b**) voraus. Anschließend wurde versucht mittels einer SUZUKI Kreuzkupplungsreaktion eine polymerisierbare Einheit an die beiden Moleküle zu knüpfen, um ein nicht-konjugiertes Polymerrückgrat mit den TADF-Einheiten in der Seitenkette zu erhalten (**E**). Für Variante **D** mit dem konjugierten Donorrückgrat und Akzeptoreinheiten in der Seitenkette stellte die YAMAMOTO-Kondensationsreaktion eine aussichtsreiche Methode dar. Allerdings zeigte sich an dieser Stelle nur die Dibromierung von B-oCz (**8a**) vielversprechend, sodass nur eine Polymerarchitektur nach dem Vorbild von **D** realisiert werden konnte. In Kooperation mit Prof. Dr. KLAUS MÜLLEN vom MPI-P und Dr. DIETER SCHOLLMEYER von der JOHANNES GUTENBERG-UNIVERSITÄT Mainz konnte zusätzlich die Kristallstruktur des entsprechenden Monomer (B-oCz)-4,9-Br_2 mittels Röntgenkristallstrukturanalyse erfolgreich ermittelt werden. Im Rahmen der Charakterisierung des erhaltenen Polymers aus der YAMAMOTO Kondensationsreaktion konnte festgestellt werden, dass es sich bei den Molekülen um ringförmige Strukturen (Makrozyklen) handelt, welche bis zu 18 Wiederholungseinheiten enthalten.

Zusätzlich wurde das erhaltene Polymer mit Hilfe von (TD-)DFT Berechnungen simuliert und es konnte gezeigt werden, dass sowohl die Energielücke zwischen den Singulet und Triplet Zuständen (ΔE_{ST}) noch immer unter 0.1 eV liegt als auch, dass HOMO und LUMO ebenfalls auf Donor und Akzeptor verteilt bleiben. Allerdings wurde die Energie des HOMOs im Zuge der Kondensationsreaktion durch die Konjugation angehoben, sodass sich ein Farbwechsel der Fluoreszenz von blau nach grün ergab. Nichtsdestotrotz wurde das erhaltene Poly-**8a**-cy mittels UV/Vis- und PL-Spektren charakterisiert und die PLQY ermittelt. Hier bestätigte sich der Farbwechsel der Fluoreszenz von blau nach grün durch die unterschiedlichen Maxima im PL Spektrum. Weiterhin konnte eine Verringerung der PLQY beobachtet werden. Mittels Messungen des PL Spektrums in verschiedenen Lösungsmitteln unterschiedlicher Polarität wurden die solvatochrome Eigenschaften des Polymers bestätigt, welcher ein weiteres Indiz für TADF Eigenschaften ist. Weitere Untersuchungen der Eigenschaften und der Bestätigung der TADF-Eigenschaften mit Hilfe temperatur- und zeitabhängiger Spektroskopie von Poly-**8a**-cycle konnten im Rahmen dieser Arbeit aus zeitlichen Gründen nicht mehr durchgeführt werden.

Summary

In the progress of the development of more and more efficient materials for organic light-emitting diodes (OLEDs), ADACHI and his coworkers used such emitter materials for the first time in 2012, which use the principle of thermally activated delayed fluorescence (TADF) to generate light.[1] However, the synthesis of such materials is a great challenge since current research is hardly going to succeed in combining the three important properties efficiency, lifetime, and color in a single molecule.[2] Nevertheless, in 2017 LU and his coworkers succeeded in synthesizing the following two organic small molecules, which satisfy a variety of requirements for a TADF emitter (Figure 0.1).[3]

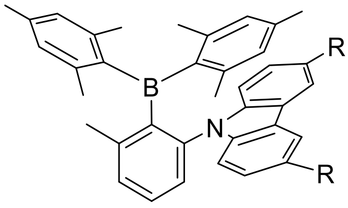

B-oCz (**8a**) R = H
B-oTC (**8b**) R = *tert*-butyl

Figure 0.1: The two small molecules B-oCz (**8a**) and B-oTC (**8b**), which can be used as blue TADF emitters.

For the first part of this work, the different energy levels of both molecules **8a** and **8b** were calculated using the (time-dependent) density functional theory (TD-DFT) at the B3LYP/6-31G(d) level. The corresponding results are shown in the following energy diagram (Figure 0.2).

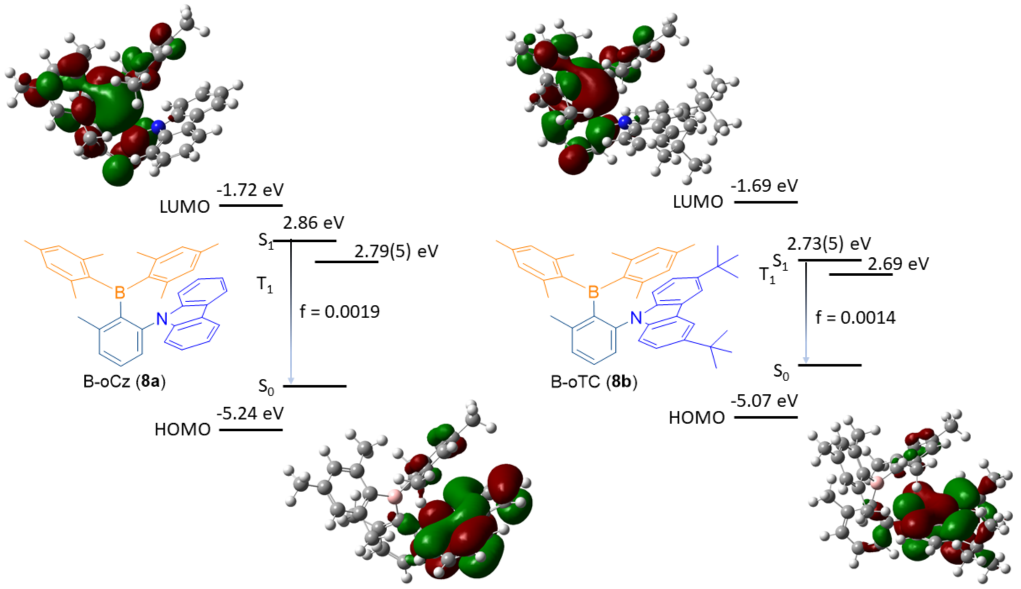

Figure 0.2: Energy diagram of the small molecules B-oCz (**8a**) and B-oTC (**8b**).

As can be seen from this energy diagram, an energy difference (ΔE_{ST}) of less than 0.1 eV could be determined for the low singlet and triplet states of both molecules. Thus, a first indication of TADF properties had been proven by theoretical calculations. Also, the donor-acceptor structure of the molecules is a frequently used design strategy of TADF emitters. This design strategy allowed a separation of the highest occupied molecular orbital (HOMO) from the lowest unoccupied molecular orbital (LUMO)[4], which is also shown in Figure 0.2.

Being up-and-coming candidates for new polymer-based TADF emitter materials, B-oCz (**8a**) and B-oTC (**8b**) were prepared in a two-step synthesis. During the synthesis, moderate overall yields of almost 25 % and very good purities for both molecules were obtained. Using UV/Vis spectra, photoluminescence (PL) spectra and photoluminescent quantum yield (PLQY), **8a,** and **8b** were characterized in oxygen-free toluene as well as in films on a quartz substrate under oxygen-free conditions. Here the results of the literature[3] could be approximately confirmed. Only the PLQY of the molecules on the quartz substrates did not reflect these results.

In order to use them in the first self-made OLEDs, B-oCz (**8a**) and B-oTC (**8b**) had to be sublimated. To later provide a reference for polymer-based OLEDs, both small molecules **8a** and **8b** were tested in different devices for OLEDs. These included hole-only devices (HOD) and electron-only devices (EOD) that investigate only one type of charge transport and, finally, the OLEDs themselves. Furthermore, a comparison between solution-processed and thermally-evaporated devices was made and the structure of thermally-deposited OLEDs was varied. However, all manufactured components did not reach the efficiencies reported in the literature[3], so that there is still a need for further optimization at this point.

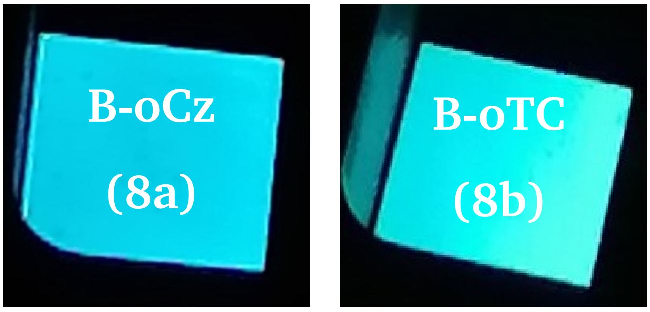

Figure 0.3: Photographs of single pixels of self-made OLEDs. **Left**: B-oCz (**8a**) as emissive layer. **Right:** B-oTC (**8b**) as emissive layer.

Since small organic molecules are generally complicated to process into an OLED, the work focused on the synthesis of these two selected molecules and their further implementation into a polymer. For the synthesis of the polymers, the following polymer architectures were selected from a large number of polymer architectures known from the literature[5–9] due to their simple realization (Figure 0.4).

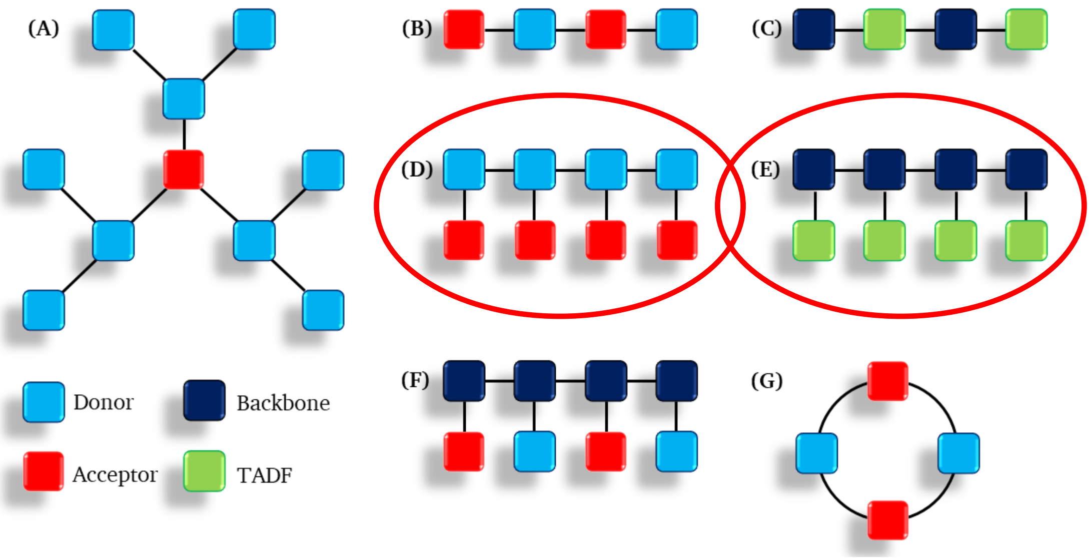

Figure 0.4: Different polymer architectures known from the literature. [5–9] Red cycles: chosen polymer architectures for the target polymers of this work.

The realization of both selected polymer architectures **D** and **E** was preceded by halogenation of B-oCz (**8a**) and B-oTC (**8b**). Subsequently, a SUZUKI cross-coupling reaction was attempted to attach a polymerizable group to the two molecules in order to obtain a non-conjugated polymer backbone with the TADF property in the side chain (**E**). For purpose **D** and the conjugated donor backbone with acceptor units in the side chain, the YAMAMOTO condensation reaction was a promising method. However, only the dibromination of B-oCz (**8a**) appeared to be promising at this point, so that only a polymer architecture modeled on **D** could be obtained. In collaboration with Prof. Dr. KLAUS MÜLLEN of the MPI-P and Dr. DIETER SCHOLLMEYER of the JOHANNES GUTENBERG-UNIVERSITY of Mainz, the crystal structure of the monomer (B-oCz)-4,9-Br_2 could be successfully determined using X-ray crystal structure analysis. During the characterization of the polymer obtained from the YAMAMOTO condensation reaction, it could be determined that the molecule has a ring-shaped structure containing up to 18 repeating units. Also, the obtained polymer was simulated by (TD-)DFT calculations, and it could be shown that the energy gap between the singlet and the triplet states (ΔE_{ST}) is still below a value of 0.1 eV and HOMO and LUMO also remained distributed between donor and acceptor. However, the energy of HOMO was increased by the conjugation during the condensation reaction, resulting in a color change of the fluorescence from blue to green.

Nevertheless, the obtained Poly-**8a**-cy was characterized by UV/Vis, and PL spectra and the PLQY is determined, too. Here, the color change of the fluorescence from blue to green was confirmed by the different maxima in the PL spectrum. Furthermore, a reduction of the PLQY could be observed. By measuring the PL spectrum in several solvents of different polarities, a solvatochroism of the polymer could be confirmed, which is another indication for TADF properties. Further investigations of the properties and the confirmation of TADF properties using temperature and time-dependent spectroscopy of Poly-**8a**-cy was not performed in this work due to time constraints.

Table of contents

I List of abbreviations

abbreviation	meaning	unit
μ_p	Hole mobility	
$\epsilon_0\epsilon_r$	Permittivity of polymer	
μ_0	Electron mobility	
4BpinSt	4,4,5,5-tetramethyl-2-(4-vinylphenyl)-1,3,2-dioxaborolane	
A	ARRHENIUS parameter	
AFM	Atomic force microscopy	
Alq_3	8-hydroxyquinoline aluminum	
B-oCz	9-(2-(dimesitylboraneyl)-3-methylphenyl)-9*H*-carbazole	
B-oTC	3,6-di-*tert*-butyl-9-(2-(dimesitylboraneyl)-3-methylphenyl)-9*H*-carbazole	
Br-oCz	9-(2-bromo-3-methylphenyl)-9*H*-carbazole	
Br-oF	2-bromo-3-fluorotoluene	
Br-oTC	9-(2-bromo-3-methylphenyl)-3,6-di-*tert*-butyl-9*H*-carbazole	
CT	Charge-transfer	
DCM	Dichloromethane	
DMF	Dimethylformamide	
DMF	Dimethylformamide	
DPEPO	(oxybis(2,1-phenylene))bis(diphenylphosphine oxide)	
e	Electron charge	
EBL	Electron-blocking layer	
E_{ex}	Exchange energy	
EIL	Electron-injection layer	
EL	electroluminescence	
EML	Emissive layer	
EO	Electron-only	
EOD	Electron-only device	
E_{orb}	Orbital energy	
EQE	External quantum efficiency	
E_{S1}	Energy of lowest singlet excited state	
E_{T1}	Energy of lowest triplet excited state	
ETL	Electron-transport layer	
ExTET	Exciplex-triplet-energy-transfer	

f	Oscillator length	
FWHM	Full width at half-maximum	
GPC	Gel-permeations chromatography	
HBL	Hole-blocking layer	
HIL	Hole-injection layer	
HO	Hole-only	
HOD	Hole-only device	
HOMO	Highest occupied molecular orbital	
HTL	Hole-transport layer	
IC	Internal conversion	
ICT	Intramolecular charge transfer	
ILC	Injection limited current	
IQE	Internal quantum efficiency	
ISC	Intersystem-crossing-process	
ITO	Indium-tin-oxide	
J	Current-density	A/m^2
K	Electron repulsion energy	
k_B	BOLTZMANN constant	
k_{rISC}	Rate of reverse intersystem crossing	
L	Thickness of layer	Nm
LCDs	Liquid crystal displays	
LED	Light-emitting diode	
LUMO	Lowest unoccupied molecular orbital	
MALDI	Matrix-assisted laser desorption ionization	
Mes_2BF	Fluoro-dimesitylborane	
n_0	Equilibrium electron density	
NBS	N-bromo-succinimide	
N_c	Effective density of states in the conduction band	
NIS	N-iodo-succinimide	
NMR	Nuclear magnetic resonance	
N_t	Total density of traps	
OLED	(organic) light-emitting diode	
PEDOT:PSS	Poly-(3,4-ethylenedioxythiophene)-poly-(styrenesulfonate)	
PL	Photoluminescence	
PLEDs	Polymer light-emitting diodes	

PLQY	Photoluminescence quantum yield	
PPV	Poly(*para*-phenylene vinylene)	
pTFF	Poly-(9,9-dioctylfluorene-2,7-diyl-1,4-phenylene-N-(*para*-trifluorophenyl)imino-1,4-phenylene)	
QE	Quantum efficiency	
r	Radius	
S	Overall spin	
S_1	First excited singlet state	
SCLC	Space charge limited current	
S_H	Host singlet	
SMOLEDs	Small molecule organic light-emitting diodes	
T	Temperature	
T_1	First excited triplet state	
TADF	Thermally activated delayed fluorescence	
TFB	Poly(9,9-dioctylfluorene-2,7-diyl-1,4-phenylene-N-(*para*-sec-butylphenyl)imino-1,4-phenylene)	
T_G	Guest triplet	
T_H	Host triplet	
TLC	Thin-layer chromatography	
TmPyPB	3,3'-(5'-(3-(pyridine-3-yl)phenyl-[1,1',3',1"-terphenyl]-3,3"-diyl)dipyridine	
TmPyTZ	2,4,6-tris(3-(pyridine-3-yl)phenyl)-1,3,5-triazine	
TOF	Time-of-flight	
TPBi	2,2',2"-(1,3,5-Benzinetryl)-tris(1-phenyl-1-*H*-benzinimidazole)	
TSCT	Through-space charge-transfer	
TTA	Triplet-triplet annihilation	
UV/Vis	Ultraviolet/visible	
V	Voltage	V
V_{crit}	Critical voltage	V
ΔE_{ST}	Energy gap between singlet and triplet excited states	
φ	Wavefunction of LUMO	
Φ	Wavefunction of HOMO	
Φ_{B}	Energy barrier without the energy of SCHOTTKY barriers	
Φ_{Inj}	Energy barrier of injection	

II List of figures

III List of schemes

IV List of tables

1 Introduction

Nowadays, displays can be found everywhere around us. Being in screens for smartphones, televisions, or computers, everyone uses them in their daily life. These wide spread applications, as we know it today, would never be possible without the discovery of electrical conductivity of polyacetylene in 1977 by HEEGER, MACDIARMID, and SHIRAKAWA.[10] As a property of a silvery film, which was under exposure to halogens iodine, bromine or chlorine, *trans* polyacetylene could achieve a high conductivity up to 10^5 S/m. For their work, these three scientists achieved the Nobel prize for chemistry in the year 2000.[11] Although this material cannot be used for commercial applications, polyacetylene was a massive inspiration for the development of organic and inorganic display materials.

Nevertheless, the first organic light-emitting diode (OLED) was developed by TANG and VANSLYKE in 1987.[12] They were using a simple two-layer diode on glass with 8-hydroxyquinoline aluminum (Alq_3) as an emissive layer. Alq_3 is a small molecule that was used in green OLEDs with an internal quantum efficiency of around 32 %. Due to light outcoupling effects of around 20 %, an external quantum efficiency of around 6 % is possible at its maximum.[13] With this new development, every pixel of an OLED can be self-luminescent and does not need a backlight. The main problems of OLEDs based on small molecules (SMOLEDs) are the fabrication and stability of such devices. SMOLEDs are mainly fabricated by using thermal deposition methods. The inefficiency of these methods is caused by their high costs and the fact that not all components can reach the substrate. Another way in the fabrication of SMOLEDs is the usage of printable materials. Therefore, dissolved single components are applied with a syringe, and after evaporation of the solvent, they are fixed on the surface. Hydrophobic polyimide walls are used for the separation of the droplets from each other to form single pixels on the substrate. Unfortunately, this method is too complicated for commercial usage.[14]

In 1990, the first OLEDs based on polymers (PLEDs) were used by BURROUGHES and his group. They used dichloro-*para*-xylene as a starting material for the polymerization from a sulphonium salt intermediate to achieve poly(*para*-phenylene vinylene) (PPV). PPV can be used as a green-yellow emitter material for OLEDs with a photoluminescence quantum yield of around 8 %, which can be easily spin-coated for device fabrication.[15] In comparison to SMOLEDs, there are several advantages of using PLEDs for LED fabrication. Polymers can be easily solution-processed by spin-coating on the substrates, which is much cheaper than thermal evaporation. Furthermore, PLEDs are very flexible due to their physical properties, which makes them ideal for mobile applications.[16]

In comparison with liquid crystal displays (LCDs), OLEDs are much thinner and lighter (~500 nm).[17] In addition to these advantages, OLEDs have better energy efficiencies, because they do not use backlight like LCDs. Furthermore, OLEDs can achieve higher contrasts because they are using their pixels only if it is necessary. Further advantages of OLEDs in comparison with LCDs are flexibility, lower electricity consumption, wider viewing angles, better response times, and color reproduction.[18]

Despite many advantages of OLEDs compared to LCDs, they still have decisive disadvantages. Besides the production and the resulting costs, the lifetime of OLEDs is a significant drawback. Red and green OLEDs have a lifetime between 20000 – 22000 h at a luminance of 1000 – 500 cd/m^2. In contrast, blue OLEDs have a lifetime of only about 1000 h at a luminance of 200 cd/m^2. However, the lifetime is temperature-dependent, so the real values should be significantly lower at higher loads.[14]

Despite the mentioned disadvantages of LCD technology, it is the market leader. However, it is expected that OLED displays will take over the market leader within the next decade and increasingly displace LCDs from the market.[19] Although SMOLEDs are more expensive to manufacture than PLEDs, available commercial OLEDs are usually based on small molecules.[20] As there is currently a lack of long-term stable materials in the field of PLEDs, current research work is focusing on their development and establishment of the technology market. For this purpose, not only known polymer classes such as PPV are investigated and optimized, but also new easily accessible and processable materials are sought. Especially the development of stable, highly efficient blue polymeric emitter materials is highly topical and the focus of the present work.

In principle, an organic light-emitting diode (OLED) consists of an organic semiconductor layer between two electrodes. To increase the efficiency of the OLED, additional layers are required. The most important functional layers are the emissive layer (EML, blue), the hole-transport layer (HTL, orange), and the electron-transport layer (ETL, orange). HTL and ETL enhance the charge transport and enable the recombination of the charge carriers to take place in the EML of the diode. This effect can be further improved by using blocking layers (green) for holes (HBL) and electrons (EBL) as additional layers. For a better injection of the charge carriers, a hole injection (HIL, purple) and an electron injection layer (EIL, purple) can be used. In many cases, the hole-transport- and blocking layers are combined in one layer to avoid additional manufacturing steps. The same applies to the electron-transport- and blocking layers.[21] Figure 2.1 shows a potential structure of a multilayer OLED with an injection- (HIL, EIL), a transport- (HTL, ETL), a blocking- (HBL, EBL), and an emissive layer (EML).

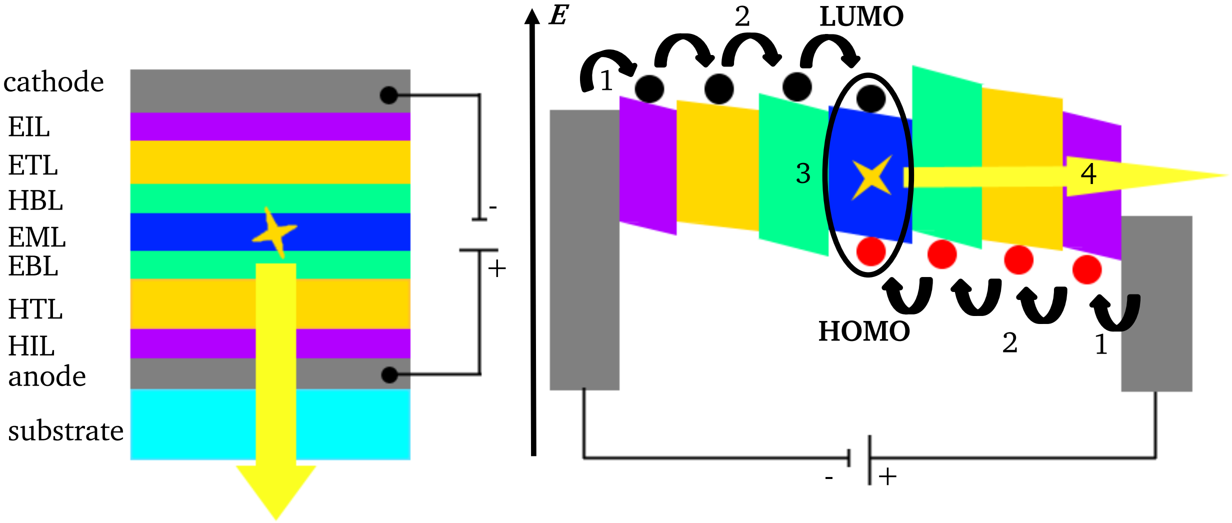

Figure 2.1: Principle scheme of a multilayer OLED with injection (purple), transport (orange), blocking (green), and emissive (dark blue) layer (**left**). Energy diagram with the hole (black) and electron (red) transport (**right**). Reproduced after literature.[22]

If some current is applied to both electrodes, four different processes are taking place in the OLED. At first, the charge carriers are injected (**1**), followed by charge carrier transport (**2**), recombination of carriers, and forming of an exciton (**3**) and, at last, light emission (**4**). These four processes are explained in more detail within the following parts.

Either the current is limited by the injection (injection limited current, ILC) or by the space charge (space charge limited current, SCLC).[23] If there is a limited amount of charge carriers between metal and the organic semiconductor, and the current is limited by charge carrier injection, it is called ILC. Here, the maximum measured current is smaller than the SCLC because no space charge can be generated.[24] In the case of SCLC, more charge carriers per time interval are available than the organic semiconductor can transport, and an ohmic contact exists. Therefore, the current is only dependent on the charge carrier mobility in the organic layer, not from the injection itself.[25] Typical values of charge carrier mobility for thin layers of organic solids are between 10^{-6} - 10^{-3} $\mathrm{cm^2V^{-1}s^{-1}}$[26] and create a space charge field, which influences the charge carrier transport.[27]

For the injection of an electron into the organic semiconductor, an energy barrier Φ_{Inj} has to be overcome. In the case of an ohmic contact, this barrier is zero. In real systems, this barrier is larger than zero, and Schottky-barriers reduce the energy barrier Φ_{Inj} to the energy barrier Φ_{B}.[28] Lower Φ_{Inj} can be overcome by thermal emission, field emission, or by the combination of these emissions (thermionic field emission).[21] In addition to that, the image-charge potential ($\Phi_{\mathrm{Image\text{-}charge}}$) is reduced by the outer electrical field Φ_{Field} and results in Φ_{combined} (Figure 2.2). This potential can be tunneled by the Fowler-Nordheim-field emission, which disregards the Shottky-effect, in high electrical fields.

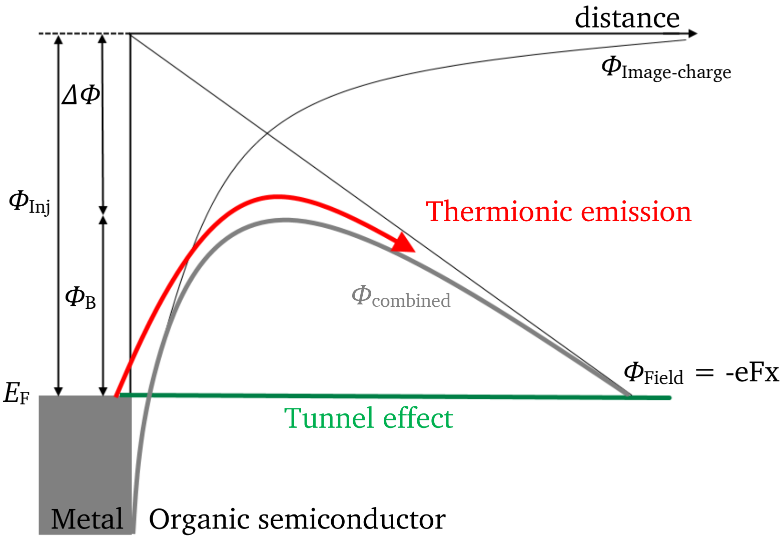

Figure 2.2: Schematic representation of thermionic emission (red) and tunnel effect (green). In the style of Schwoerer and literature.[21]

In an enhanced model of Gartstein and Conwell, the Schottky-effect, as well as the existing disorder in organic solids, are considered. Due to the Schottky-effect, the effective energy barrier, which has to be overcome is Φ_{B}. However, the existing disorder of organic solids includes the present hopping transport. The model from Gartstein and Conwell for a charge carrier transport from a metal into an organic semiconductor is shown in Figure 2.3.

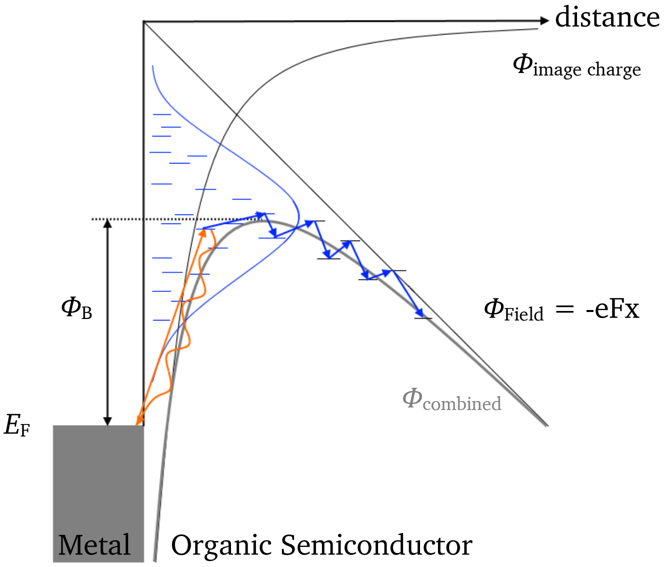

Figure 2.3: Model of charge carrier injection by GARTSTEIN and CONWELL. The charge carrier is injected from metal to organic semiconductor. Reproduced after literature.[29]

In this model, the charge carriers are hopping (orange arrow) from the Fermi level (E_F) of the electrode to a marginal energy level of the GAUSSIAN state distribution (blue), from where the charge carrier has two different options. On the one hand, the charge carrier is transferred to further energy levels with greater distance from the electrode, and finally, the energy barrier Φ_B can be overcome. On the other hand, the charge carrier can jump back to the electrode, where it can recombine with its image-charge (curved orange arrow).[29]

If an electron meets a hole in the organic semiconductor, they can recombine and form an exciton with a lifetime of some nanoseconds. Dependent on the overall spin (S), triplet (T_1), or singlet (S_1) excitons are built. Triplet excitons are having an overall spin of one with three different possibilities for an arrangement and singlet excitons an S of zero with one possibility for arrangement, which means that three times more triplet excitons are formed than singlet excitons. After excitation to higher levels, they can relax to favorable configurations by radiative decay or non-radiative decay.[4] In the following JABLONSKI-diagram (Figure 2.4), the different relaxation processes from the excited states are shown.

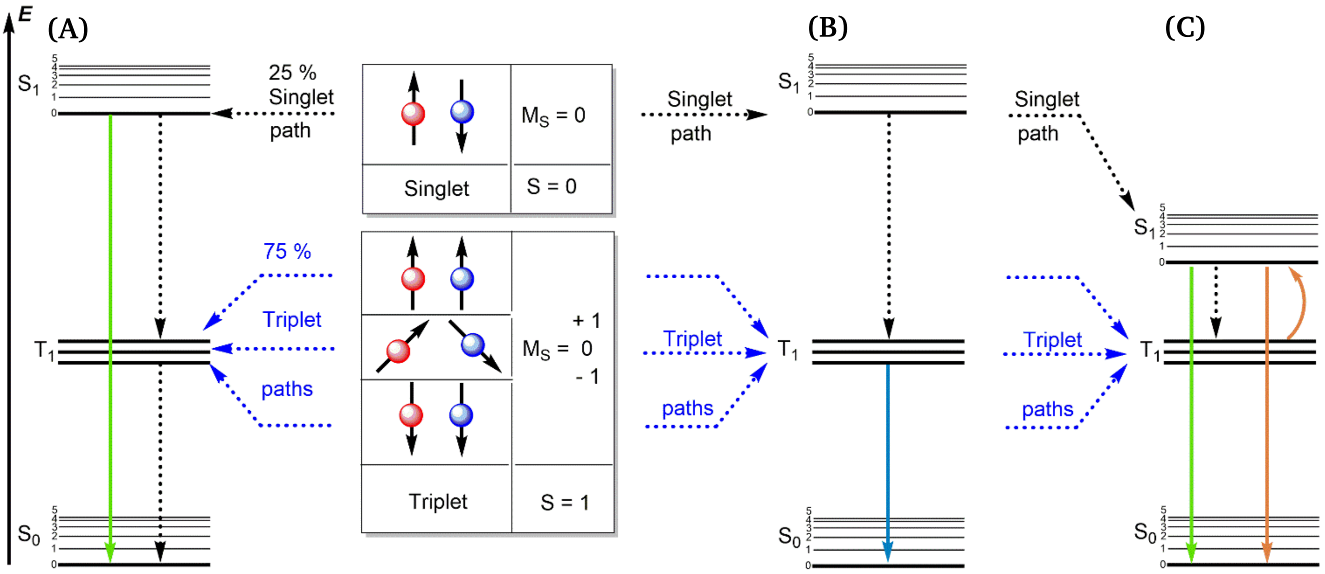

Figure 2.4: JABLONSKY diagram of different electroluminescence mechanisms from the singlet (S_1) and triplet (T_1) excitons. The vibrational states for T_1 are missing for clarity. (**A**) Fluorescence, (**B**) Phosphorescence, and (**C**) thermally activated delayed fluorescence (TADF). Reproduced after literature.[4]

Singlet (S_0, $S_1 \ldots S_n$) - and triplet (T_1, $T_2 \ldots T_n$) -states are divided up into different vibration states (v = 0, 1, 2, 3…). The crossover between two different vibration states within one spin state is called vibrational relaxation, and the crossing between two different spin states at the same multiplicity is known as internal conversion (dashed arrows in black). Both processes are non-radiative. Standard organic emissive materials (**A**) are producing light only by the decay of an excited singlet state (green arrow), the so-called Fluorescence. In comparison to this decay, a conversion of a singlet state into a triplet state or the other way around, known as an intersystem-crossing-process (ISC), is ten times slower due to its high energy gap between of 0.5 – 1.0 eV between singlet and triplet state (ΔE_{ST}). The lifetime of a triplet exciton can go up to 10 s due to the forbidden spin relaxation from T_1 to the S_0 ground state and leads to a non-radiative decay (dashed arrow in black).[30]

In the case of triplet emitter (**B**), metal-organic complexes with metals like Ir(III), Pt(II), Ru(II), Re(I), and Os(II) are used. Due to the heavy metal ion, these complexes show an effective spin-orbit interaction, which enables two different processes. On the one hand, the relaxation of the T_1 state into the S_0 ground state, which is radiative (phosphorescence). Phosphorescence is enabled as a result of the significantly reduced lifetime of the triplet state of 1 μs. On the other hand, the ISC rate is improved by four to five orders of magnitude due to a reduction of ΔE_{ST} by spin-orbit coupling. As a consequence, in such triplet emitters, all generated excitons can be used for light generation. Nevertheless, the concentration of triplet excitons in the emitter layer should not be too high, otherwise quenching by triplet-triplet annihilation (TTA) will occur.[30]

During TTA, two triplet excitons collide and delete each other in two different ways. On the one hand, a ground state S_0 and an excited state S_n are built. With an internal conversion (IC), the S_n state can relax into S_1 and with delayed fluorescence to S_0. On the other hand, one triplet exciton is built by the recombination of two different triplet excitons. Both processes of TTA result in quenching of phosphorescence and are shown in Figure 2.5.[30]

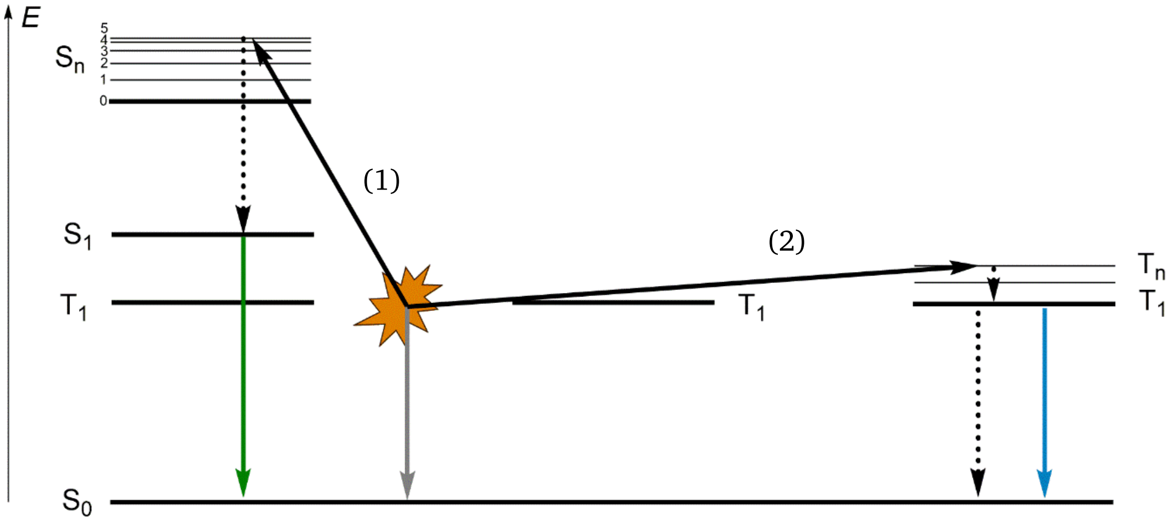

Figure 2.5: Triplet-triplet annihilation (TTA). Reproduced after literature.[31]

To avoid TTA, the triplet emitter is brought into a matrix (guest and host principle) where an energy transfer from the host (donor) to guest (acceptor) takes place. This energy transfer can follow two different mechanisms.

The first mechanism of energy transfer (FÖRSTER-transfer) is based on dipole-dipole interactions. Therefore, the distance between donor and acceptor should be lower than 10 nm due to its dependence on r^{-6}. Additionally, the spectral overlap and the orientation of donor and acceptor are prerequisites.[32] For the second mechanism (DEXTER-transfer), an intermolecular electron interchange takes place and is dependent on the overlap of neighboring molecular orbitals.[33] In both transfers, the excitons are generated at the host and transferred to the guest, whereby these excitons can be generated to a certain extent directly on the emitting guest, too. Following both transfer mechanisms, host singlets (S_H), as well as host triplets (T_H), can be transformed into guest triplets (T_G) by using ISC after converting the triplet excitons into singlet excitons (triplet harvesting).[34] Unfortunately, the energy gap between the guest and the host is vast because of the higher triplet energy of the host in comparison to the guest. This higher energy enables the energy transfer between host and guest and disables the back transfer of energy for catching the exciton but accelerates the degradation of the material.[35] For solving this problem, exciplex-triplet-energy-transfers (ExTET) were developed. Therefore, the phosphorescent guest is in a matrix with the electron transport material as a host and a hole transport material. As a result, an exciplex is built, whose energy levels (S_E and T_E) are significantly lower than the levels from the lonely host. This formation of an exciplex leads to higher efficiencies and higher lifetimes at lower operating voltages.[4,34] Figure 2.6 is comparing the ExTET with regular host-guest energy transfer.

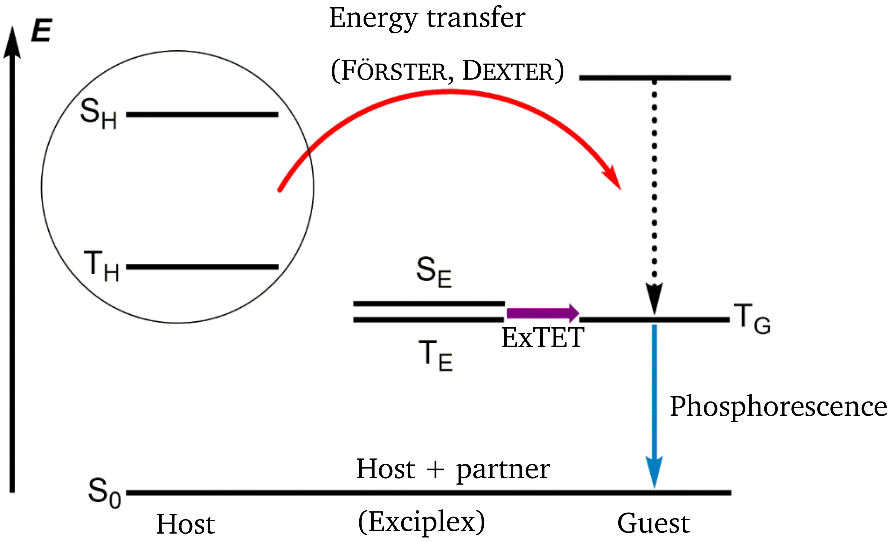

Figure 2.6: Exciplex-Triplet-energy transfer (ExTET) compared to regular host-guest-energy transfer. H: Host, E: Exciplex, G: Guest. Produced after literature.[34]

For the third possibility to generate light by organic materials, it is necessary to have a minimal energy gap between the triplet and singlet excited states (less than 0.1 eV). This small gap guarantees a useful reversed intersystem crossing (rISC) and a high emissive rate ($S_1 \rightarrow S_0$) of around $10^6\,\mathrm{s}^{-1}$ to avoid competing with non-radiative relaxation processes.[4] The interrelation between the rISC rate and ΔE_{ST} is given by the ARRHENIUS equation (Equation 1).

$$k_{\mathrm{rISC}} = A \cdot exp\left(-\frac{\Delta E_{\mathrm{ST}}}{k_{\mathrm{B}}T}\right) \tag{1}$$

k_{rISC}	Rate of rISC	A	ARRHENIUS parameter
ΔE_{ST}	Energy gap between singlet and triplet excited states	k_{B}	BOLTZMANN constant
T	Temperature		

For calculating ΔE_{ST} it is necessary to calculate the energy of the lowest singlet (E_{S1}) and triplet (E_{T1}) excited states, like shown in Equations 2 – 4.

$$E_{\mathrm{S1}} = E_{\mathrm{orb}} + K + E_{\mathrm{ex}} \tag{2}$$

$$E_{\mathrm{T1}} = E_{\mathrm{orb}} + K - E_{\mathrm{ex}} \tag{3}$$

$$\Delta E_{\mathrm{ST}} = E_{\mathrm{S1}} - E_{\mathrm{T1}} = 2E_{\mathrm{ex}} \tag{4}$$

E_{S1}	Energy of lowest singlet excited state	E_{T1}	Energy of lowest triplet excited state
E_{orb}	Orbital energy	ΔE_{ST}	Energy gap between lowest singlet and triplet excited state
K	Electron repulsion energy	E_{ex}	Exchange energy

As seen in Equation 4, the minimization of ΔE_{ST} is paired with the minimization of the exchange energy E_{ex}, which can be calculated by Equation 5. Besides, this equation describes the overlap between the highest occupied molecular orbital (HOMO) and the lowest unoccupied molecular orbital (LUMO).[36]

$$E_{\mathrm{ex}} = \iint \phi(r_1)\varphi(r_2)\left(\frac{e^2}{r_1 - r_2}\right)\phi(r_2)\varphi(r_1)\mathrm{d}r_1\mathrm{d}r_2 \tag{5}$$

E_{ex}	Exchange energy	Φ	Wavefunction of HOMO
φ	Wavefunction of LUMO	r	Radius
e	Electron charge		

The described organic emitter materials have different capabilities to utilize the excitons for inducing photons, which leads to very different efficiencies of the OLED devices. This efficiency can be described in two ways – the real point of view and the quantum mechanical one. From the physical point of view, the current-density-voltage (J-V)-characteristics are very important to describe the efficiency of an OLED and is also connected to a balanced charge-transport. To investigate the charge-transport through an OLED, two different kinds of devices can be used. For the investigation of the hole-transport properties, hole-only devices (HOD) are used and for the properties of electron-transport electron-only devices (EOD), respectively. In the case of HOD, the electrodes should be close to the valence band of the investigated material and for EOD close to the conduction band.[37] If J depends quadratically on V in a log(J)-log(V) plot of a HOD, it describes the SCLC following Equation 6.[38]

$$J = \frac{9}{8}\epsilon_0\epsilon_\mathrm{r}\mu_\mathrm{p}\frac{V^2}{L^3} \tag{6}$$

J	Current-density	$\epsilon_0\epsilon_\mathrm{r}$	Permittivity of the material
μ_p	Hole mobility	V	Voltage
L	Device thickness		

Regarding the applied voltages, two different regimes can be discriminated, in *J*-*V* plots of EOD. For an ohmic regime, with a voltage below a critical voltage (V_crit), the electron current depends linearly on the bias voltage, following Equation 7.[38]

$$J = n_0 q\mu_\mathrm{n}\frac{V}{L} \tag{7}$$

J	Current-density	n_0	Equilibrium electron density
μ_n	Electron mobility	V	Voltage
L	Thickness of layer	q	Point charge

If the voltage is above $V_\mathrm{crit,}$ sharp increased electron currents can be observed, which is characteristic for an insulator with traps. Depending on the slope of this increase, trap-levels are located at single energy levels with an extremely sharp transition or point to distribution, if these levels are located at different energies. If the trap-levels are located at single energy levels, the current switches directly to the SCLC at this current, following Equation 8.[38]

$$J = N_\mathrm{c} q\mu_\mathrm{n}\left(\frac{\epsilon_0\epsilon_\mathrm{r}}{qN_\mathrm{t}}\right)^r\frac{V^{r+1}}{L^{2r+1}}C(r) \tag{8}$$

with $C(\mathrm{r}) = r^r(2r+1)^{r+1}(r+1)^{-r-2}$ and $r = T_\mathrm{t}/T$.

J	Current-density	N_c	Effective density of states in the conduction band
μ_n	Electron mobility	$\epsilon_0\epsilon_\mathrm{r}$	Permittivity of the material
N_t	Total density of traps	V	Voltage
L	Thickness of layer	q	Point charge
T_t	Trap distribution parameter		

In Figure 2.7, a calculated *J*-*V* characteristic is compared to the bulk limited SCLC, the diffusion-limited injection, and the Fowler-Nordheim current for a PPV device.

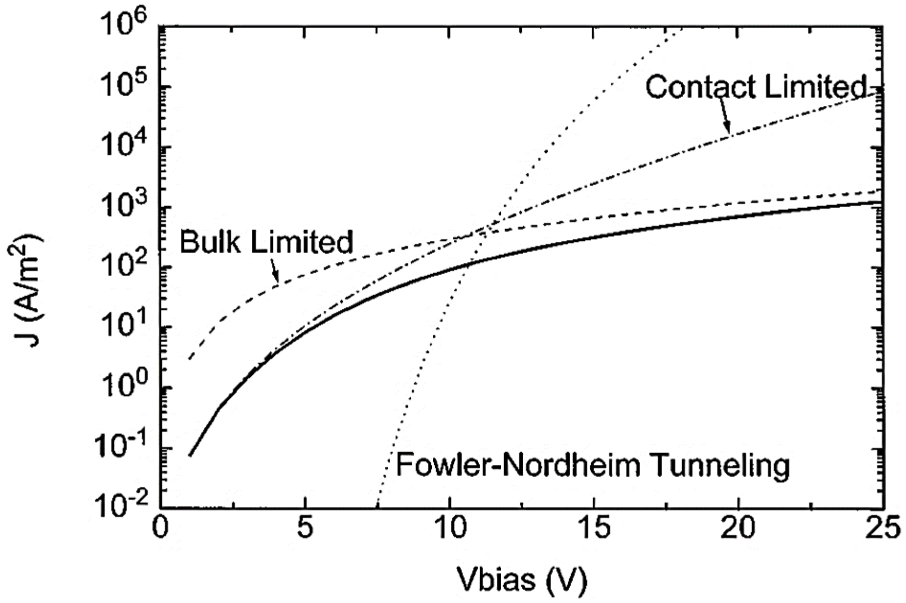

Figure 2.7: Calculated *J*-*V* characteristic (solid line) in comparison to contact limited, bulk limited, and the FOWLER-NORDHEIM current. Reproduced after literature.[38]

From the quantum mechanical point of view, the efficiency of an OLED can be described by the quantum efficiency (QE), referring to the numeral ratio of photons induced per injected exciton. If photons are generated within the emissive layer, it is called internal quantum efficiency (IQE), which is directly determined by the emitter. The numerical ratio of total photons emitting from the device per charge pairs injected is called external quantum efficiency (EQE).[36]

First-generation emitters are using fluorescent materials in OLED devices. For luminescence, they can only take advantage of singlet excitons, which leads to a maximum IQE of 25 %. Considering that outcoupling efficiency usually is around 20 %, the EQE is only 5 % at its maximum. Phosphorescent emitters, which are used in second-generation OLEDs, can reach 100 % IQE because they can harvest both kinds of excitons. Nevertheless, the heavy metals incorporated in second-generation OLEDs are mostly toxic. The combination of this toxicity, the costs of the heavy metals and the high-vacuum processes lead to very high production costs and require other alternatives for EML in an OLED.[5] Exciting alternatives to phosphorescent materials are thermally activated delayed fluorescence (TADF) – based materials. The principle of TADF was first rationalized in fluorescein solutions in 1929 by PERRIN and later in 1941 by LEWIS.[39] 2012 ADACHI and his coworkers proposed the TADF effect as a way to harvest non-emissive triplet excited states in OLEDs for the first time. They synthesized different TADF emitters based on carbazolyl dicyanobenzenes (CDCB) (Figure 2.8) as metal-free organic electroluminescent molecules. With 4CzIPN in an OLED, they could measure an EQE over 19 %, which is comparable to commonly used phosphorescence-based OLEDs.[1]

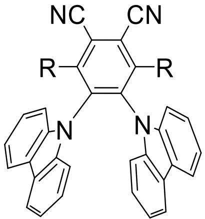

1

4CzPN: R = carbazolyl

2CzPN: R = H

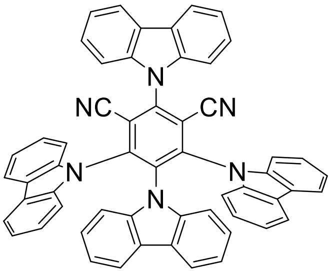

2

4CzIPN

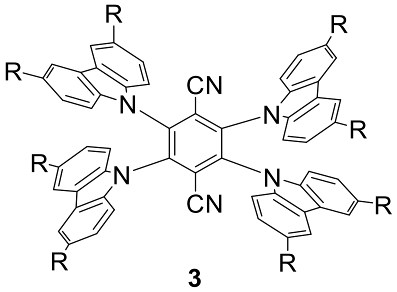

3

4CzTPN: R = H

4CzTPN-Me: R = Me

4CzTPN-Ph: R = Ph

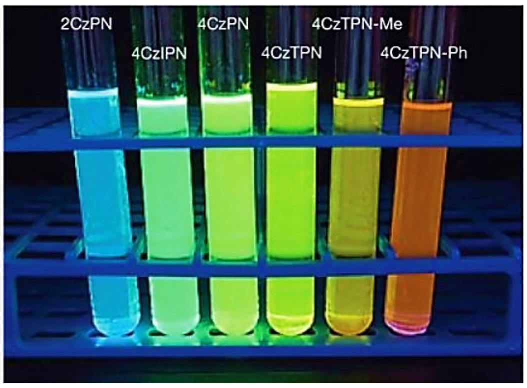

Figure 2.8: Molecular structures of the TADF emitters based on carbazolyl dicyanobenzenes as metal-free organic electroluminescent molecules (**top**). Photograph of the molecules in oxygen-free toluene under irradiation at 365 nm. Reproduced after literature[1] (**down**).

In order to satisfy the requirements for the smallest possible ΔE_{ST} and a high photoluminescence quantum yield (PLQY), attention to a few rules have to be paid when designing TADF emitters. The PLQY describes the efficiency of all (non-)radiative transition processes of a TADF emitter, and despite small ΔE_{ST}, PLQY is one key parameter for third-generation OLEDs. In addition to these two main parameters for efficient TADF emitters, a narrow full width at half-maximum (FWHM) of the emission spectrum (color purity) and stability of the materials (lifetime) are essential parameters for molecular design of TADF emitters. Luckily, all parameters are related to each other and could be optimized at the same time.[2] In Figure 2.9, material parameters are related to parameters of device performances and design methods.

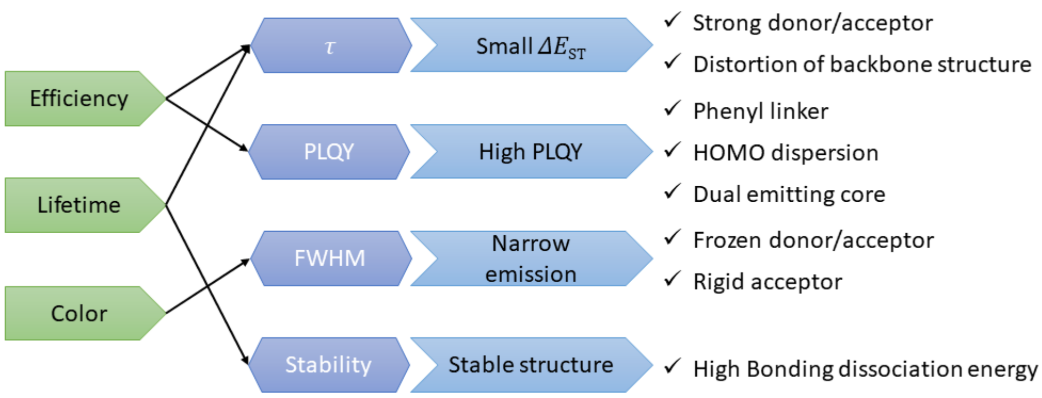

Figure 2.9: Material parameters related to the parameters of device performances and design methods. Reproduced after literature.[2]

TADF emitters with a donor-acceptor structure are the most promising and most reported designs in the literature. Strong donors and acceptors separate the HOMO and LUMO very precisely, resulting in lower ΔE_{ST}. These architectures for charge-transfer (CT) states with separated HOMO and LUMO could either be intra- or intermolecular. Even a charge-transfer through space (TSCT) is possible with well-separated donor and acceptor units, like SPULING et al. reported in 2018, working on [2.2]-paracyclophanes as deep blue TADF emitters (Figure 2.10).[40]

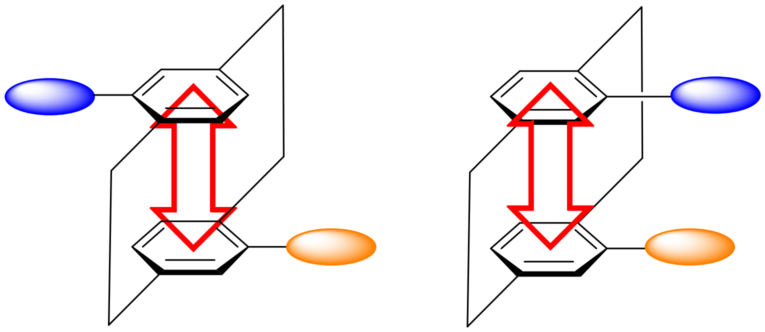

Figure 2.10: Skeleton of a [2.2]-paracyclophane for TADF emitter and the concept of through-space charge-transfer (TSCT, red arrow). Reproduced after literature.[40]

Due to their strong electron-donating ability, nitrogen-containing aromatics, including carbazole, diphenylamine, phenoxazine, and their derivatives, are favored as donor units.[4] Some commonly used donor and acceptor units are shown in Figure 2.11.

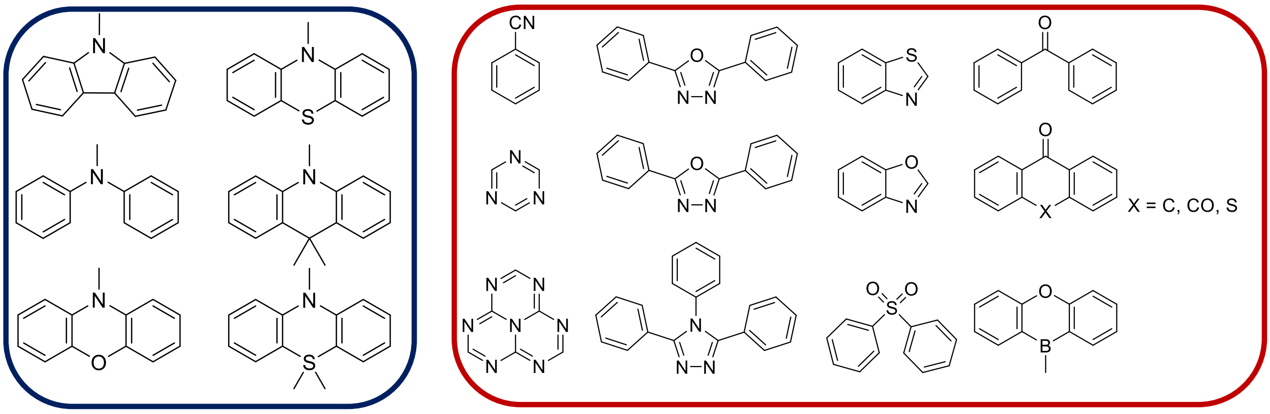

Figure 2.11: Commonly used donors (blue) and acceptors (red) for TADF molecules. Reproduced after literature.[4]

An easy way to increase the PLQY is to use a phenyl linker design. Unfortunately, the phenyl linker reduces the HOMO and LUMO isolation by extending them to himself, resulting in a larger ΔE_{ST} because of increased singlet energy. This effect can be avoided by strengthening the CT character with reliable donors and acceptors.[2] Some examples are shown in Figure 2.12.

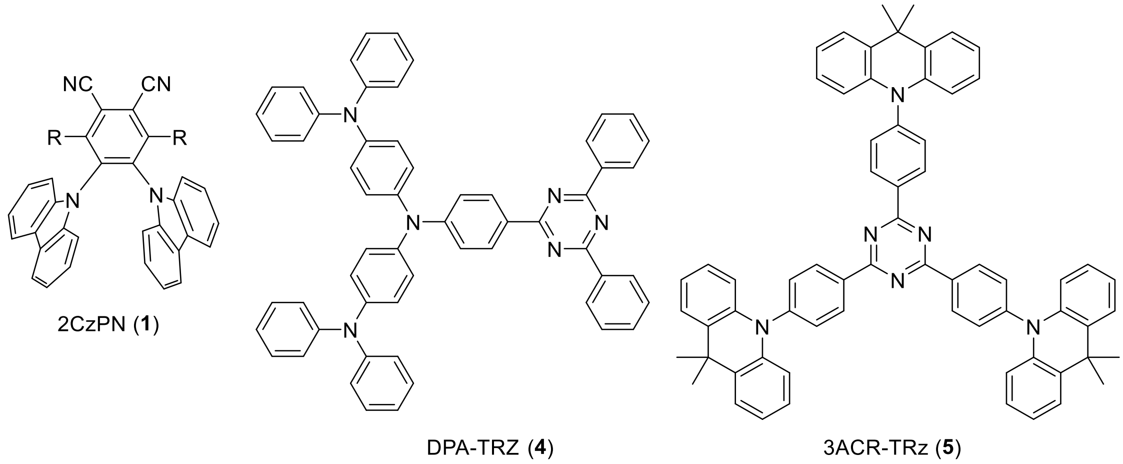
2CzPN (**1**)

DPA-TRZ (**4**)

3ACR-TRz (**5**)

Figure 2.12: Chemical structures of TADF emitters with high PLQY. 2CzPN (**1**) (100 %), DPA-TRZ (**4**) (100 %), and 3-ACR-TRz (**5**) (98 %).[2]

In point of color purity, FWHM is an essential parameter. In TADF emitters, it is possible to have multiple CT excited states with different energies resulting in broad emission spectra. However, for high color purity, TADF emitters with a narrow emission and a small FWHM are necessary, which can be realized in two different ways. On the one hand, the donor-acceptor based core structure can be frozen by fused structure or sterically hindrance. On the other hand, a rigid acceptor structure for minimizing the vibrational motion of the emitter.[2] Two examples of TADF emitters with a small FWHM are shown in Figure 2.13.

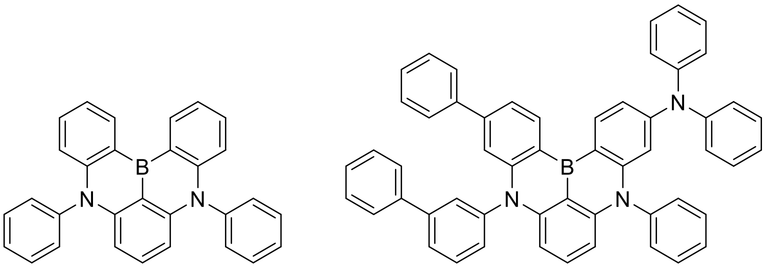

DABNA-1 (**6**)　　DABNA-2 (**7**)

Figure 2.13: Chemical structures of TADF emitters with narrow FWHM. DABNA-1 (**6**) (27 nm) and DABNA-2 (**7**) (24 nm).[2]

As explained in the section above, it is possible to improve every single material parameter by chemical structure. Unfortunately, it is very hard to design a material which satisfies all the requirements at the same time. That is why actual research processes focus on the development of such ideal molecules . An ideal structure for TADF emitters would have stable donor and acceptor moieties for stability, which are rigid for small FWHM. Furthermore, both components should be linked via an aromatic linker to reach high PLQY. Also, short times for delayed fluorescence (τ) are essential in the ideal molecular design of TADF emitters. Therefore, strong electron-donating and electron-withdrawing power by donor and acceptor are required. This is either possible by using strong donors and acceptors or through using multiple donors and acceptors.[2]

In 2017, Lu and his group published the two different TADF emitters 9-(2-(dimesitylboraneyl)-3-methylphenyl)-9*H*-carbazole (B-oCz, **8a**) and 3,6-di-*tert*-butyl-9-(2-(dimesityl-boraneyl)-3-methylphenyl)-9*H*-carbazole (B-oTC, **8b**) (Figure 2.14), which achieved a PLQY of 61 % and 94 % in neat films. Besides, these materials have an EQE of 8.0 % and 19.1 %, which is the highest value reported for non-doped solution-processed OLEDs.[3]

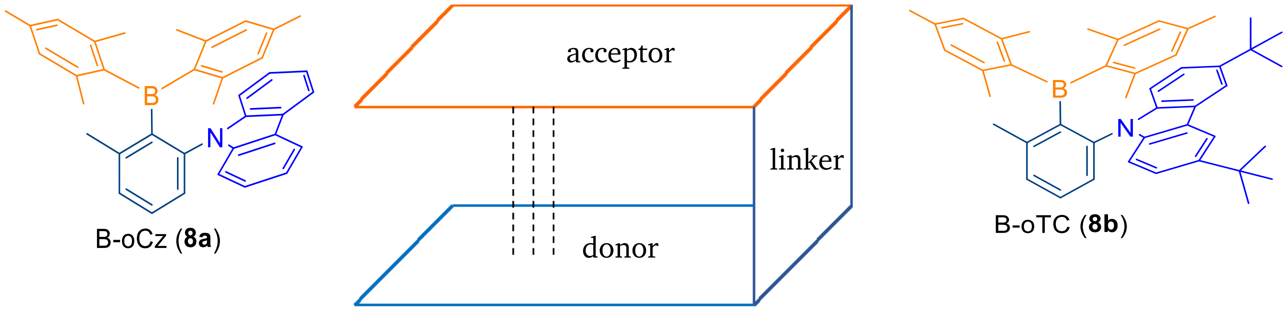

B-oCz (**8a**)　　B-oTC (**8b**)

Figure 2.14: Donor-Acceptor structure of the small molecules B-oCz **8a** and B-oTC **8b** with intramolecular charge-transfer through space (dashed black lines). Reproduced after literature.[3]

Both molecules **8a** and **8b** are designed like described above, following the donor-acceptor arrangement with a phenyl linker in between, leading to a CT through space and the linker simultaneously. Besides, the intramolecular vibration relaxation, which accelerates non-radiative decay, is suppressed by the strong intramolecular interactions. Also, LU and his group are using carbazole derivatives as strong donors and the boron compound as acceptor. This donor-acceptor arrangement results in small ΔE_{ST} of 0.068 eV and 0.046 eV, making these materials interesting candidates for efficient TADF emitters. Further on, these donor and acceptor components can suppress self-quenching processes.[41,42] As another interesting parameter, the FWHM of B-oCz (**8a**) and B-oTC (**8b**) are 60 nm and 56 nm, which is very promising for pure (sky-)blue OLEDs.[3] Being two of only a few organic molecules, B-oCz (**8a**) and B-oTC (**8b**) can be used as pure material for solution-processed TADF OLEDs.[3,43] However, most SMOLEDs are still produced by thermal evaporation processes, making the whole fabrication process very expensive and very energy inefficient. In contrast to SMOLEDs, PLEDs can be easily processed in solution by spin-coating or other printing processes. As a result, large-area and also flexible imaging systems or lightning media can be produced much more easily and cost-effectively on a large scale.[22]

In principle, it is possible to use similar design strategies for polymers like for small molecules. So, in macromolecules, HOMO and LUMO should be separated carefully on donor and acceptor for a small $\Delta E_{ST.}$ Besides, the non-radiative transition should be suppressed by using a certain rigid structure. Due to the conjugated polymeric system, it is challenging to achieve small ΔE_{ST} and high PLQY. Further on, the triplet excitons in polymers and oligomers are often quenched by the intra- or intermolecular TTA.[6] However, in literature, different design strategies for TADF polymers are reported and are shown in Figure 2.15.[5–9]

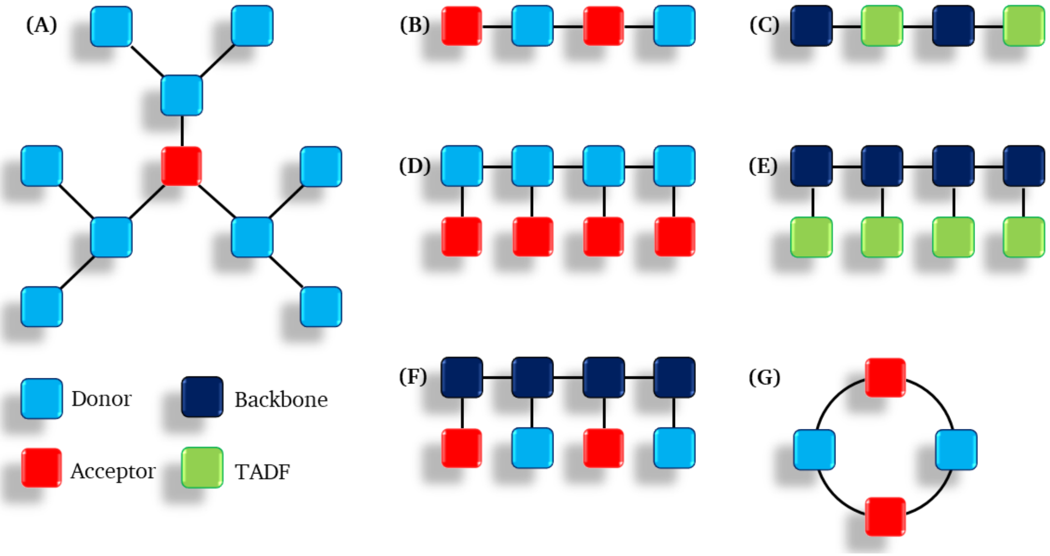

Figure 2.15: Reported design strategies for TADF macromolecules. (**A**) dendrimers, (**B**) alternating donor and acceptor moieties, (**C**) TADF unit between conjugated backbone, (**D**) conjugated donor with grafted acceptor units, (**E**) conjugated backbone with grafted TADF units[5,6], (**F**) conjugated backbone with grafted donor and acceptor units for charge-transfer through space[8,9] and (**G**) donor-acceptor-donor-acceptor π-conjugated macrocycle[7].

To combine the advantages of B-oCz (**8a**) and B-oTC (**8b**) with the advantages of polymer-based OLEDs, design strategies **D** and **E** seem to be very promising from a chemical point of view. The critical point to offer TADF character to conjugated organic macromolecules is to tune the singlet and triplet energy level. Therefore, the HOMO has to be distributed over the entire backbone, while the LUMO is localized on the acceptor groups in the side chain. Dias and co-workers reported a TADF polymer (COPO2, **9**), designed from a small molecule (PTZ-DBTO2, **10**), with a very similar fluorescence to the corresponding small molecule and a maximum EQE of 11.05 % at 5.5 V. In the same work, this group publish COPO1 (**11**), following strategy **E** for designing a TADF polymer. Therefore, Dias and co-workers are using PTZ-DBTO2 (**10**) again for the TADF unit and a non-conjugated ethylene group as backbone and styrene as a spacer. Unfortunately, the maximum EQE of COPO1 is only around 2.3 % at 7 V. As acceptor, Dias and co-workers are using a dibenzothiophene derivative and phenothiazine as the donor.[44] Both polymers, COPO2 (**9**) and COPO1 (**11**), and the corresponding small molecule PTZ-DBTO2 (**10**) are shown in Figure 2.16.

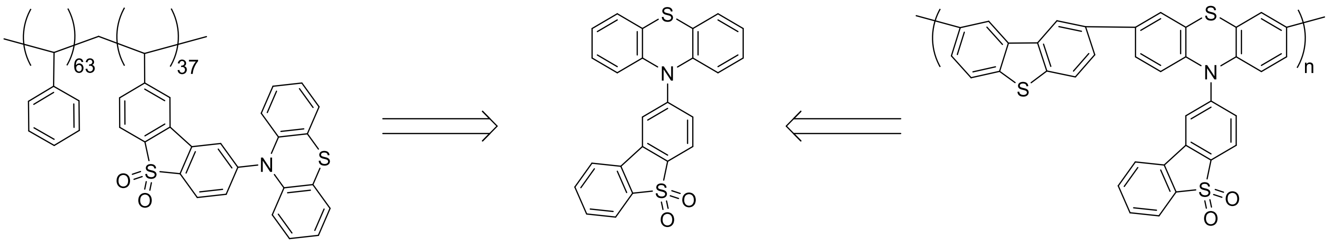

9 **10** **11**

Figure 2.16: Structures of TADF polymers COPO2 (**9**), COPO1 (**11**), and corresponding small molecule PTZ-DBTO2 (**10**).

3 Objectives

Even though most reported thermally activated delayed fluorescence (TADF) emitters are small molecules, there are several problems in the production of organic light-emitting diodes (OLEDs). These emitters can crystallize very easily and already surpassed an external quantum efficiency (EQE) of 35 %. Unfortunately, such good crystallization properties are resulting in poor solubilities and do not lead to enclosed films in solution processing. Thus, these emitters are mostly deposited by thermal evaporation under high vacuum with high temperatures, which results in size-limited OLED devices at relatively high costs. Due to these reasons, there is a high research interest in transferring TADF properties from small molecules to polymers, which can be easily prepared through solution-processing methods. These include spin-coating, ink-jet printing, and flow-casting. Therefore, they exhibit a high potential for large-area and large-scale fabrication.[5]

Like mentioned in the chapter before, the small molecules 9-(2-(dimesitylboraneyl)-3-methylphenyl)-9*H*-carbazole (B-oCz, **8a**) and 3,6-di-*tert*-butyl-9-(2-(dimesityl-boraneyl)-3-methylphenyl)-9*H*-carbazole (B-oTC, **8b**) are very promising candidates for blue-emitting TADF materials.[3] In combination with several design strategies for TADF polymers, different possibilities of developing new emitter materials based on TADF should be possible. Dias and co-workers already showed that it is possible to design different polymer architectures with a small molecule as a starting point.[44] Therefore, the following objectives were chosen for this project, summarized in Figure 3.1.

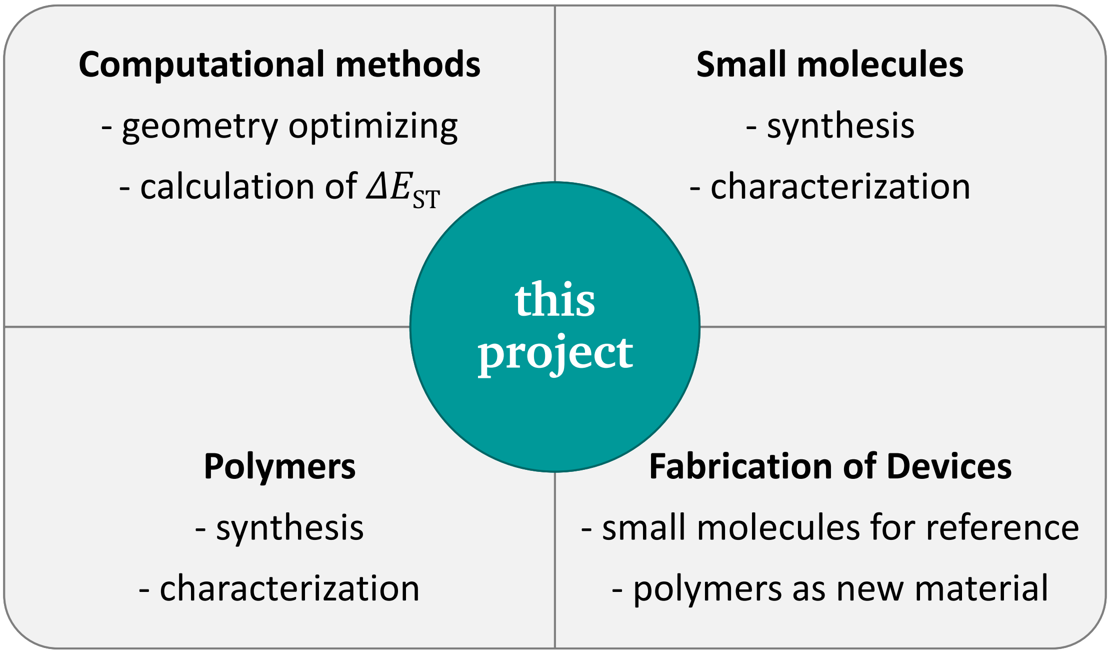

Figure 3.1: Overview of the different objectives of this project.

At the beginning of this master project, the small molecules and the target polymers were simulated by using density functional theory (DFT) and time-dependent DFT (TD-DFT) calculations. After optimization of the molecules' ground state, the energy gap between the excited singlet state and the excited triplet state (ΔE_{ST}) were calculated.

After using computational methods, the synthesis of both small molecules **8a** and **8b** were in focus. Both target small molecules are shown in Figure 3.2.

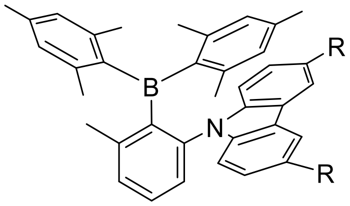

B-oCz (**8a**) R = H
B-oTC (**8b**) R = *tert*-butyl

Figure 3.2: Structure of the small molecules B-oCz (**8a**) and B-oTC (**8b**).

After a successful synthesis, the B-oCz (**8a)** and B-oTC (**8b**) were sublimated and analyzed with different analytical methods. For analytical methods, nuclear magnetic resonance spectroscopy (NMR), UV/Vis, photoluminescence and photoluminescence quantum yield (PLQY) measurements were used. Except for NMR spectra, all measurements were taken in solution and film.

In the next step, the properties of the small molecules had been tried to transfer to polymers. Therefore, additional functionalities were required. These functionalities depend on the chosen architectures for the target polymers. For these two small molecules, the following polymeric structures were quite close, using the donor in a conjugated backbone and the whole TADF unit in a sidechain (Figure 3.3).

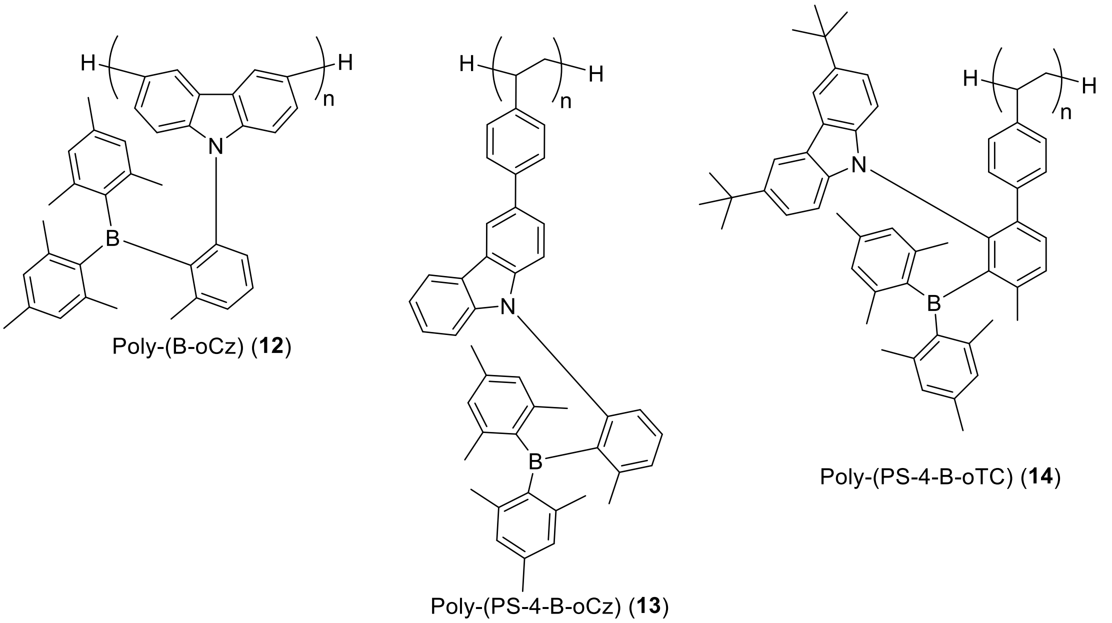

Poly-(B-oCz) (**12**)

Poly-(PS-4-B-oCz) (**13**)

Poly-(PS-4-B-oTC) (**14**)

Figure 3.3: Structure of the target polymers Poly-(B-oCz) **8c**, Poly-(PS-4-B-oCz) **13,** and Poly-(PS-4-B-oTC) **14**.

Like the small molecules, after a successful synthesis, the polymers were analyzed by using NMR techniques and standard photophysical measurements. Additionally, the synthesized polymers have been characterized by an analytical gel permeation chromatography (GPC) and by matrix-assisted laser desorption ionization with a time-of-flight mass spectrometry (MALDI-TOF), for determining their molecular weight distribution. Measuring the UV/Vis spectra, photoluminescence and PLQY were taken in solution and in films, too. Therefore, it was interesting to investigate if the different polymers will keep the properties of the small molecules of high PLQY, blue color, and no self-quenching.

The last part of this project was the fabrication of different devices for OLEDs. Even though the structure of the hole-only devices (HOD), electron-only devices (EOD), and light-emitting diodes (LED) are well optimized by Lu and co-workers[3] the devices for small molecules were fabricated by using standard materials and with a more comfortable device structure. This step had to be done for having a reference and an easier comparison of the small molecules with the new materials. Additionally, the small molecules were used in devices, which are fabricated by using spin-coating and thermal evaporation processes. At last, the devices were analyzed by measuring the photophysics like the current-density versus voltage curve and electroluminescence spectra. For LEDs, the external quantum efficiency (EQE) was calculated.

4 Results

The results are divided into following sections. The first section describes the retrosynthetic analysis of the target molecules, followed by the synthesis and the spectroscopic characterization of the small molecules 9-(2-(dimesitylboraneyl)-3-methylphenyl)-9*H*-carbazole (B-oCz, **8a**) and 3,6-di-*tert*-butyl-9-(2-(dimesityl-boraneyl)-3-methylphenyl)-9*H*-carbazole (B-oTC, **8b**). Included in the second section is the theoretical calculation by using (time-dependent) density functional theory of B-oCz (**8a**) and B-oTC (**8b**). The third section of the results is focusing on device fabrication using the blue emitters **8a** and **8b** as the emissive layer. Therefore, three different kinds of device structures were built to investigate the charge transport and efficiency. The last part of the results describes the completely new functionalization steps of B-oCz (**8a**) and B-oTC (**8b**) and the attempts to polymerize them.

4.1 Retrosynthetic analysis of the target molecules

In Scheme 4.1, the retrosynthetic analysis of the target polymers is shown. As starting material, the two different carbazole-derivatives 9*H*-carbazole (**20a**) and 3,6-di-*tert*-butyl-9*H*-carbazole (**20b**) are used.

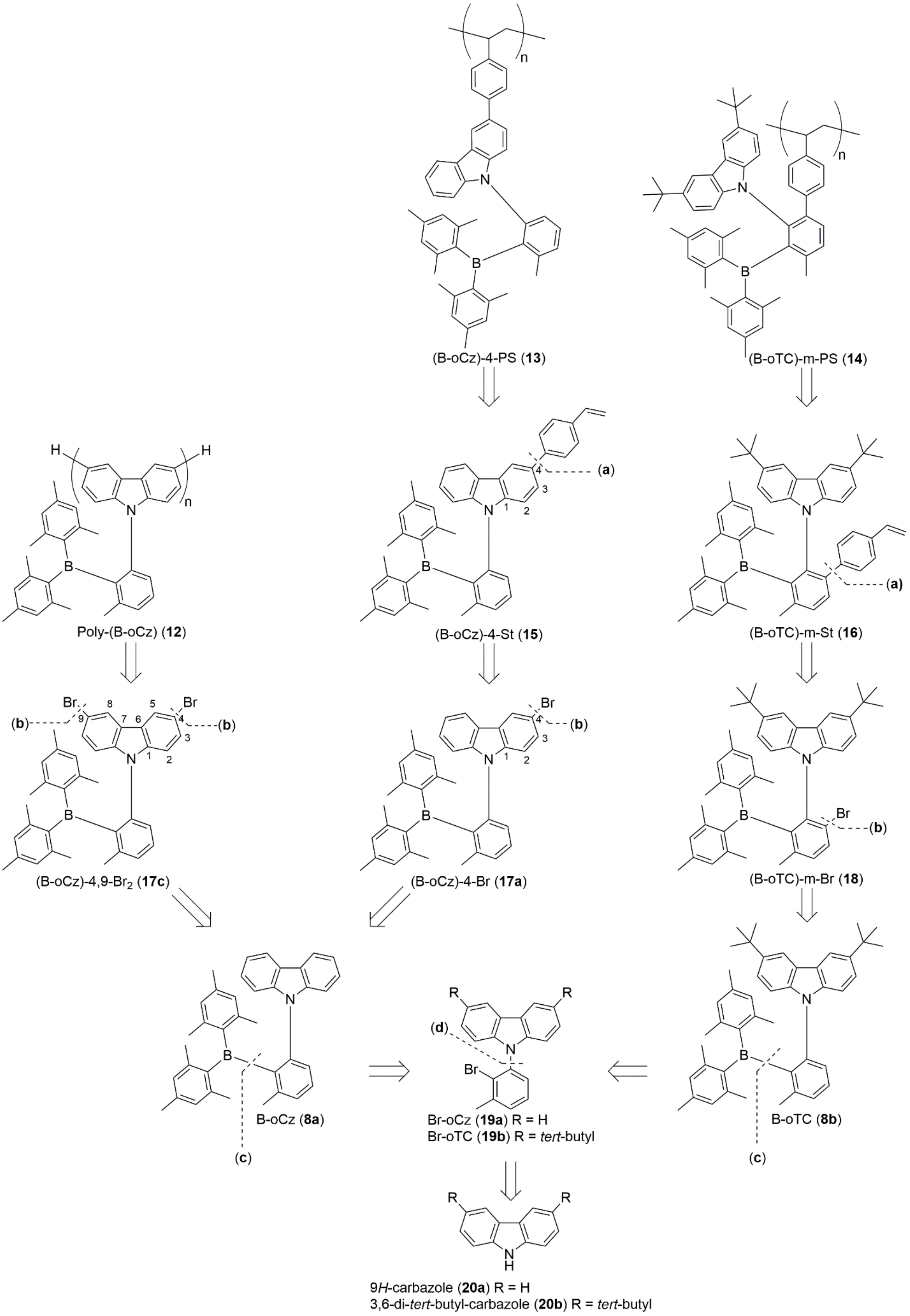

Scheme 4.1: Retrosynthetic analyses of target macromolecules Poly-(B-oCz9 (**12**), (B-oCz)-4-PS (**13**) and (B-oTC)-m-PS (**14**).

The synthetical objectives of this project are the polymers Poly-(B-oCz) (**12**), (B-oCz)-4-PS (**13**), and (B-oTC)-m-PS (**14**). The two polymers **13** and **14** can be synthesized by using different ways of polymerization of poly-(styrene). Therefore, the whole varieties of controlled and free radical polymerization can be used. Following the idea to polymerize a styrene derivative, the monomers of the two polymers **13** and **14** are the substituted styrene-derivatives **15** and **16**. In the case of monomer **15**, the styrene is coupled on the carbazole functionality, and for monomer **16,** it is connected to the phenyl linker of the molecule. Starting material for Poly-(B-oCz) (**12**) as well as for the styrene derivatives **15** and **16** are either the brominated species **17a, 17b**, **17c,** or **18**. To get the styrene functionality for (B-oCz)-4-St (**15**) and (B-oTC)-m-St (**16**), a cross-coupling reaction like the SUZUKI cross-coupling can be used (**a**). For synthesizing such a homo-polymer like Poly-(B-oCz) (**12**), the dibrominated (B-oCz)-4,9-Br_2 (**17c**) is converted in a YAMAMOTO cross-coupling reaction to the target polymer. The brominated molecules **17a**, **17b, 17c**, and **18** can be synthesized by using a bromination reagent like N-bromo-succinimide (NBS) (**b**) and the target small molecules B-oCz (**8a**) and B-oTC (**8b**). The two small molecules **8a** and **8b** can be synthesized by a lithium-halogen exchange and the addition of fluoro-dimesitylborane to the molecules Br-oCz (**19a**) and Br-oTC (**19b**) (**c**). As the starting material of the whole synthesis route, 9*H*-carbazole (**20a**) and 3,6-di-*tert*-butyl-9*H*-carbazole (**20b**) are used (**d**).

4.2 Results of the synthesis and spectroscopic characterization of B-oCz and B-oTC

First, the small molecules **8a** and **8b** were simulated by using computational methods to get a first impression of their photophysical properties. Afterward, the synthesis and characterization by using different spectroscopic methods is described. At the end of this section, the first attempts of device fabrication and optimization are discussed.

4.2.1 Theoretical calculations

To get a first impression about the physical properties of a molecule, theoretical calculations are beneficial. For thermally activated delayed fluorescence (TADF) emitters, the energy gap between the excited singlet (S_1) and the excited triplet (T_1) state (ΔE_{ST}) is a significant parameter. Figure 4.1 shows the results of the theoretical calculations.

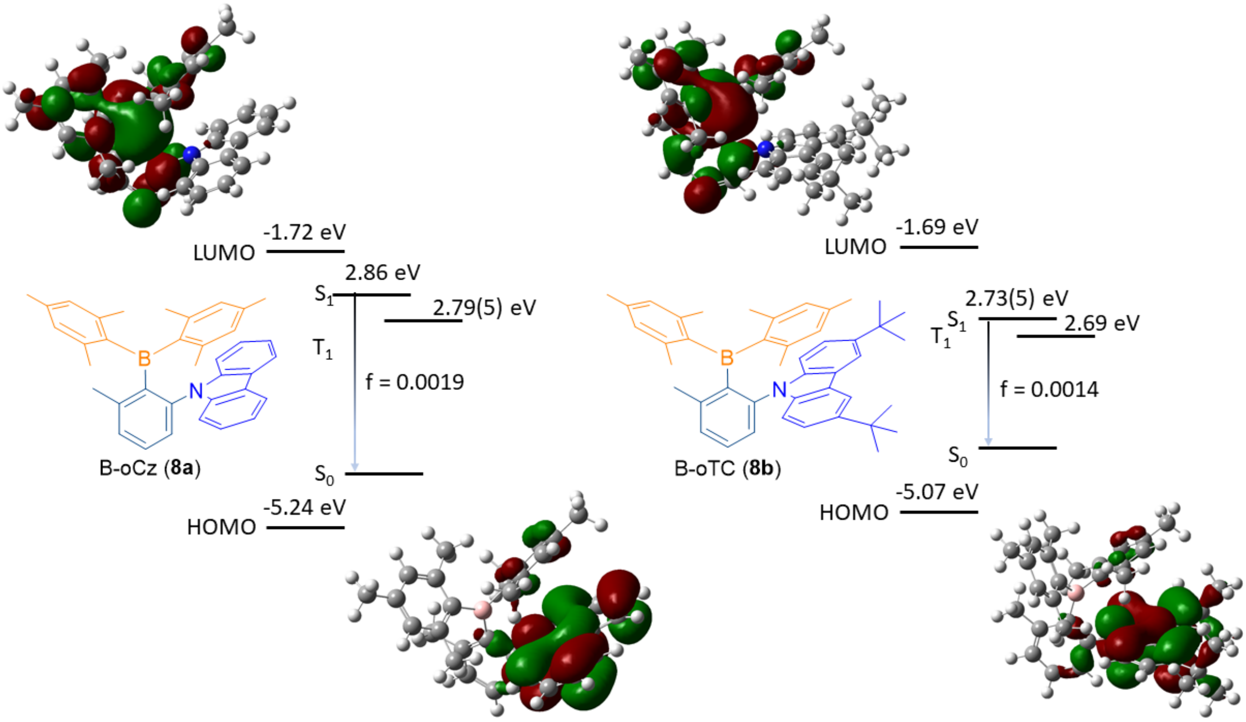

Figure 4.1: Chemical structures of B-oCz (**8a**, left), B-oTC (**8b**, right), and their frontier HOMO and LUMO. In addition to the structures, the energy level diagram for the HOMO and LUMO, as well as the low-lying singlet (S_1) and triplet excited (T_1) states are shown.

For geometry optimization of all ground states of the molecules, the density functional theory (DFT) at the B3LYP/6-31G(d) level of theory was used. The optimized ground states were used for the calculation of ΔE_{ST} with time-dependent density functional theory (TD-DFT) calculations at the same level of theory. The estimated ΔE_{ST} values and oscillator length f resulting from TD-DFT calculations were 0.065 eV (f = 0.0019) for B-oCz (**8a**), 0.045 eV (f = 0.0014) for B-oTC (**8b**) could be calculated, respectively. The ΔE_{ST} values for the two small molecules **8a** and **8b** are quite close to the reported values from Lu and his coworkers, with a standard deviation below 5 % for both molecules.[3] These values are below the magical value of 0.1 eV, which is one first hint for TADF properties. Additionally, Figure 4.1 shows the well-separated HOMO and LUMO location on the donor and the acceptor part of the molecules, respectively. This is in good agreement with the previously described design strategy for TADF emitters. Further on, the intermolecular π-π-interactions caused by the geometry and the quite small distances between donor and acceptor can lead to a charge transfer through space and thorough the phenyl linker.

4.2.2 Synthesis and spectroscopic characterization of B-oCz and B-oTC

The first synthetic task was to synthesize the two small molecules 9-(2-(dimesitylboraneyl)-3-methylphenyl)-9*H*-carbazole (B-oCz, **8a**) and 3,6-di-*tert*-butyl-9-(2-(dimesityl-boraneyl)-3-methylphenyl)-9*H*-carbazole (B-oTC, **8b**). Therefore, the following synthesis route was chosen in accordance to the literature[3] (Scheme 4.2).

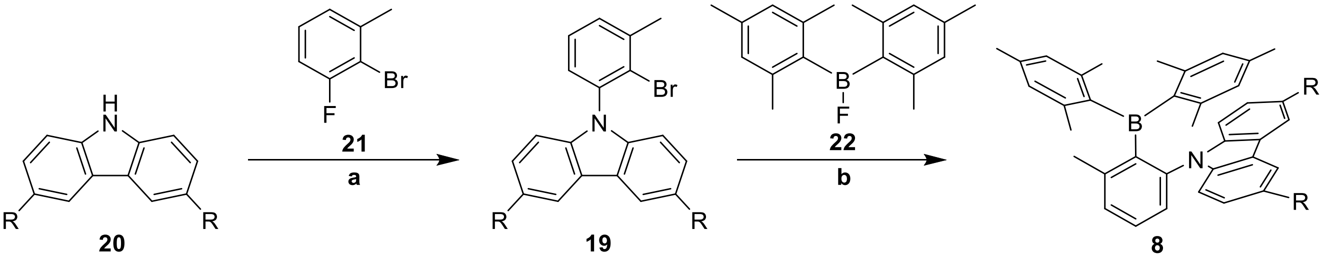

R = H (**20a**)
R = *tert*-butyl (**20b**)

R = H (**19a**)
R = *tert*-butyl (**19b**)

R = H (**8a**)
R = *tert*-butyl (**8b**)

Scheme 4.2: Synthesis of the small molecules B-oCz (**8a**) and B-oTC (**8b**). Reaction conditions: **a) 21**, Cs_2CO_3, anhydrous DMF, 150 °C, overnight, yield: 77.0 % (**19a**), 58.1 % (**19b**). **b)** 1.) *n*-BuLi, CPME, 0 °C, 30 min. 2.) **22**, CPME, 0 °C – RT, overnight, yield: 73.2 % (**8a**), 49.2 % (**8b**).

The first reaction step follows a nucleophilic aromatic substitution of the two carbazole derivatives **20a** and **20b,** after deprotonation by the base Cs_2CO_3. The intermediates 9-(2-bromo-3-methyl phenyl)-9*H*-carbazole (Br-oCz, **19a**) and 9-(2-bromo-3-methyl phenyl)-3,6-di-*tert*-butyl-9*H*-carbazole (Br-oTC, **19b**) were purified by column chromatography, using a solvent mixture of ethyl acetate (EA) and hexanes (Hex) (EA/Hex = 1:20, v:v). After the purification step, both molecules could be afforded as colorless solids in moderate yields of 77.0 % (Br-oCz, **19a**) and 58.1 % (Br-oTC, **19b**). To get the final molecules B-oCz (**8a**) and B-oTC (**8b**), *n*-butyl lithium was used as a base and fluoro-dimesitylborane (Mes_2BF, **5**) as a reagent for the acceptor moiety. For purification, the crudes were washed with hexanes and filtered to afford the (pale) yellow crystals with a good purity in yields of 73.2 % (B-oCz, **8a**) and 49.2 % (B-oTC, **8b**), respectively. These overall yields of 56.4 % and 28.6 % are much lower than in the literature, with 73.6 % and 60 %[3]. Reasons for this could be the problems during purification because the intermediates **19a** and **19b** smeared on the silica column and built a lot of mixed fractions that were not purified a second time. Also, the recrystallization from ethanol to afford the small molecules **8a** and **8b** did not work like it is reported in the literature. It could have happened, that parts of the product stacked in the organic phase during the washing with hexanes, that could not be separated from the impurities. However, for using these materials in the further synthesis steps, they were in an outstanding purification grade. For using them in organic light-emitting diodes (OLEDs), an additional sublimation was necessary. The corresponding NMR spectra of the intermediates **19a** and **19b**, as well as the molecules **8a** and **8b**, are shown in the appendix (Figure 9.1, page a – Figure 9.22, page k).

Besides the characterization of the small molecules, B-oCz (**8a**) and B-oTC (**8b**) with NMR spectroscopic methods, UV/Vis spectra, photoluminescence (PL) spectra and the photoluminescence quantum yield (PLQY) were measured. These measurements were taken in oxygen-free toluene and in films on quartz substrates under nitrogen. As depicted in Figure 4.2, both molecules **8a** and **8b** show two different absorption shoulders at wavelengths in the range around 300 nm and 350 nm (black curve). In addition to that, they show a broad shoulder at wavelengths of around 400 nm, which can be assigned to the intramolecular charge-transfer transitions caused by their donor-acceptor electronic structures.[3] The PL spectra (blue) are showing a structureless PL band with maxima at 480 nm (B-oCz, **8a**) and 500 nm (B-oTC, **8b**) in oxygen-free toluene. In films on quartz substrates, the PL bands are shifted to 469 nm and 478 nm, respectively.

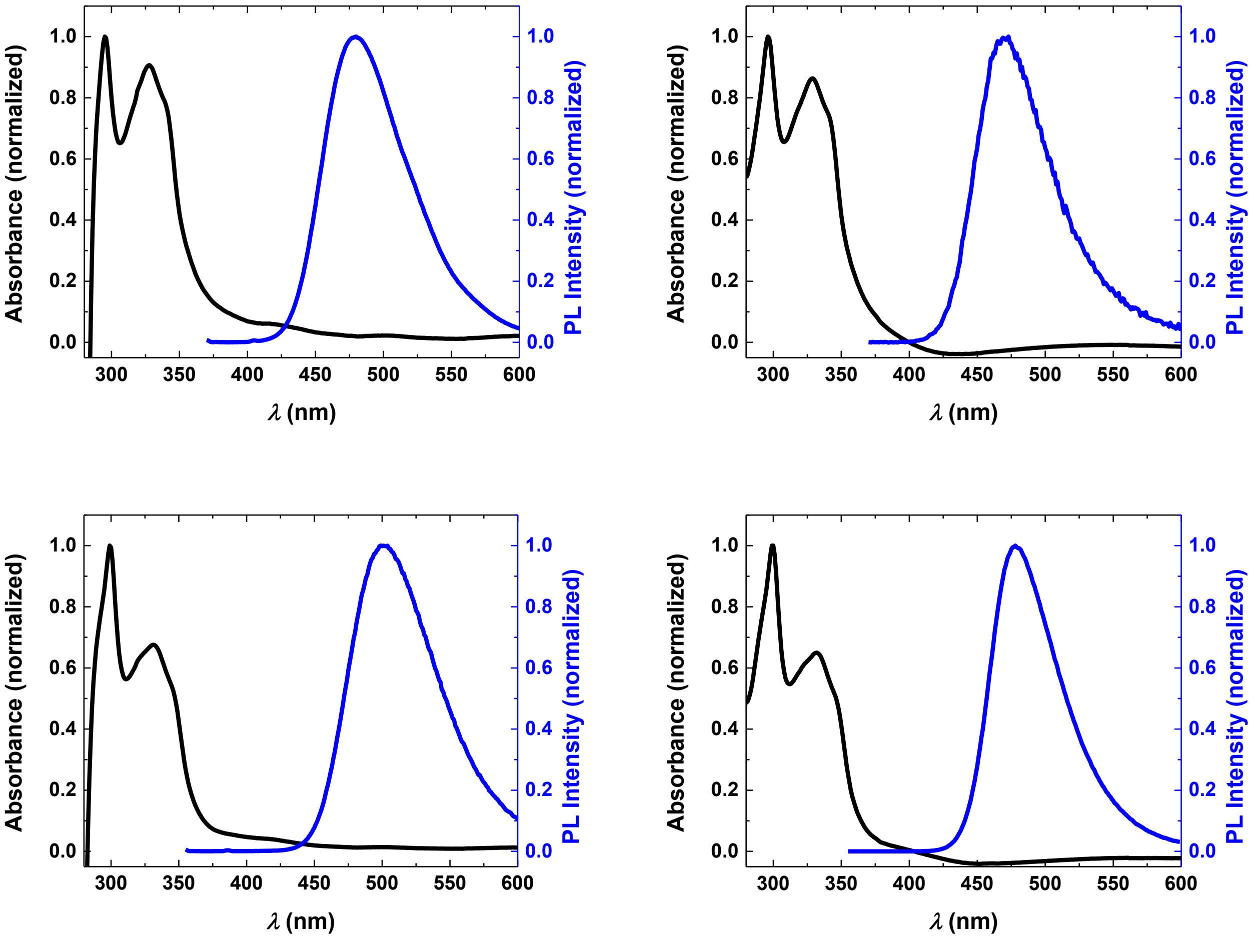

Figure 4.2: Spectroscopic results of B-oCz (**8a**, top) and B-oTC (**8b**, bottom). **Left:** measurements in oxygen-free toluene. **Right:** measurements in a film on a quartz substrate. **Black:** UV/Vis spectrum. **Blue:** PL spectrum.

The detected PLQY values for both small molecules are summarized in Table 4.1, together with the maxima of UV/Vis spectra and PL spectra. As well as the UV/Vis and PL measurements, PLQY was measured in oxygen-free toluene and in films on quartz substrates under nitrogen, too.

Table 4.1: Summarized results of the spectroscopic measurements for the small molecules B-oCz (**8a**) and B-oTC (**8b**) under oxygen-free conditions.

material	**UV/Vis**		**PL**		**PLQY (%)**	
	$\lambda_{\mathrm{solution}}$ **(nm)**	λ_{film} **(nm)**	$\lambda_{\mathrm{solution}}$ **(nm)**	λ_{film} **(nm)**	**solution**	**film**
B-oCz	295 | 328	296 | 329	480	469	52.6	11.9
B-oTC	299 | 331	299 | 332	500	478	87.4	76.0

The results from the UV/Vis- and the PL spectra are in agreement to the literature[3]. The maximum wavelengths of the PL spectra in solution are higher than in neat films because, in solution, the molecules do not have an ordered structure like in a film. Additionally, this redshift in a solvent is a hint for the TADF properties of B-oCz (**8a**) and B-oTC (**8b**). Furthermore, the PLQY of these small molecules in solution are in agreement to the reported values of 56 % for B-oCz (**8a**) and 91 % for B-oTC (**8b**) by concerning the uncertainty of the PLQY measurements of around 10 %. The higher PLQY values of 61 % and 94 % in neat films could not be reproduced. This could be related to the problems during the film preparation and the measurement procedure. The neat films were spin-coated on UV/ozone treated quartz substrates in a concentration of around 15 mg/mL, which results in a film thickness of around 50 nm for these materials. This concentration and this thickness may have been too low for these measurements. The second reason for such a decrease in the PLQY could be, that the substrates came in contact with the air during their placement in the integrating sphere before it was flushed with nitrogen. It was observed that at some points, the material started to crystallize on the surface. Unfortunately, these measurements could not be repeated because, in the subsequent attempts, the films did not stick on the substrates.

4.3 Device fabrication by using B-oCz and B-oTC as an emissive layer

Using B-oCz (**8a**) and B-oTC (**8b**) as an emissive layer in different device structures should help to understand the charge transport through these materials and could be used as a reference for future devices with polymers based on these materials. For the investigation of the single charge carrier injection and their transport through the different layers, hole-only devices (HOD) and electron-only devices (EOD) are commonly used. The combination of these two device structures leads to the light-emitting diode (LED), which is also used for investigating the color of the emissive layer in an electrical device and its efficiency. In this section, the single-carrier devices and organic light-emitting diodes based on the TADF emitters B-oCz (**8a**) and B-oTC (**8b**) are described.

4.3.1 Solution-processed devices

For investigating the carrier-transporting properties of B-oCz (**8a**) and B-oTC (**8b**), HOD and EOD were fabricated with the device structures shown in Figure 4.3.

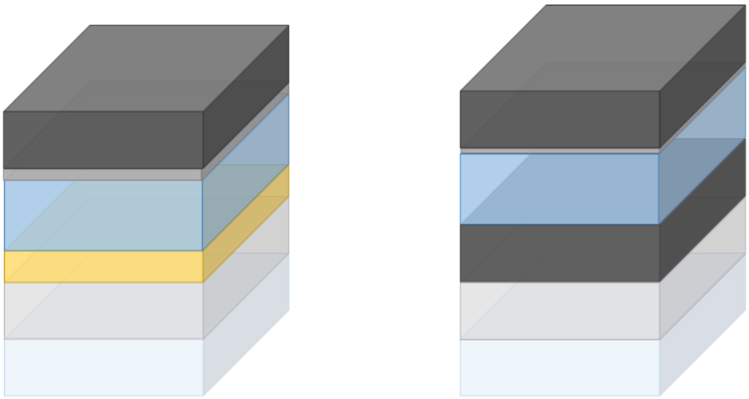

Figure 4.3: Schematic structure of solution-processed single-carrier devices. **Left**: hole-only devices with the device structure glass/ITO/PEDOT:PSS (55 nm)/emitter (200 nm)/ MoO_3 (10 nm)/Al (100 nm). **Right**: electron-only device with the device structure glass/Al_{ox} (100 nm)/emitter (200 nm)/Ba (5 nm)/Al (100 nm).

Using poly-(3,4-ethylene dioxythiophene)-poly-(styrene sulfonate) (PEDOT:PSS, **23**) as an additional layer in a HOD gave the possibility to investigate the hole injection properties of this material into the small molecules. Its chemical structure is shown in Figure 4.4.

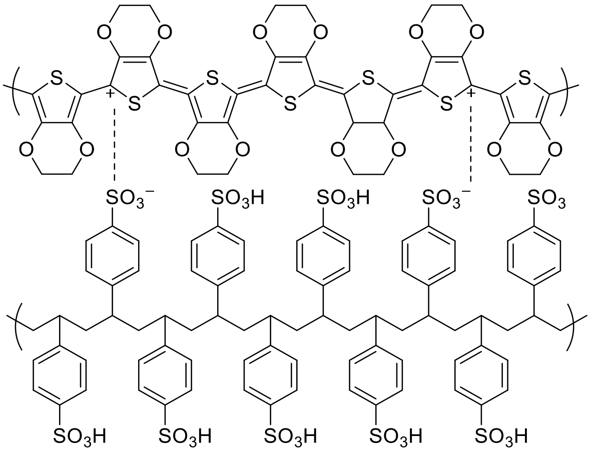

(**23**)

Figure 4.4: Chemical structures of poly-(3,4-ethylenedioxythiophene)-poly-(styrenesulfonate) (PEDOT:PSS, **23**).

For spin-coated single-carrier devices, a batch of the small molecules B-oCz (**8a**) and B-oTC (**8b**) were synthesized during a research internship before this project started. This batch was used and sublimated a second time before its usage in the devices. The results of the different current densities (*J*) versus the voltage (*V*) curves for the HOD and EOD of B-oCz (**8a**) and B-oTC (**8b**) are shown in Figure 4.5. If it was possible, the temperature-dependent scans were measured.

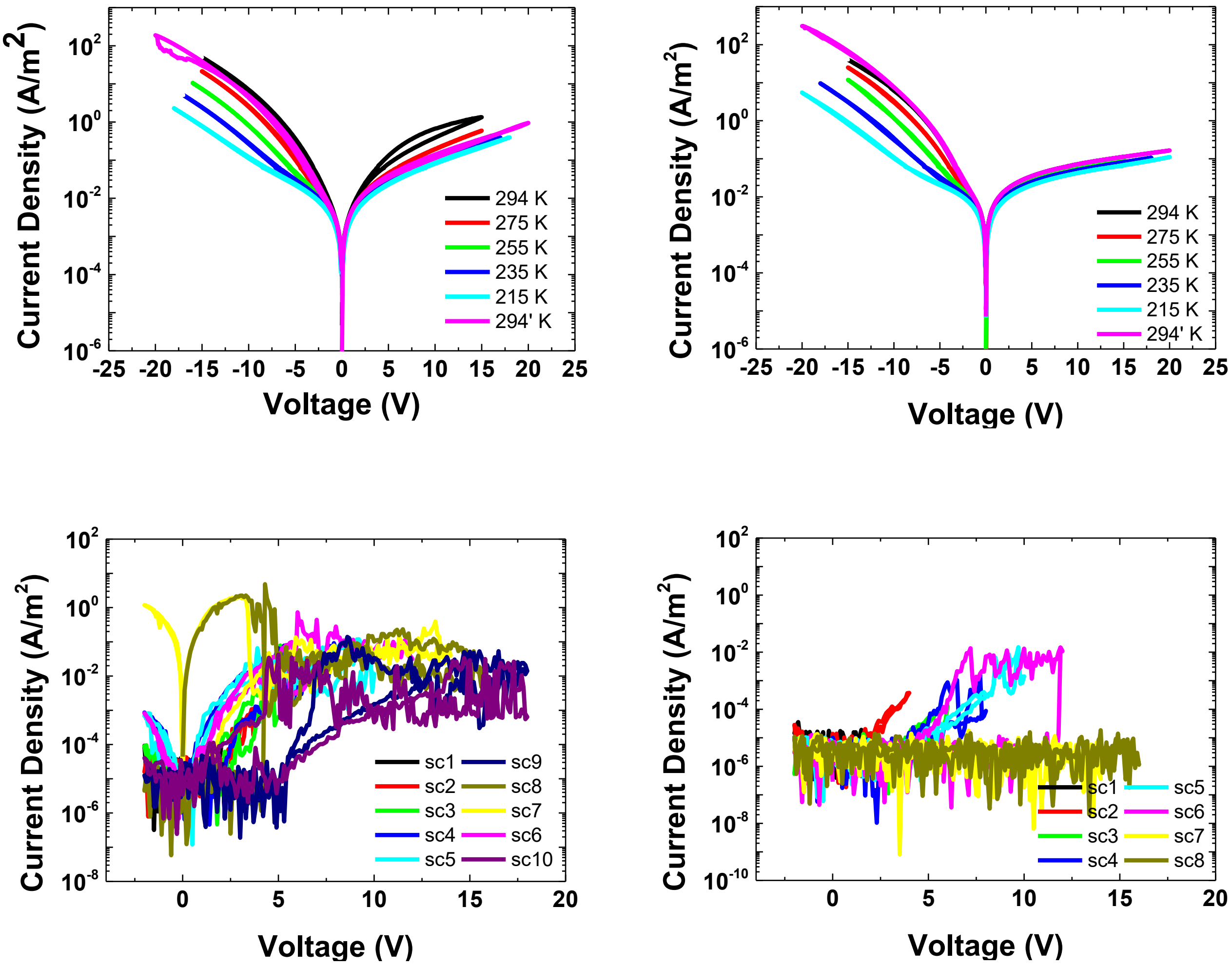

Figure 4.5: *J-V* curves resulting from measuring HOD (**top**) and EOD (**bottom**) of B-oCz (**8a, left**) and B-oTC (**8b, right**).

In the case of the spin-coated HODs for B-oCz (**8a**) and B-oTC (**8b**), the *J-V* curves at different temperatures show a temperature dependence on the left side (back-scan) and on the right side (forward-scan), these values are almost constant. Considering that in Equation 8, the temperature dependence of the current density is shown, this was expected for both sides of the scan for the HOD. The forward-scan describes the property of PEDOT:PSS as hole-injection and hole-transport layer, while the back-scan describes the properties at the interlayer between MoO_3 and the emissive layers. Due to the temperature dependence on the left side, it could be seen that MoO_3 builds an ohmic contact with the small molecules B-oCz (**8a**) and B-oTC (**8b**). In comparison to that, the PEDOT:PSS shows only leakage-current, which means that the current is not interacting with the small molecules **8a** and **8b** and only sent from one electrode to the other one. For the decreasing curve in the case of B-oCz (**8a**) on the left side, it is reasonable that the material degrades due to the high voltages and other defects in the microstructure of the films.

For the EODs of the spin-coated molecules B-oCz (**8a**) and B-oTC (**8b**), very noisy signals could be afforded after each scan. Unfortunately, no area of the devices was stable enough to measure the current density at different temperatures to verify if these results were leakage current or not. Again, the decreasing current density is related to a degradation process of the emitters **8a** and **8b**.

Despite the bad performance of the single-carrier devices, solution-processed organic light-emitting diodes based on B-oCz (**8a**) and B-oTC (**8b**) were fabricated. The schematic device structure is shown in Figure 4.6.

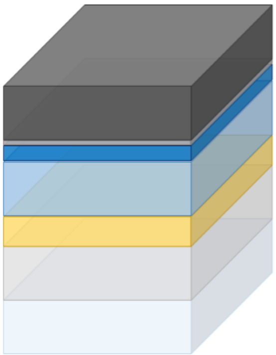

Figure 4.6: Schematic structure of solution-processed organic light-emitting diode following the device structure: glass/ITO/PEDOT:PSS (55 nm)/emitter (100 nm)/ TPBi (30 nm)/Ba (5 nm)/Al (100 nm).

As it was done for the single carrier devices, B-oCz (**8a**) and B-oTC (**8b**) were used from a batch of the research internship and sublimated a second time, before spin-coating. As electron-transport layer 2,2',2"-(1,3,5-Benzinetryl)-tris(1-phenyl-1-*H*-benzinimidazole) (TPBi (**24**), Figure 4.7) was used because of its HOMO and LUMO levels of -6.3 eV and -2.7 eV.[45] The results for the solution-processed LEDs of B-oCz (**8a**) are shown in Figure 4.8.

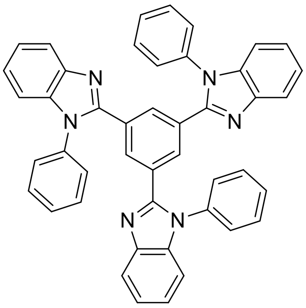

TPBi (**24**)

Figure 4.7: Chemical structure of 2,2',2''-(1,3,5-Benzinetryl)-tris(1-phenyl-1-*H*-benzinimidazole) (TPBi).

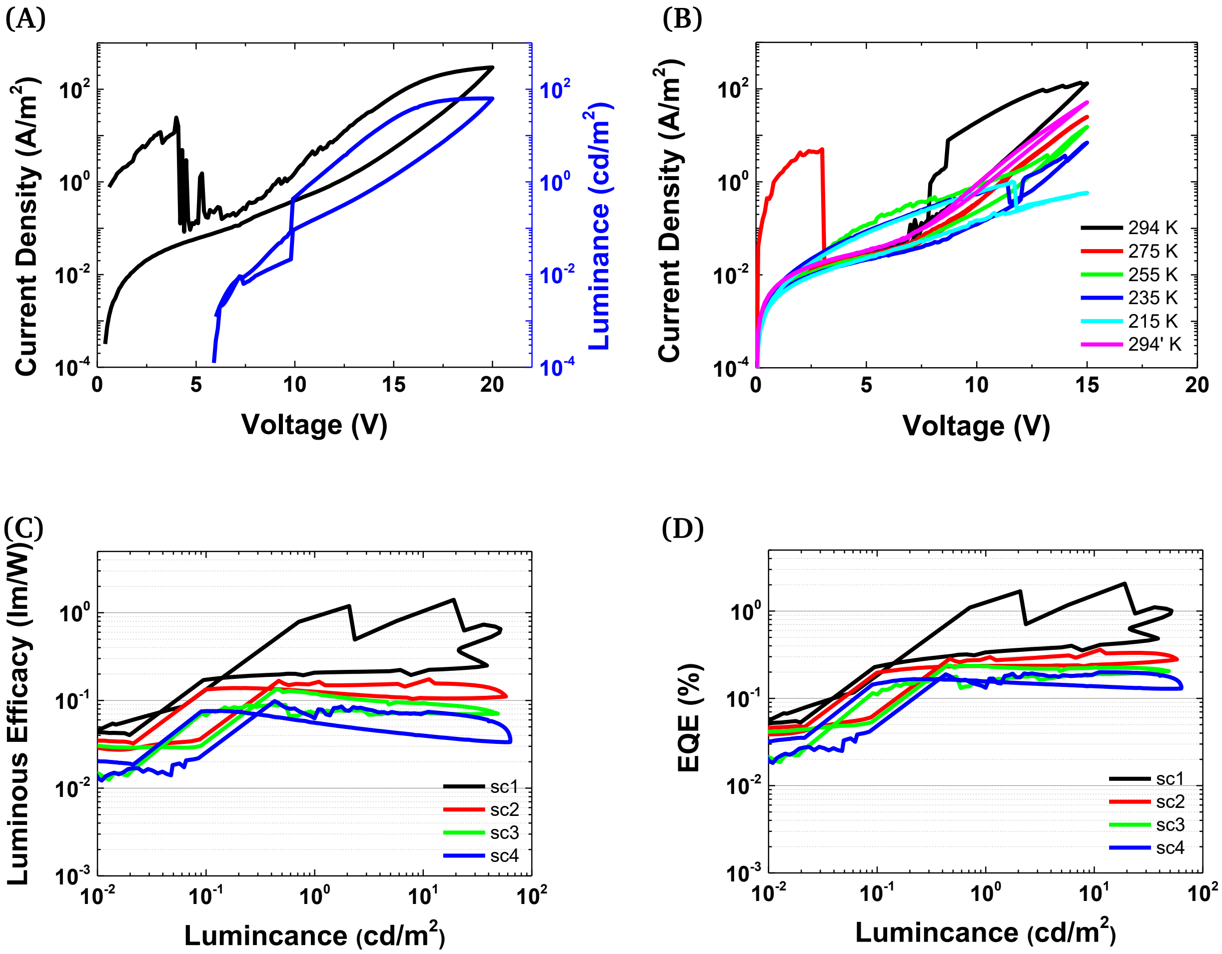

Figure 4.8: Results of a solution-processed organic light-emitting diode based on B-oCz (**8a**). **(A)** current density (black) and luminance (blue) at 20 V in one plot. (**B**) temperature dependence of current density at 15 V. Luminous efficacy **(C)** and external quantum efficiency **(D)** versus luminance.

Figure 4.8 (**A**) shows, that for a solution-processed organic-light emitting diode (OLED) based on B-oCz (**8a**), a very high voltage of 20 V was necessary to get a current density of around 10^3 A/m^2. At this voltage, a luminance of around 100 cd/m^2 was afforded with a low luminous efficacy of around 1 lm/W at 60 cd/m^2 (**C**). The lower the temperature, the lower the *J-V* curves (**B**) are which means that the current is dependent on the temperature. Unfortunately, this organic light-emitting diode shows only a maximum external quantum efficiency (EQE) (**D**) of around 1-2 % at a low luminance of 20 cd/m^2. This value becomes lower at higher luminance and with the number of scans caused by the degradation of the emitting material. The same trend in device characteristics can be seen for a solution-processed OLED based on B-oTC (**8b**) as an emissive layer (Figure 9.42, page w).

To get an impression of the color of an OLED, the electroluminescence spectrum (EL spectrum) is measured. This spectrum is also necessary to calculate the EQE of the devices. Both EL spectra of the solution-processed OLEDs based on the small molecules **8a** and **8b** are shown in Figure 4.9.

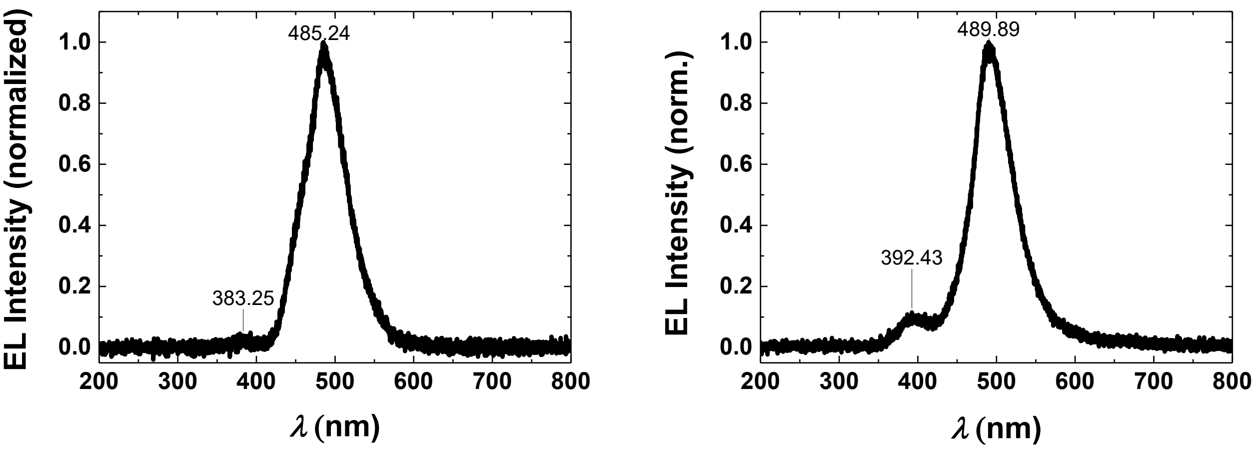

Figure 4.9: Normalized electroluminescence spectra of a spin-coated OLED based on B-oCz (**8a, left**) and B-oTC (**8b, right**).

Both small molecules **8a** and **8b** show a shapeless broad EL emission at maximum wavelengths of around 485 nm and 490 nm, which did not relate to the literature values of 463 nm[3] for B-oCz (**8a**) and 474 nm[3] for B-oTC (**8b**), respectively. This shift to higher wavelengths could be related to different possibilities causing the second small shoulder in the EL spectra at wavelengths of around 383 nm and 392 nm. On the one hand, this phenomenon could relate to impurities in the material, causing some charge carrier traps, which are shifting the maximum wavelengths. On the other hand, related to the emission spectrum of TPBi with its onset at 340 nm and a maximum at 385 nm[46], the second emission in the EL spectrum refers to the fluorescence of the electron-transport material TPBi (**24**). Nevertheless, both materials showed a (greenish-) blue emission. Nevertheless, this second shoulder led to decreasing efficiencies of the OLEDs and should be removed in the future.

Another parameter influencing the performances of a solution-processed OLED is the roughness of the surface. Therefore, the surface of solution-processed films on glass substrates with B-oCz (**8a**) and B-oTC (**8b**) was analyzed with atomic force microscopy (AFM). To get a representative impression of the surface's roughness, an area of 100 μm x 100 μm was measured for both materials **8a** and **8b**. The AFM pictures of these measurements are shown in Figure 9.40 on page u and a profile of height in Figure **9.41** on page v for all the films. These measurements result in a root mean square value of around 5.6 nm for B-oCz (**8a**) and 5.5 nm for B-oTC (**8b**), which was determined. In comparison to the literature, these values are roughly ten times higher, but the literature values were scanned on an area of 3 μm x 3 μm.[3] Additionally, it is reasonable that some defects and degradation processes inside the material led to lower efficiencies of the devices.

4.3.2 Thermally-evaporated devices

To improve the device performance, both small molecules **8a** and **8b** were thermally-evaporated as emissive layers. Additionally, TPBi (**24**) was added to the EOD as an electron-transport layer. The new device structures of HOD and EOD are shown in Figure 4.10.

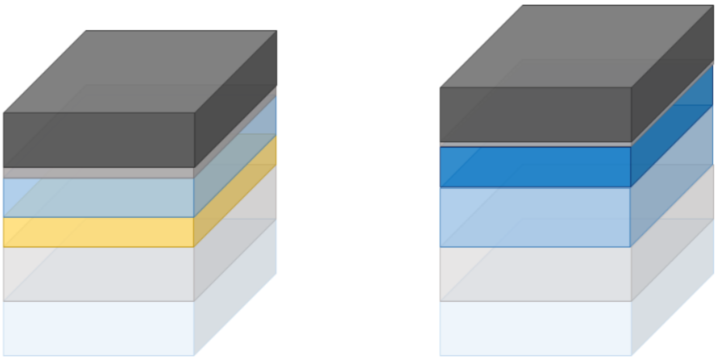

Figure 4.10: Schematic structure of thermally-evaporated single carrier devices. **Left**: hole-only devices with the device structure glass/ITO/PEDOT:PSS (55 nm)/emitter (60 nm)/ MoO_3 (10 nm)/Al (100 nm). **Right**: electron-only device with the device structure glass/Al_{ox} (100 nm)/emitter (110 nm)/TPBi (60 nm)/Ba (5 nm)/Al (100 nm).

In the case of all thermally-evaporated devices discussed in this subsection, B-oCz (**8a**) and B-oTC (**8b**) were used from the batch, synthesized at the beginning of this research project. Before this batch was used in devices, both small molecules **8a** and **8b** were sublimated once. The results of the single-carrier devices (HOD and EOD) of the thermally-evaporated B-oCz (**8a**) and B-oTC (**8b**) are shown in Figure 4.11.

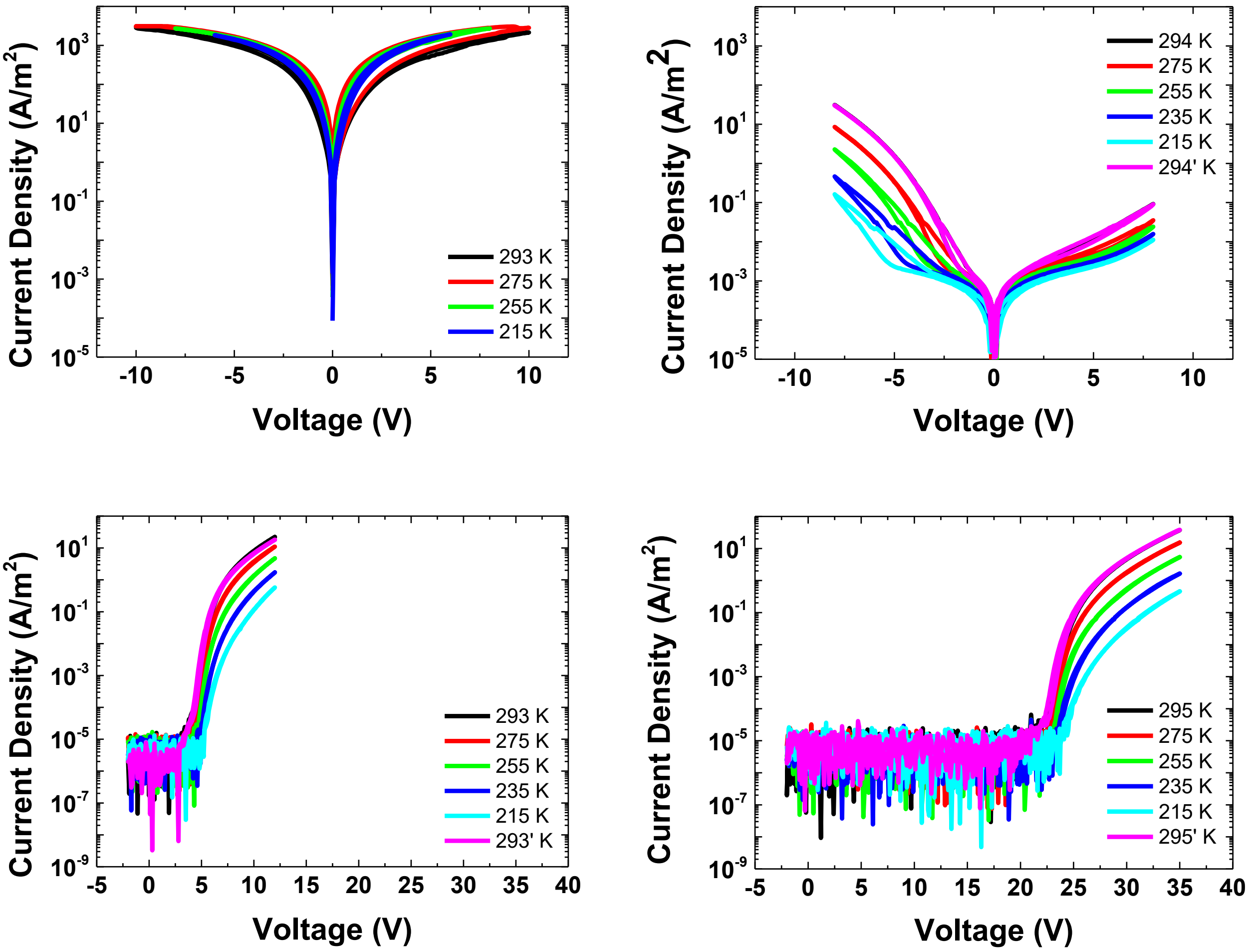

Figure 4.11: *J*-*V* curves resulting from measuring HOD (**top**) and EOD (**bottom**) of B-oCz (**8a, left**) and B-oTC (**8b, right**).

In almost every *J*-*V* curve of the thermally-evaporated small molecules **8a** and **8b**, an improvement in comparison to the spin-coated ones could be observed. However, the HOD of B-oCz (**8a**) showed only leakage current. Using the thermally-evaporated B-oTC (**8b**) instead of the solution-processed led to a temperature dependence of the *J*-*V* curves at even lower voltages for almost the same current density. Further on, both EODs showed a temperature dependence, and even very high voltages are necessary for B-oTC (**8b**).

Based on these results, new LEDs were fabricated by using thermally-evaporated B-oCz (**8a**) and B-oTC (**8b**). The schematic device structure is shown in Figure 4.12.

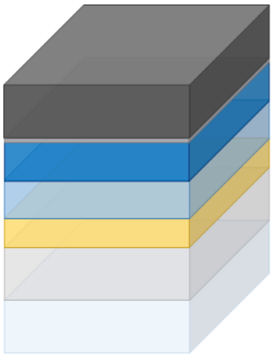

Figure 4.12: Schematic structure of thermally-evaporated organic light-emitting diode following the device structure: glass/ITO/PEDOT:PSS (55 nm)/emitter (60 nm)/ TPBi (60 nm)/Ba (5 nm)/Al (100 nm).

The device performance of B-oCz (**8a**) as a thermally-evaporated emissive layer is shown in Figure 4.13. Again, the *J*-*V* curve in comparison to the luminance is shown in **(A)** and the temperature-dependence of *J*-*V* curves in **(B),** together with the luminous efficacy **(C)** and EQE **(D)** versus the luminance.

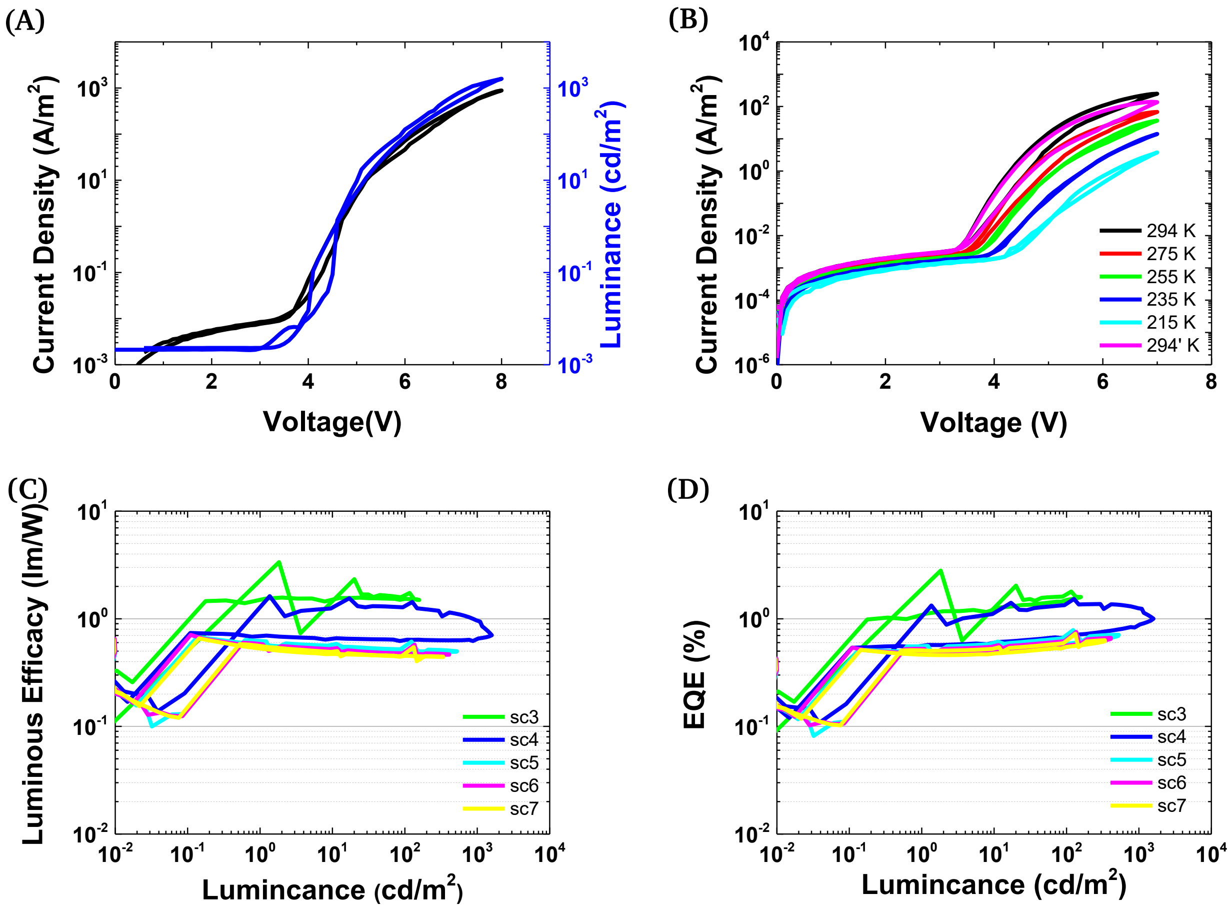

Figure 4.13: Photophysical results of a thermally-evaporated organic light-emitting diode based on B-oCz (**8a**). **(A)** current density (black) and luminance (blue) at 8 V in one plot. **(B)** temperature dependence of current density at 7 V. Luminous efficacy **(C)** and external quantum efficiency **(D)** versus luminance.

Figure 4.13 shows that almost every parameter improved for around one order of magnitude only by using the thermal-evaporation processes instead of the solution-processes for OLEDs. Also, the hysteresis of the material got less related to a lower degradation process of B-oCz (**8a**). The improvement of the LED efficiencies became obvious by comparison the luminous efficacy (**C**) and the EQE (**D**). While the solution-processed LEDs only achieved a maximum EQE of around 1 % at 20 cd/m^2, a maximum EQE of around 1.5 % at 100 cd/m^2 could be achieved for the thermally-evaporated ones. In the case of B-oTC (**8b**), almost the same trends could be observed only with higher absolute values.

In comparison to the solution-processed LEDs, the thermally-evaporated ones needed less than half of voltages to reach a current density of around 10^3 A/m^2 with even higher values for the luminance (**A**). The luminous efficacy (**C**) also improved by one order of magnitude and is constant in comparison to the solution-processed LEDs. For the LEDs of B-oCz (**8b**), the same results could be obtained but with even higher absolute values (see Figure 9.43 on page x and Table 4.2 on page 40). Despite the improvements of the thermally-evaporated LEDs, the afforded efficiencies were far away from the literature[3]. The color of the LEDs was verified by measuring the EL spectra, which can be seen in Figure 4.14.

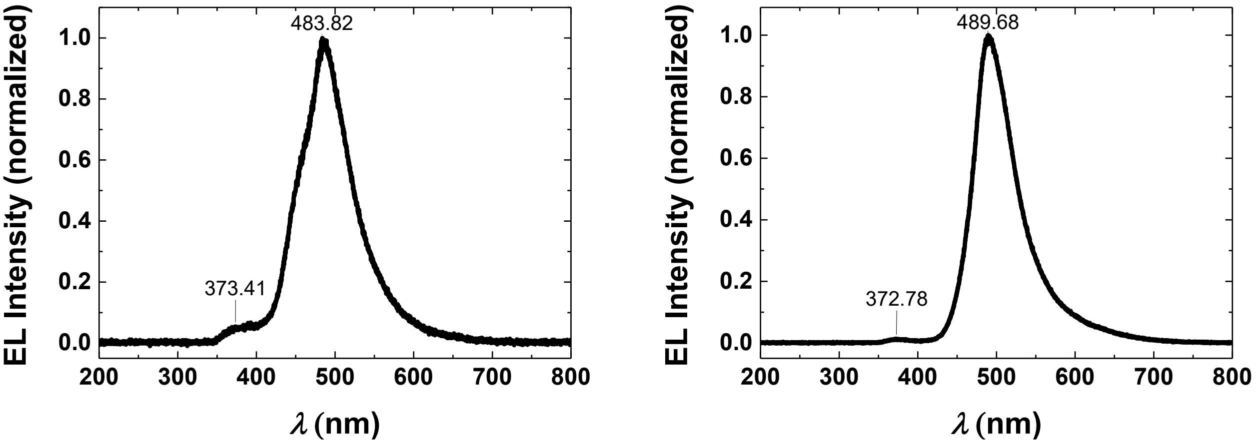

Figure 4.14: Normalized electroluminescence spectra of a thermally-evaporated OLED based on B-oCz (**8a, left**) and B-oTC (**8b, right**).

The maximum wavelengths of both EL spectra are related to the EL spectra shown in Figure 4.9 for the solution-processed small molecules **8a** and **8b**. The second smaller emission, mentioned above, also appeared at wavelengths of around 373 nm. In the case of B-oCz (**8a**), the primary shoulder is broader, which led to the assumption that the triplet state of TPBi is responsible for this redshift. The triplet state of TPBi has an energy level of around 2.7 eV[45], which is lower than the calculated triplet energy of B-oCz (**8a**) and nearly the same value of B-oTC (**8b**). Perhaps, the charge carriers recombined on the surface between the electron transport layer. Because of that, they are trapped in the triplet state of TPBi (**24**), leading to a loss of efficiencies in OLEDs and the broader EL shoulders.

To proof the hypothesis of trapped excitons in the triplet state of TPBi (**24**), another device structure was suggested. Figure 4.15 shows a comparison of the HOMO and LUMO levels in the fabricated devices by vacuum thermal evaporation compared to the device structure from the literature[3].

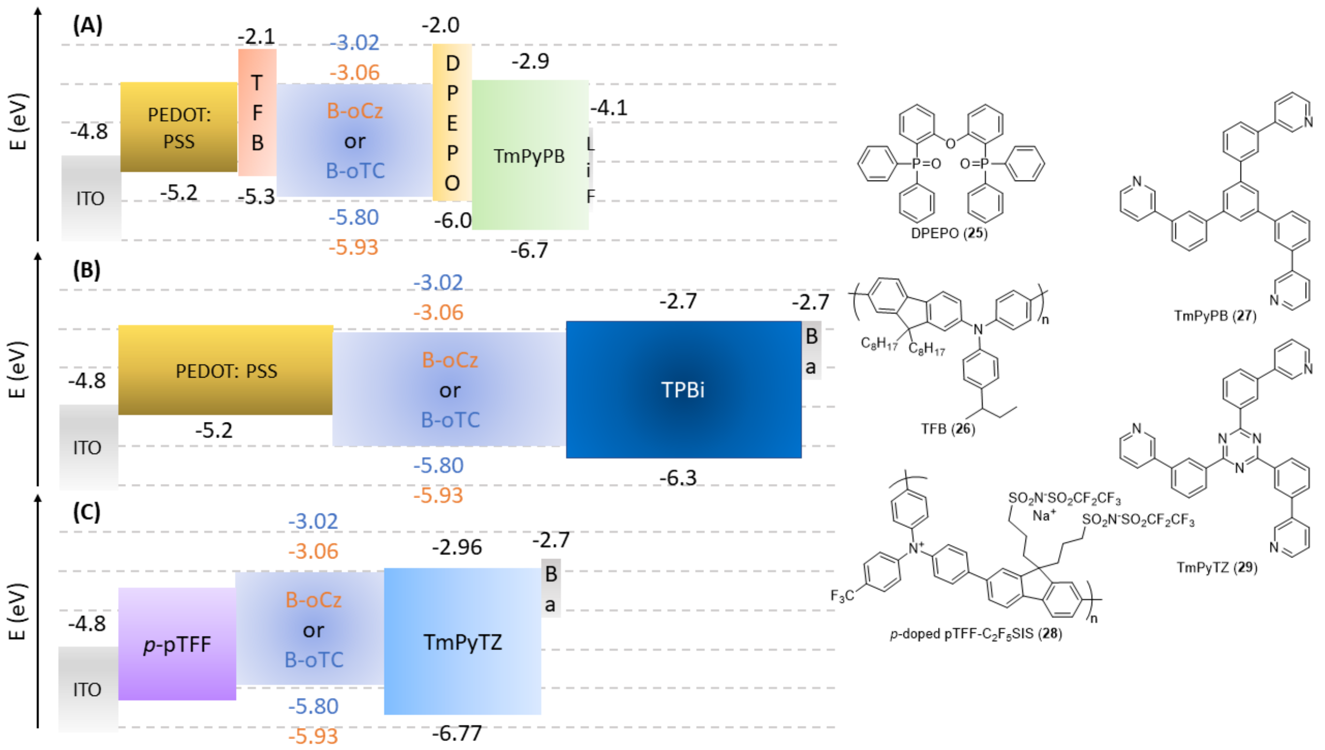

Figure 4.15: Comparison of different organic light-emitting device structures. **(A)** from literature[3]. **(B)** thermally-evaporated OLED, first batch. **(C)** thermally-evaporated OLED, second batch.

In the second attempt to build a thermally-evaporated OLED, *p*-doped poly-(9,9-bis-(3-(pentafluoroethanesulfonyl-imidosulfonyl)propyl)fluorene-2,7-diyl-*alt*-1,4-phenylene-(*para*-trifluoromethylphenylimino)-1,4-phenylene) sodium salt (*p*-pTFF, **28**) was used as a hole-transport layer. With its workfunction of 5.85 eV[47], it should be able to inject the holes much better in the emissive layer then PEDOT:PSS (**23**). As a second change to the first batch of thermally-evaporated OLED, TPBi (**24**) was replaced by 2,4,6-tris(3-(pyridine-3-yl)phenyl)-1,3,5-triazine (TmPyTZ **29**) to avoid the trapping of the excitons in the triplet state of TPBi (**24**). Additionally, the thicknesses of the different organic layers were decreased to apply lower voltages during the measurements. In comparison to the device structure, the second batch of thermally-evaporated OLED was quite similar to the literature. Poly(9,9-dioctylfluorene-2,7-diyl-1,4-phenylene-N-(*para*-sec-butylphenyl)imino-1,4-phenylene) (TFB, **26**) is a derivative of pTFF (**28**) and works as hole-transport layer as well as an electron-blocking layer. As an electron-transport, layer Lu and his coworkers used 3,3'-(5'-(3-(pyridine-3-yl)phenyl-[1,1',3',1''-terphenyl]-3,3''-diyl)dipyridine (TmPyPB, **27**) which has quite similar energy levels as the used TmPyTZ (**29**). As an additional hole-blocking layer (oxybis(2,1-phenylene))bis(diphenylphosphine oxide) (DPEPO, **25**) was used in the literature and missing in the fabricated OLED. The resulting performance of the OLED is shown in Figure 4.16.

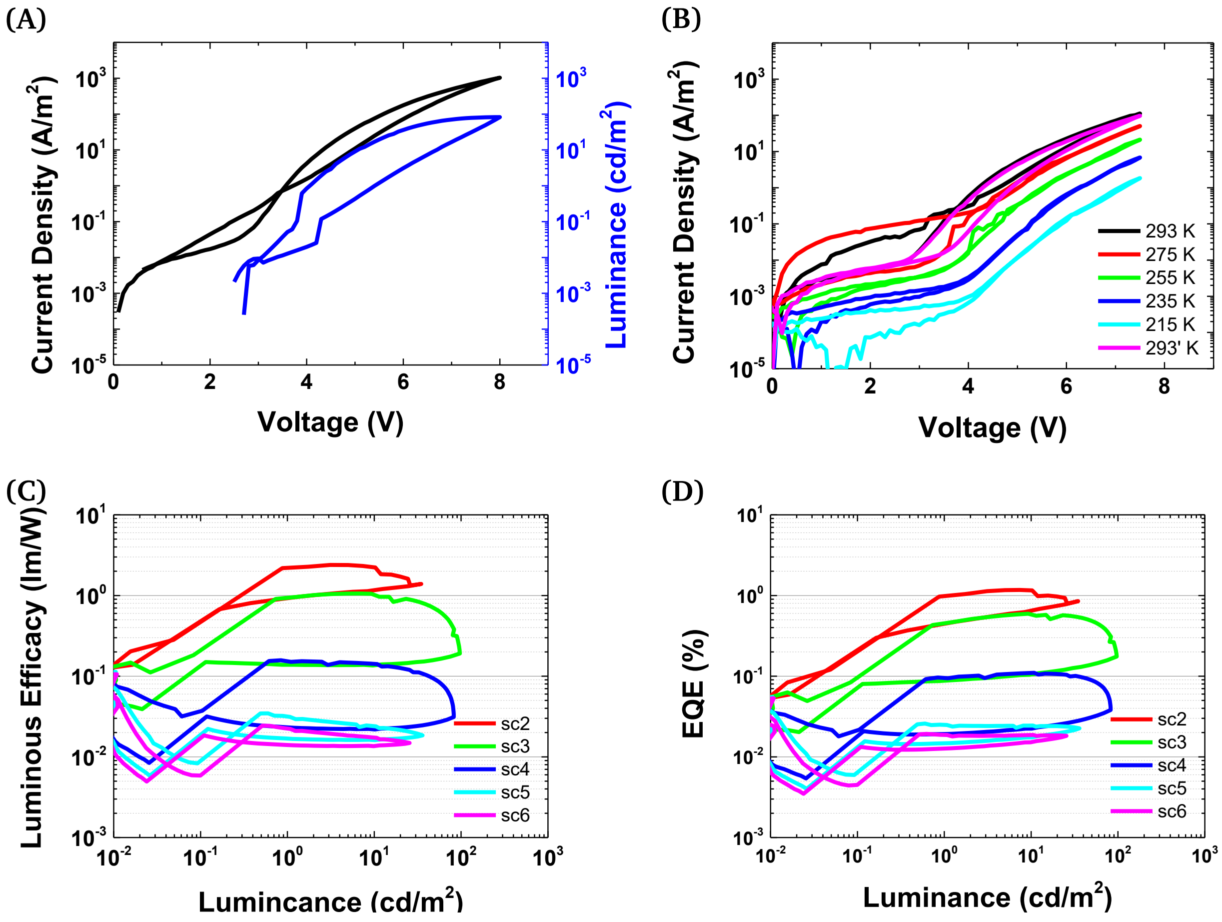

Figure 4.16: Photophysical results of a thermally-evaporated organic light-emitting diode based on B-oCz (**8a**). **(A)** current density (black) and luminance (blue) at 8 V in one plot. **(B)** temperature dependence of current density at 7 V. Luminous efficacy **(C)** and external quantum efficiency **(D)** versus luminance.

Using pTFF (**28**) as a hole-transport layer and TmPyTZ (**29**) as an electron-transport layer resulted in the same current density at the same voltage and a decreased luminance of around one order of magnitude (**A**). Besides, the luminous efficacy is nearly doubled in this OLED but shows a more significant degradation effect. For this OLED, an EQE of around 1 % could be achieved, which is a bit lower than the EQE, afforded with PEDOT:PSS (**23**) and TPBi (**24**) as a hole- and an electron-transport layer. Also, the degradation effect of this new LED is much more significant and results in a loss of around two orders of magnitude in the efficiencies. This degradation process could also be seen in the temperature-dependent *J*-*V* curves, too. In the case of B-oTC (**8b**), these effects are even more reliable

(Figure 9.44, page y), resulting in a maximum EQE of 1 %, which is only a third of the first batch of thermally-evaporated OLEDs. To get an impression, if the new device structure removed the second emission of TPBi (**24**) in the EL spectra, new EL spectra were measured (Figure 4.17).

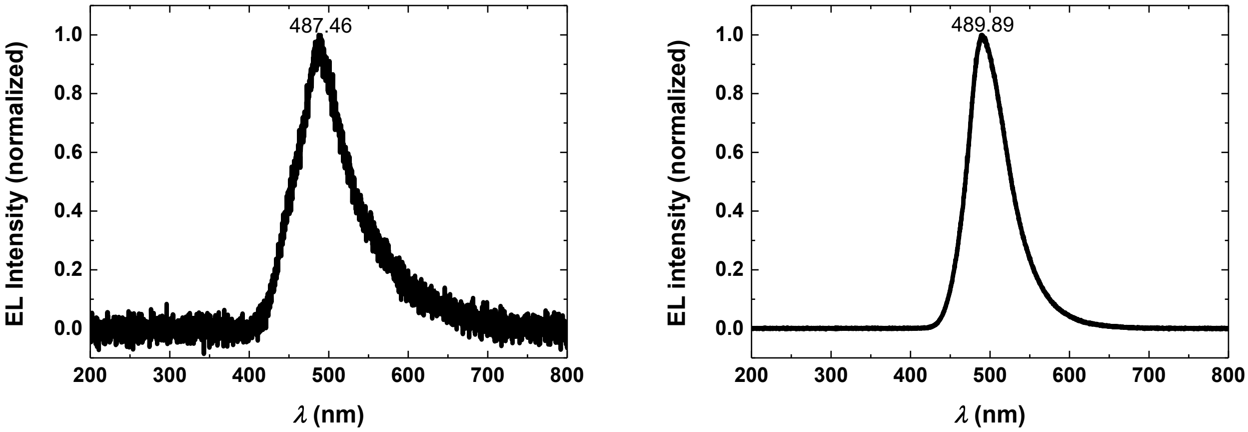

Figure 4.17: Normalized electroluminescence spectra of a thermally-evaporated OLED based on B-oCz (**8a, left**) and B-oTC (**8b, right**).

In both EL spectra the second emission of TPBi (**24**) was not observed. The maximum wavelengths is not in agreement to literature[3] and reproduced the results of the solution-processed OLEDs. To compare the results of all fabricated devices, they are summed up in Table 4.2.

Table 4.2: **Device 1:** spin-coated LED with the structure PEDOT:PSS/emitter/TPBi/Ba/Al. **Device 2:** thermally-evaporated LED with the structure PEDOT:PSS/emitter/TPBi/Ba/Al. **Device 3:** thermally-evaporated LED with the structure pTFF/emitter/TmPyTZ/Ba/Al. **[a]**: maximum luminance. **[b]**: turn-on voltage. **[c]**: maximum luminous efficacy. **[d]**: maximum EQE. **[e]**: EL maximum.

Device	$L_{\max}$[a] / cd/m^2	V[b] / V	$LE_{\max}$[c] / lm/W	EQE$_{\max}$[d] / %	λ[e] / nm
1 – B-oCz (**8a**)	63	5.6	1.4	1.1	485.24
1 – B-oTC (**8b**)	57	4.9	4.2	1.5	489.89
2 – B-oCz (**8a**)	1588	3.1	3.4	1.8	483.82
2 – B-oTC (**8b**)	2464	5.0	4.3	3.3	489.86
3 – B-oCz (**8a**)	82	2.7	2.4	1.2	487.46
3 – B-oTC (**8b**)	1158	4.5	0.7	1.1	489.89

It is possible that the recombination of the charge carriers did not take place in the middle of the OLED, rather at a surface between two different layers. This could explain why Lu and his coworkers used TFB

(**26**) as an additional electron-blocking layer and DPEPO (**25**) as an additional hole-blocking layer. Furthermore, the general lousy device performance can be explained in that regard. These two different layers usually were not to be used in an OLED based on polymers, which is the reason these layers were not used in the fabricated OLEDs.

4.4 Results of the synthesis and spectroscopic characterization of the polymers

As a completely new part of this project, the small molecules B-oCz (**8a**) and B-oTC (**8b**) should be building blocks for polymers. Related to the synthesis steps, this chapter is subdivided into three different subsections. At first the halogenation attempts of the small molecules **8a** and **8b** for the subsequent addition of a polymerizable group on these molecules are described. The following subsection describes the attempts of an addition of a polymerizable group on B-oCz (**8a**) and B-oTC (**8b**). In the final subsection of this chapter, the synthesis and a first spectroscopic characterization of the polymer are described.

4.4.1 Halogenation of B-oCz and B-oTC

A rather simple way of adding a polymerizable group to the small molecules B-oCz (**8a**) and B-oTC (**8b**) is the halogenation of these molecules. Therefore, different methods were tried using N-bromo-succinimide (NBS, **30a**) and N-iodo-succinimide (NIS, **30b**). The different halogenation attempts are shown in Scheme 4.3.

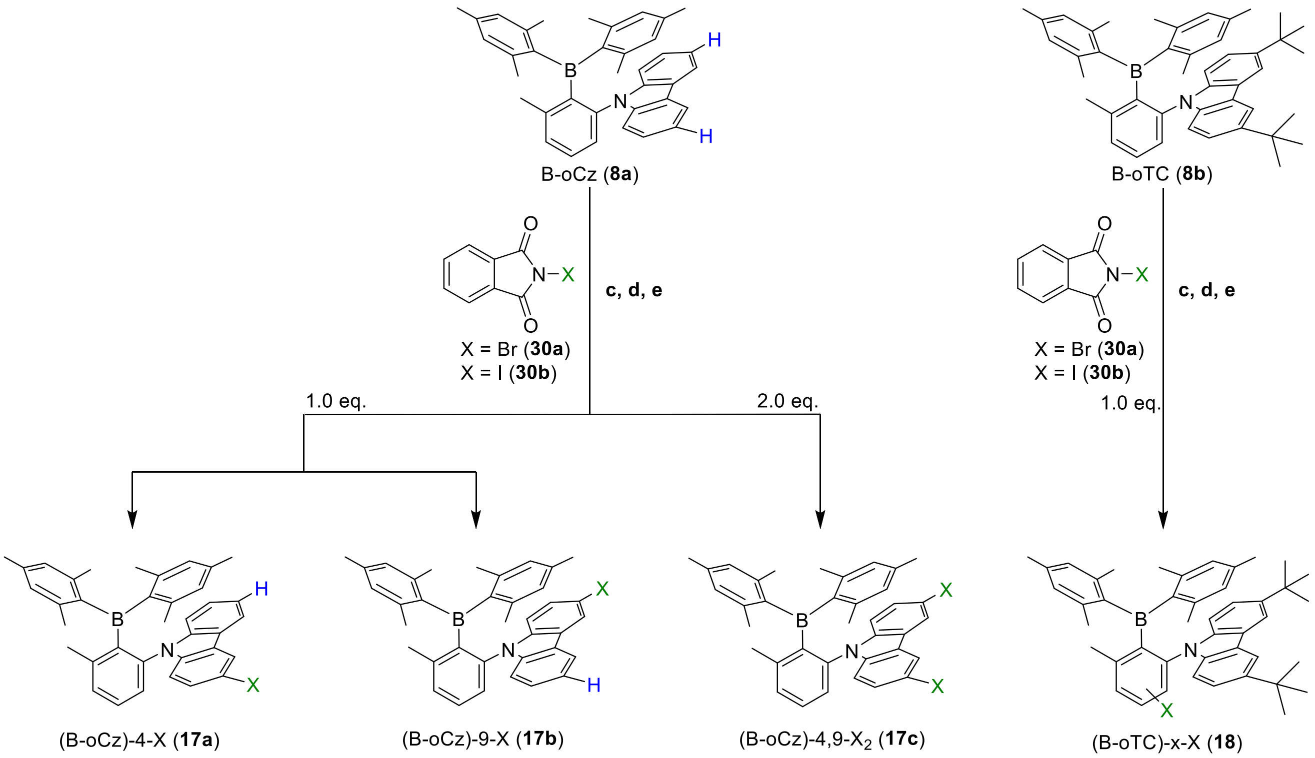

Scheme 4.3: Different halogenation attempts of B-oCz (**8a**) and B-oTC (**8b**) by using NBS (**30a**) and NIS (**30b**) under different conditions. **c) 30a**, $CHCl_3$, 60 °C, 2 d, yield: 69.8 % (**17a + 17b**), 77.4 % (**17c**), 71.6 % (**18**). **d) 30a**, DCM, $AuCl_3$, 60 °C, overnight, yield: 12.9 % (**17a + 17b**), 82.0 % (**17c**), 4.6 % (**18**). **e) 30b**, DMF/DCM (1:2, v:v), 60 °C, 1 week, no yield obtained.

All reactions were monitored by using ^{1}H-NMR spectroscopy. Unfortunately, no conversion was obtained by using NIS (**30b**) as halogenation reagent. The bromination reactions were purified by flash column chromatography and gel permeation chromatography. Regarding the ^{1}H-NMR spectrum (shown in Figure 9.23, page l), a product mixture of different substitution patterns or other products was afforded. In the case of the mono-bromination of B-oCz (**8a**), two different species could be identified in the ^{1}H-NMR, shown in Figure 4.18.

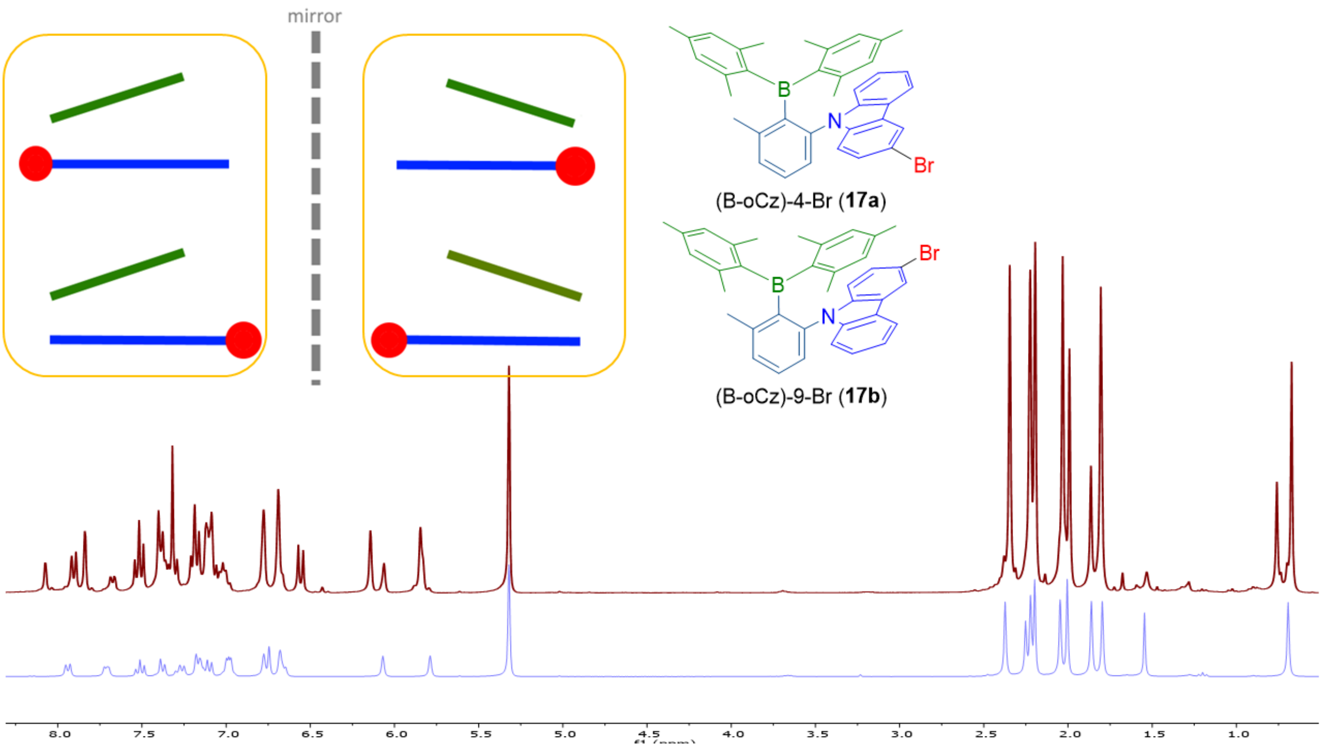

Figure 4.18: Different products of mono-bromination of B-oCz (**8a**). **Blue:** ^{1}H-NMR spectrum of B-oCz (**8a**). **Red**: ^{1}H-NMR spectrum of product mixture containing (B-oCz)-4-Br (**17a**) and (B-oCz)-9-Br (**17b**).

Shown in Figure 4.18, the bromine can attack the front side or the backside of the carbazole of B-oCz (**8a**), resulting in two different isomers with a rate of around 1:2 of **17a** to **17b**. Using $AuCl_3$ as a catalyst should increase the selectivity of the bromination, but unfortunately, the same ratio could be afforded. To verify the brominated small molecules **17a**, **17b,** and **18,** a mass spectrum with an atmospheric pressure chemical ionization source was measured. The different spectra are depicted in Figure 4.19.

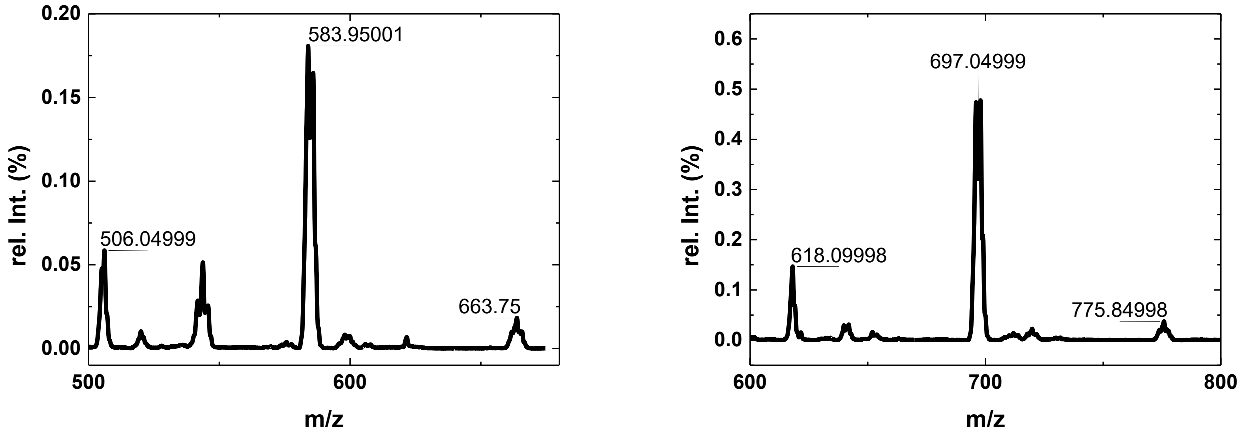

Figure 4.19: Atmospheric pressure chemical ionization mass spectra of (B-oCz)-4-Br/(B-oCz)-9-Br(**17a** and **17b, left**) and (B-oTC)-x-Br (**18, right**).

For the mono-brominated B-oCz (**8a**), (B-oCz)-4-Br (**17a**) and (B-oCz)-9-Br (**ent-17a**), a molecular weight of around 584 g/mol was expected and for the mono-brominated B-oTC (**8b**), (B-oTC)-x-Br (**18**), a molecular weight of 697 g/mol. Unfortunately, in both spectra, the small molecules **8a** (506 g/mol) and **8b** (618 g/mol), as well as multiple brominated species, are still in the product mixture after purification. An additional problem for (B-oTC)-x-Br is the unknown substitution pattern, which cannot be identified by using standard NMR techniques. Besides these, for (B-oCz)-4-Br (**17a**) and (B-oCz)-9-Br (**17b**), a SUZUKI cross-coupling reaction was tried in a small test batch. The reaction sequence can be seen in Scheme 4.4.

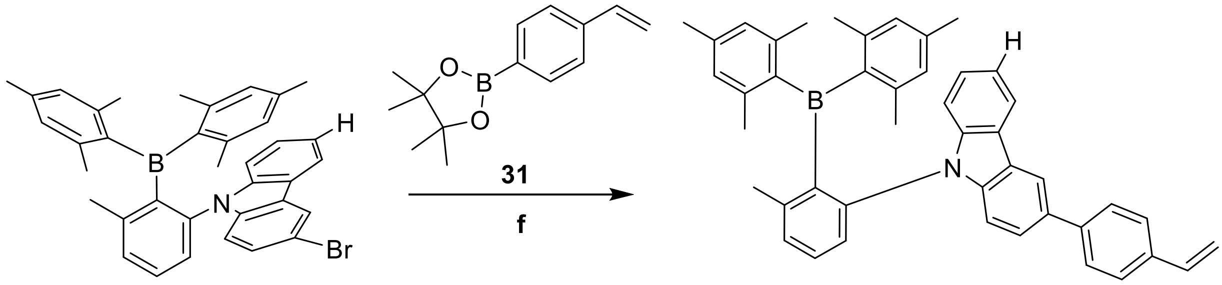

(B-oCz)-4-Br (**17a**)

(B-oCz)-4-St (**15a**)

Scheme 4.4: SUZUKI cross-coupling reaction of (B-oCz)-4-Br (**17a**) with 4-BPinSt (**31**). **f) 31**, Na_2CO_3, $Pd(PPh_3)_4$, H_2O/toluene (1:1, v:v), 120 °C, 48 h, yield: only for mass spectrum. For clarity, only one possible halogenic compound is shown.

In principle, a SUZUKI cross-coupling reaction couples an organic halogenic compound with a boronic acid under basic conditions. Here, the organic halogenic compound was the mixture of **17a** and **17b** and 4,4,5,5-tetramethyl-2-(4-vinylphenyl)-1,3,2-dioxaborolane (4-BPinSt, **31**) as boronic acid to get (B-oCz)-4-St (**15a**) and (B-oCz)-9-St (**15b**) as the product of a SUZUKI cross-coupling reaction. As can be seen in the ^{1}H-NMR (Figure 9.32, page p) and the mass spectrum (Figure 4.20), the product was obtained, but the yield was too low for polymerization.

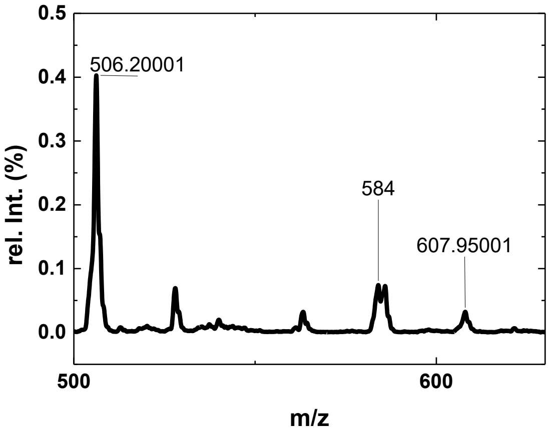

Figure 4.20: Atmospheric pressure chemical ionization mass spectrum of (B-oCz)-4-St (**15a**) and (B-oCz)-4-St (**15b**).

On the one hand, Figure 4.20 shows that the reaction in principle took place. On the other hand, some starting material is left (m/z ((B-oCz)-Br) = 584.4) and could be detected, too. The optimization of the reaction conditions was not done so far.

In comparison to the mono-bromination of the small molecules **8a** and **8b**, the bromination of B-oCz (**8a**) with two equivalents of NBS (**30a**) worked out and resulted in high yields and suitable purities. Only minimal amounts of starting material (**8a**), mono-brominated, and over-brominated species can be seen in the mass spectrum (Figure 4.21). The expected mass for (B-oCz)-4,9-Br_2 (**17c**) is around 663 g/mol and could be found in this spectrum.

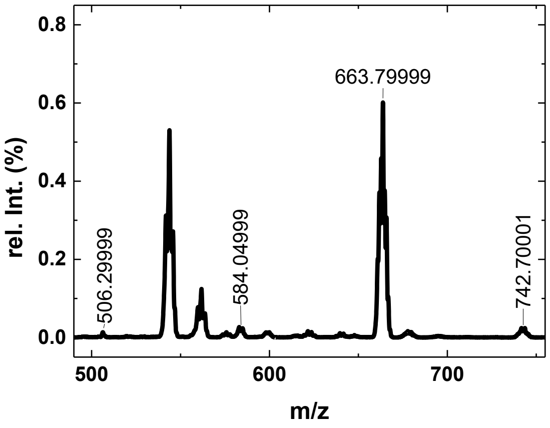

Figure 4.21: Atmospheric pressure chemical ionization mass spectrum of (B-oCz)-4,9-Br_2 (**17c**).

(B-oCz)-4,9-Br_2 (**17c**) was the only compound, which formed single crystals, which could be used for further structure analysis. In collaboration with Prof. Dr. KLAUS MÜLLEN and Dr. DIETER SCHOLLMEYER, it was possible to get an X-ray crystal structure of this molecule (Figure 4.22).

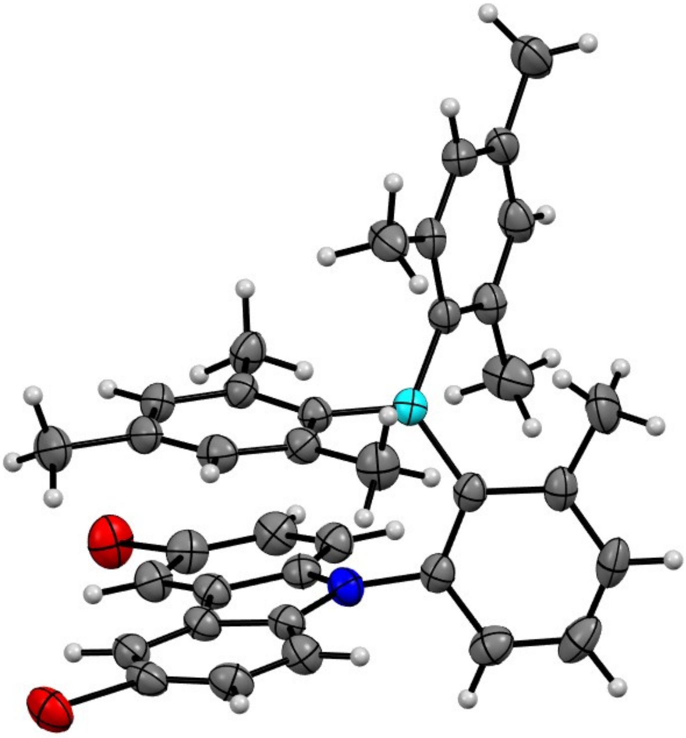

Figure 4.22: X-ray crystal structure of (B-oCz)-4,9-Br_2.

The crystal structure of (B-oCz)-4,9-Br_2 (**17c**) confirmed the addition of the bromines expectedly. With this in mind, (B-oCz)-4,9-Br_2 (**17c**) could be used for a YAMAMOTO condensation, leading to a homopolymer, depicted in Scheme 4.5.

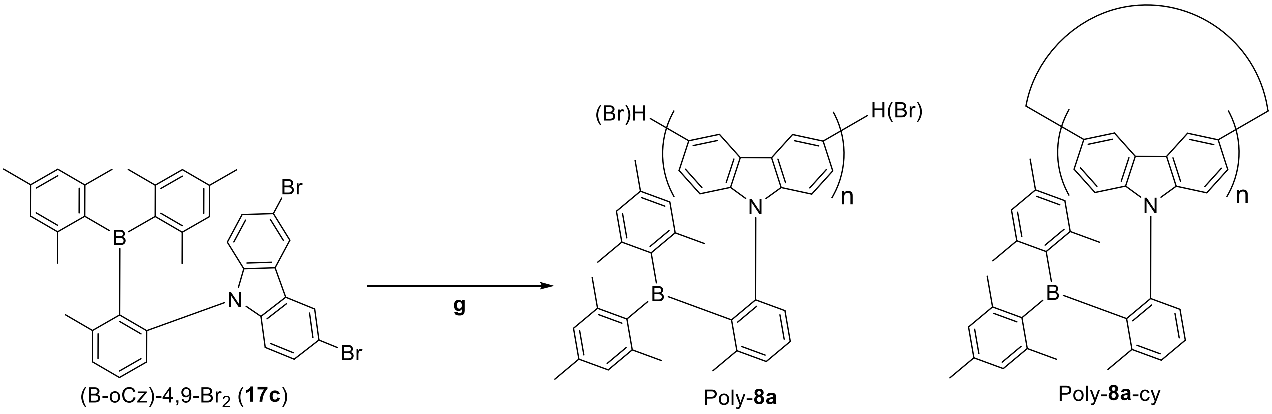

Scheme 4.5: YAMAMOTO condensation of (B-oCz)-4,9-Br_2 (**17c**). **g)** $Ni(COD)_2$/COD/BPY (2.5:2.5:2.5), DMF/toluene (1:1, v:v), 90 °C, 48 h, yield: 3.6 %.

For this polymerization bis(1,5-cyclooctadiene)nickel ($Ni(COD)_2$) was used as catalyst in combination with 1,5-cyclooctadiene (COD) and 2,2'-bipyridine (BPY) as ligands. The crude product of Poly-**8a** was first purified by filtering through a syringe filter to get rid of the catalyst. Afterward, it was purified by

Soxhlet extraction with methanol and acetone as solvents. The analytical GPC elugrams after the single purification steps are shown in Figure 4.23. The dotted lines are showing the removed fractions of the crude product, while the bold curves are normalized to the maximum of the crude product.

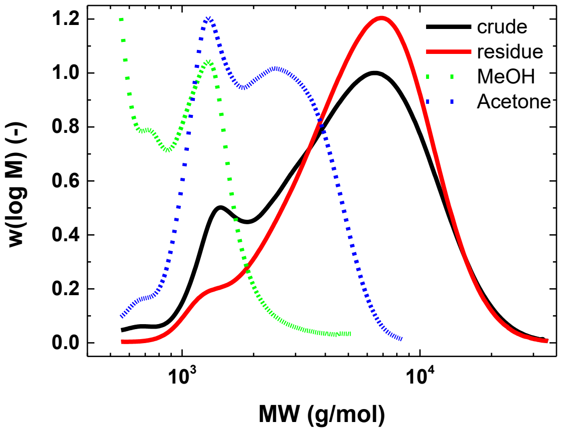

Figure 4.23: Results of analytical GPC of Poly-(B-oCz) (Poly-**8a**).

After polymerization (black), only low molecular weights (M_n = 3559.94 g/mol, M_w = 6038.14 g/mol) were obtained with a good dispersity of 1.70 in toluene/DMF at 90 °C. Several Soxhlet extractions could improve this with methanol (green) and acetone (blue), resulting in molecular weights of M_n = 4344.34 g/mol, M_w = 6704.76 g/mol and dispersity of 1.54 (red). Considering a molecular weight for one repeating unit of 503.3 g/mol, this led to a chain length of nine repeating units. By taking a picture of the obtained green-yellowish material under UV-light, a bright green color could be seen (Figure 4.24).

Figure 4.24: Photograph of the residue after Soxhlet extraction under UV irradiation at 356 nm.

The structure of Poly-**8a** was characterized by NMR spectroscopy and matrix-assisted laser desorption/ionization time-of-flight (MALDI-TOF) mass spectrometry. For a more straightforward assignment of the signals, the NMR spectra of the oligomer were compared to B-oCz (**8a**) and (B-oCz)-4,9-Br₂ (**17c**). The comparison of the different ^{1}H-NMR spectra is shown in Figure 4.25. For clarity, only the range of 5.6 ppm to 8.8 ppm is shown.

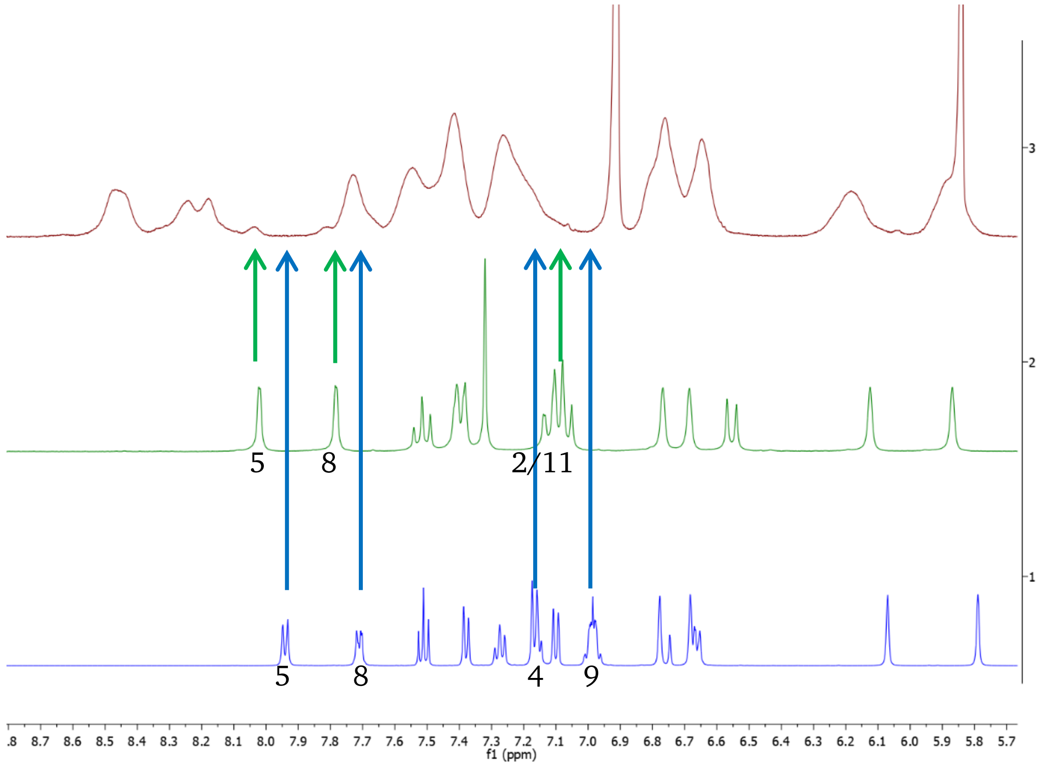

Figure 4.25: Comparison of ^{1}H-NMR spectra of B-oCz (**8a**, blue), (B-oCz)-4,9-Br₂ (**17c**, green) and Poly-**8a** (red).

No end group signals in Poly-**8a** could be identified by comparing the ^{1}H-NMR spectra of all three compounds to each other. A comparison between the different carbon NMR spectra should help to identify the endgroup of Ploy-**8a**, which is shown in Figure 4.26.

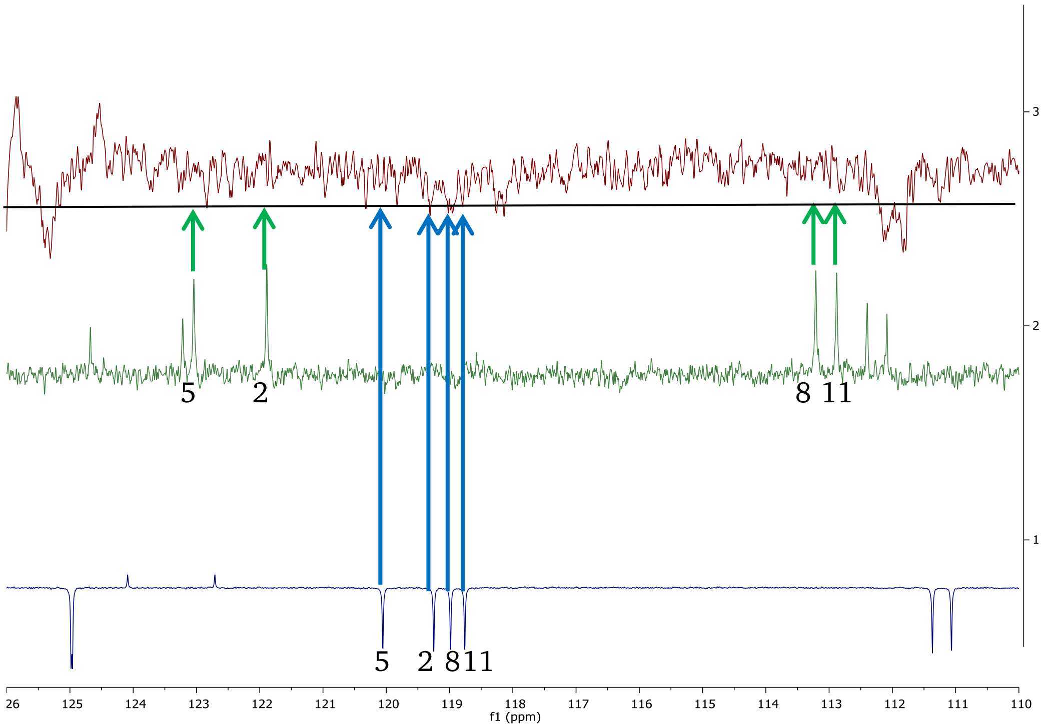

Figure 4.26: Comparison of ^{13}C-NMR spectra of B-oCz (**8a**, blue), (B-oCz)-4,9-Br$_2$ (**17c**, green) and Poly-**8a** (red). Black line is used as a reference line for baseline.

As well as shown in the ^{1}H-NMR spectra, no specific end group for Poly-**8a** could be detected in the carbon NMR spectrum. These results led to the idea of a cyclic structure, which was already reported in the literature that is using YAMAMOTO condensation for functionalized carbazoles, too.[48,49] To get an idea of how to analyze the MALDI-TOF mass spectrum of Poly-**8a**, the different possibilities of an end group and the repeating unit are shown in Figure 4.27.

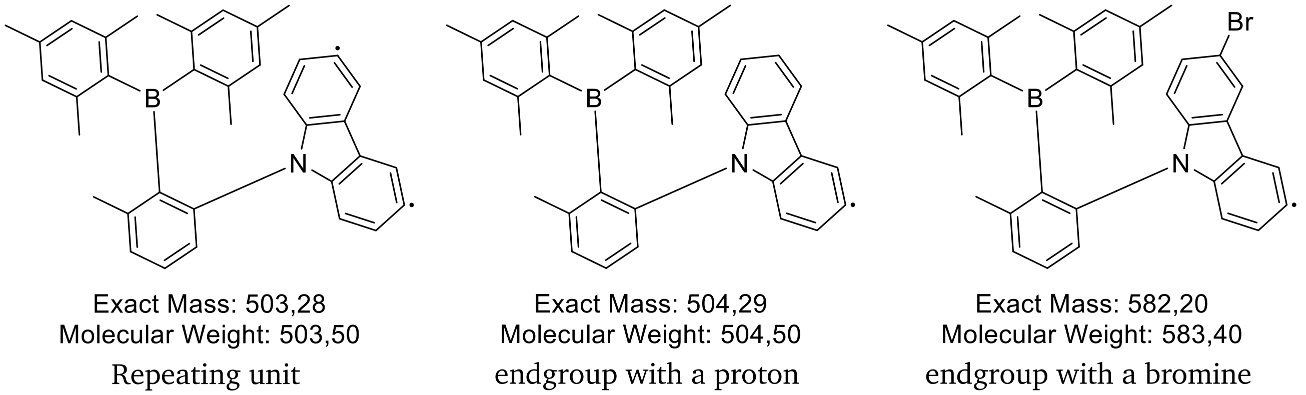

Figure 4.27: Molecular weights and exact masses of the repeating unit and the different endgroups of Poly-**8a**.

The different possible endgroups can form in different ways. In the expected result of a YAMAMOTO condensation reaction, bromine should appear as a functional endgroup. In the case of only monobrominated starting material like (**17a** and **17b**), an additional quenching reaction can take place and results in a proton as an endgroup.

By analyzing the MALDI-TOF mass spectrum, depicted in Figure 4.28, it can be seen that the peak of the cyclic tetramer (m/z = 2013.27) is dominating the spectrum. However, there were also macrocycles of around $n = 18$ ($M_{n=18} = 9059.4$ g/mol) are formed, too.

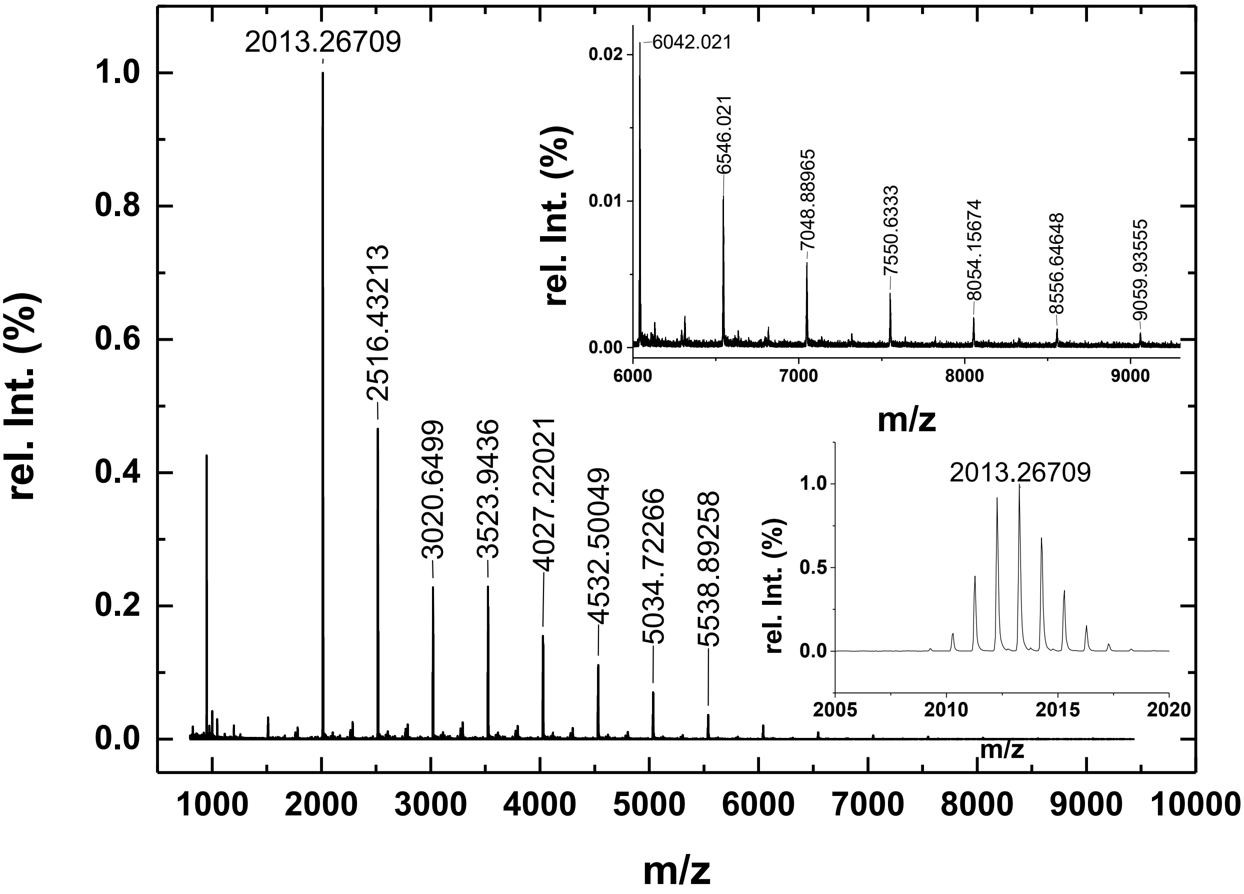

Figure 4.28: MALDI-TOF mass spectrum of Poly-**8a**. Upper right corner: expansion of the range 6000 ≤ m/z ≤ 9500. Right corner on the bottom: expansion of the peak at an m/z of 2013.27.

By the NMR spectra, no further open-chain linear structures could be found, because the H_5 and H_8 protons are located inside the ring. This position leads to a deshielding effect on the two protons H_5 and H_8, causing the signal at 8.37 ppm in a tetrameric cycle, whereas these protons are causing the signal in the region of 7.95 – 8.22 ppm for bigger macrocycles. The degree of polymerization determined by the ^{1}H-NMR spectra is around ten if the broad signals at 5.89 ppm and 6.16 ppm are used as a reference, which led to a molecular weight of 5033.0 g/mol. Comparing the determined repeating units and the molecular masses by GPC, NMR, and MALDI-TOF mass spectrum, GPC and NMR are quite close to each other. Only the determined molecular weight determined by MALDI-TOF mass spectrum was a bit higher. The reason could be that larger macrocycles are inadequately represented in the MALDI-TOF mass spectrum. Nevertheless, the molecular weights determined by GPC had a maximum of up to 20000 g/mol, which is significantly higher than the molecular weight of the cyclic tetramer Poly-**8a**-cy.

To get an impression about the distribution of HOMO and LUMO in Poly-**8a**-cy and the energy level of the excited singlet and the excited triplet state, the cyclic tetramer was calculated by using DFT calculations. For a comparison to B-oCz (**8a**), the same levels of theory were for (TD)-DFT calculations. The results for Poly-**8a**-cy are depicted in Figure 4.29.

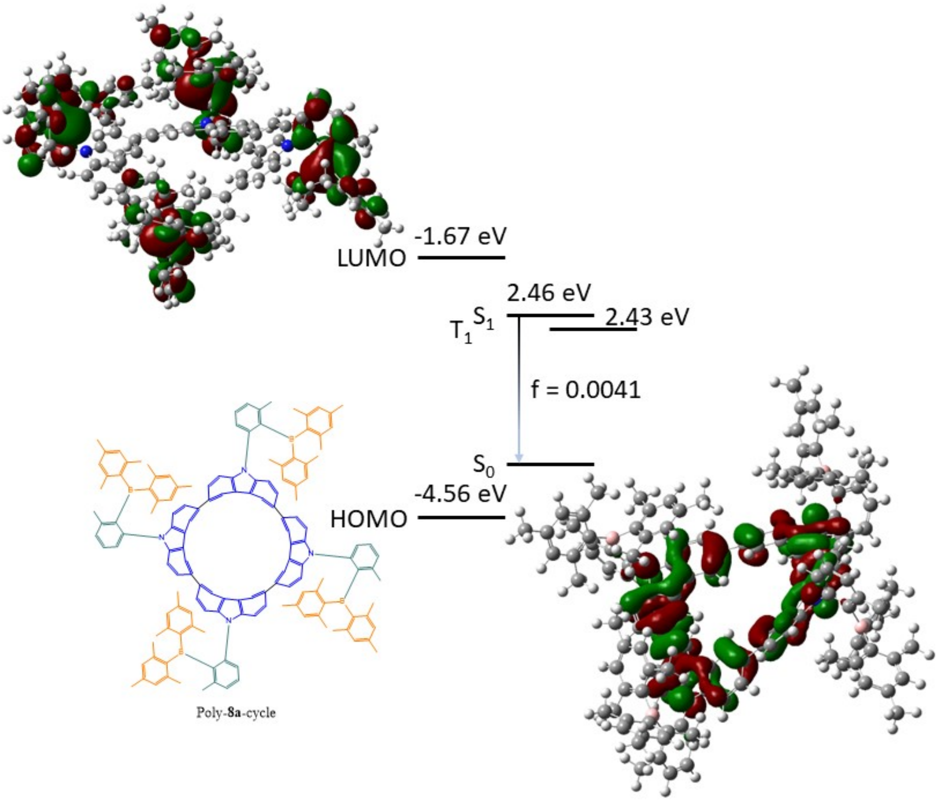

Figure 4.29: Chemical structure of Poly-**8a**-cycle and its frontier HOMO and LUMO. In addition to the structure, the energy level diagram for the HOMO and LUMO, as well as the low-lying singlet (S_1) and triplet excited (T_1) states, are shown together with the oscillator length *f*.

For the tetramer of the Poly-**8c**-cy, a ΔE_{ST} of 0.03 eV could be calculated. In comparison to B-oCz (**8a**), this value was significantly decreased and should show a TADF behavior in further investigations. It was remarkable that the energy level of HOMO was significantly increased compared to the ones in the small molecules **8a** and **8b**, which explains the color shift from the fluorescence from blue to green. Further on, the HOMO and LUMO were well separated on the donor and acceptor moieties like in the molecules before polymerization.

For a first photophysical characterization, UV/Vis spectra, PL, and PLQY were measured in oxygen-free toluene for this molecule. The spectroscopic results are depicted in Figure 4.30.

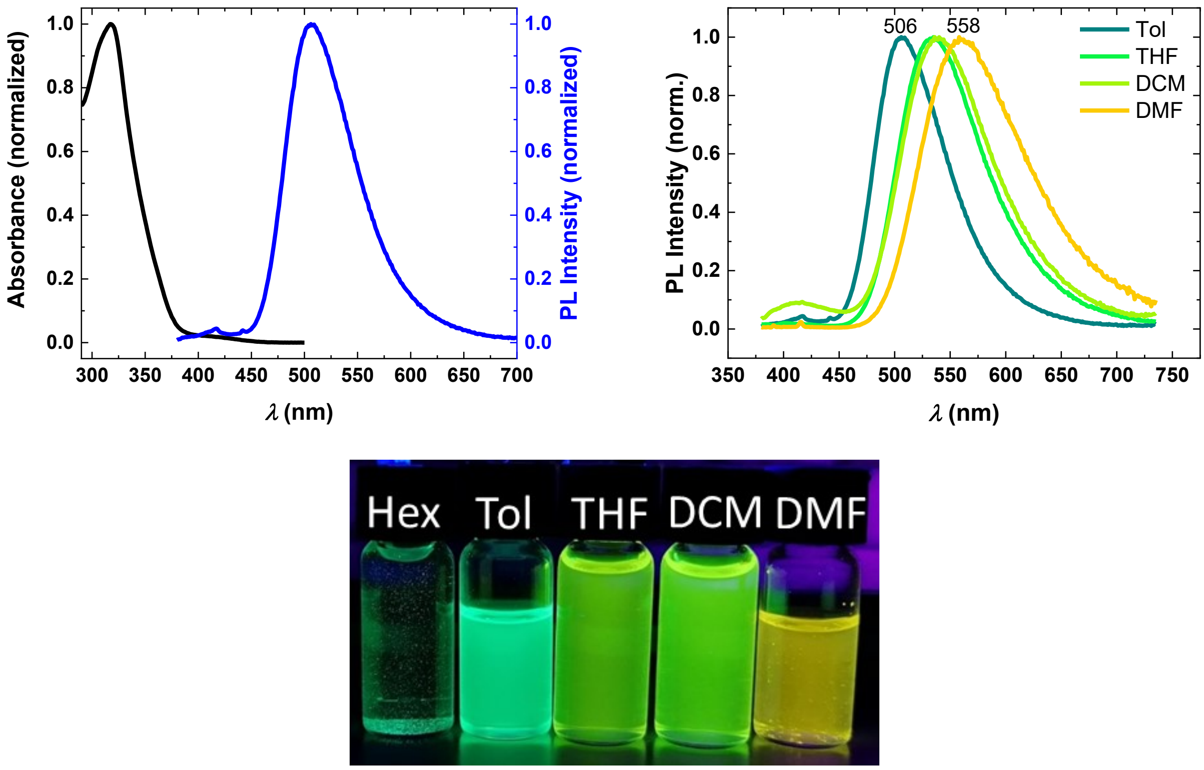

Figure 4.30: Spectroscopic results of Poly-**8a**-cycle. **Upper left:** UV/Vis spectrum (black) and PL spectrum (blue) in oxygen-free toluene. **Upper right:** PL spectrum in different degassed solvents. **Down:** photograph of Poly-**8a**-cycle in different solvents under irradiation at 356 nm.

In comparison to B-oCz (**8a**), Poly-**8a**-cy showed only one absorption feature in the UV/Vis spectrum (black) with a maximum at a wavelength of 317 nm. Additionally, a small broad shoulder around 400 nm could be seen for Poly-**8a**-cy following the UV/Vis spectra of B-oCz (**8a**). This shoulder was related to the intramolecular charge-transfer transitions caused by the donor-acceptor arrangement in the chemical structure. The PL spectrum (blue) showed a structureless PL band with its maximum at 506 nm and was shifted around 26 nm to the green region of the spectrum in comparison to B-oCz (**8a**). For another indication of the TADF properties of Poly-**8a**-cy, the PL spectrum was measured in different solvents with different polarities (toluene < THF < DCM < DMF). The positive correlation between the increasing polarity of the solvents and the maximum wavelength is characterized as solvatochroism, which indicated a charge-transfer property of the synthesized polymer. The estimated PLQY of Poly-**8a**-cy in oxygen-free toluene was around 22.4 %, which is much lower than the PLQY of B-oCz (**8a**) in the same solvent. Further investigations of the properties and the confirmation of TADF properties using temperature and time-dependent spectroscopy of Poly-**8a**-cy could not be done in this project due to time constraints.

5 Conclusion and outlook

The topic of this master thesis was the synthesis of novel polymers with thermally activated delayed fluorescence (TADF) for the application as an emissive layer in organic light-emitting diodes (OLEDs). For this purpose, the research areas involved everything from the theoretical calculations of individual molecules using (time-dependent)-density functional theory (TD-DFT) calculations to the synthesis of various compounds and the fabrication of OLEDs.

Using (TD-)DFT calculations at the B3LYP/6-31G(d) theory level enabled the calculation of different energy states like the energy levels of the highest occupied molecular orbital (HOMO) and the lowest unoccupied molecular orbital (LUMO) of the synthesized small molecules and the polymer. Additionally, the energy levels of the lower excited singlet states and the lower excited triplet state were calculated, which have been used for the calculation of the energy gap between these two states (ΔE_{ST}). In the context of these calculations, a value of ΔE_{ST} smaller than 0.1 eV was determined for all calculated molecules, which is a rough guide for molecules with TADF properties. Besides, the optimized structures showed that the HOMO is well separated from the LUMO.

After sublimation of B-oCz (**8a**) and B-oTC (**8b**), they were used for the fabrication of different device structures. Therefore, the devices were fabricated by solution-processed and thermally-evaporation methods. Additionally, different device structures were tested for the thermally-evaporated OLEDs. Although the devices' performance did not approach that of the literature[3], they were the first blue emitters, which were successfully used in an OLED in this group. The efficiencies of the different devices can be improved by adding further layers such as hole-blocking layer and electron-blocking layer, although such a multi-layer structure would certainly not be necessary for later polymers based on these small molecules B-oCz (**8a**) and B-oTC (**8b**).

The main part of this master thesis was the synthesis of two different small molecules and their transfer into a polymer. Therefore, the two literature-known small molecules 9-(2-(dimesitylboraneyl)-3-methylphenyl)-9*H*-carbazole (B-oCz, **8a**) and 3,6-di-*tert*-butyl-9-(2-(dimesitylboraneyl)-3-methylphenyl)-9*H*-carbazole (B-oTC, **8b**) were synthesized and used for further reactions. To transfer these two small molecules into a polymer, different halogenation reactions with N-bromo-succinimide and N-iodo-succinimide were investigated. In contrast to the iodination reactions, the brominations showed a conversion to the desired products, but only the debromination of B-oCz (**8a**) was successful. However, for the mono-brominated B-oCz (**8a**), a SUZUKI cross-coupling reaction was done for a proof of concept and showed that it is possible to add styrene on the donor moiety of this small molecule. With the optimization of the purification of the mono-bromination reactions and the reaction conditions of the SUZUKI cross-coupling reaction, it should be possible to synthesize a chiral polymer with TADF properties. The main problem of the bromination of B-oTC (**8b**) was the purity of the afforded crude product, where the assignment of the substitution pattern was not possible in the ^{1}H-NMR. After the optimization of the purification, it should be possible to do a SUZUKI cross-coupling reaction, too, to add a functional group for polymerization to B-oTC (**8b**).

However, the dibrominated B-oCz (**8a**) showed high conversions and a good grade of purity. Ongoing with a YAMAMOTO condensation reaction, a green-yellowish polymer could be synthesized, which showed a green fluorescence under irradiation at 356 nm. Structure analysis using NMR spectra, GPC, and a MALDI-TOF mass spectrum revealed that primarily cyclic compounds with up to 18 repeating units were obtained. This cyclic polymer compound was characterized by measuring the UV/Vis spectrum, the PL spectrum, and the PLQY in oxygen-free toluene. Further on, the solvatochromism of this compound could be shown by measuring the PL in different solvents. However, the yield was not high enough so that neither these measurements could be repeated on a quartz substrate nor an OLED could be built. Therefore, the synthesis and purification of the polymer have to be repeated. With enough material, it should be possible to measure UV/Vis- and PL spectra in films and for usage in OLEDs. Using styrene as a host for the polymer should also enable an investigation of the self-quenching processes in this material. If the PLQY is constant despite using a host, no self-quenching processes are taking place, and this polymer-host combination would be the first polymer-based OLED with this property. Further on, it should be possible to use this polymer to synthesize a blue-emitting polymer by using spacer like benzophenone in between the single donor units which interrupt the conjugation of the backbone and decrease the energy level of the HOMO again. If this works and even the device structure is optimized for this material, it could be the first blue polymer with a high EQE showing no self-quenching and would be a great success in the research field of organic light-emitting diodes based on polymers.

6 Experimental section

6.1 Methods and instruments for analysis

6.1.1 Used Chemicals

Used chemicals were from different manufacturers (*Acros Organics*, *Sigma Aldrich*, *TCI,* and others) and used as received, in case of no further descriptions. All chemical experiments were done under an inert gas atmosphere in dried vessels with commonly used SCHLENK technique. As inert gas argon 4.6 (*Westfalen AG*) was used. For air-sensitive reactions or preparation of oxygen-free solvents in the glovebox, the anhydrous solvents were additionally degassed three-times by using the freeze-pump-thaw technique.

6.1.2 Instruments of analysis and methods

For the characterization of the synthesized substances, the following instruments and methods were used. The names of instruments were given with their manufacturers.

Computational methods

All the theoretical calculations were carried out using GAUSSIAN 09 REVISION D.01 WIN 64. The density functional theory (DFT) calculations at the B3LYP/6-31G level were used to optimize the ground state geometries of the investigated compounds. To calculate the singlet- and triplet-energy states time-dependent density functional theory (TD-DFT) calculations were performed at the same level using the optimized ground state geometries. The electron density of molecular orbitals was generated using GAUSSVIEW 5.0 program.

Thin Layer chromatography (TLC)

For qualitative thin layer chromatography, two different coated plates were used. On the one hand, ALUGRAM® SIL G/UV_{254} (*Macherey-Nagel*) plates were used with 0.20 mm of silica oxide on aluminum sheets as the stationary phase. On the other hand, POLYGRAM® ALOX N/UV_{254} (*Macherey-Nagel*) plates were used with a layer of 0.20 mm of neutral Al_2O_3 on polyester. Compounds that are fluorescent under irradiation were detected under irradiation with a UV-lamp (*Vilber Lourmat*) at wavelengths of 254 nm or 365 nm.

Column chromatography

As the stationary phase for column chromatography silica gel 60 (size 40 – 63 μm) (*Mercherey-Nagel*) was used. The separations have been done at room temperature. All solids were placed on the silica gel as dry load. Therefore, the different materials were dissolved in dichloromethane and got adsorbed on silica gel by evaporating the solvent to dryness.

Gel permeation chromatography (GPC)

Preparative

The used GPC system was a LABOACE LC-5060 recycling preparative HPLC System (*Japan Analytical Industry Co., Ltd.*, *JAI*) in combination with two columns JAIGEL-3HR (*JAI*) and JAIGEL-2.5HR (*JAI*) with an exclusions limit of 70000 and 20000, respectively. As a detector system, an UV-VIS4CH LA and RI-700 LA was used (both from *JAI*). For purifications, a concentration of 100 mg material in 1 mL $CHCl_3$ (ROTISOLV® HPLC, *Carl Roth GmbH+Co.KG,* stabilizer: 1 % ethanol) was used.

Analytical

To determine the molecular weights of the polymer compounds and its dispersity, a SHIMADZU recycling-GPC Prominence System (*Shimadzu*) was used. Ms. Sandra Seywald did the measurements in the department of polymer analytics. Therefore, the material was dissolved in THF to get a concentration of 2 g/L. For calibration, polystyrene was used.

Nuclear magnetic resonance spectroscopy (NMR)

NMR spectra were measured at the BRUKER 300 MHZ NMR SPECTROMETER AVANCE, BRUKER 500 MHZ SPECTROMETER AVANCE, and BRUKER 700 MHZ SPECTROMETER AVANCE (all spectrometers are from *Bruker Biospin GmbH)*. The assignments were made with MESTRENOVA 14.1.1 (*Mestrelab*) and TOPSPIN 3.6.1 (*Bruker Biospin GmbH*). The respective measuring frequency, the deuterated solvents used, and the measuring temperature is following the spectroscopic data in brackets in front. The chemical shifts are in parts per million (ppm) relative to the respective undeleted residual signal of the solvent.[50]

CD_2Cl_2: δ (^{1}H-NMR) = 5.32 ppm, δ (^{13}C-NMR) = 53.84 ppm.
THF-d_8: δ (^{1}H-NMR) = 1.72 ppm, δ (^{13}C-NMR) = 25.31 ppm.

The following abbreviations were used to designate the fine structures of the proton signals: s (singlet), d (dublet), t (triplet), pt (pseudo-triplet), m (multiplet). The coupling constants *J* are given in Hertz. The position of the ^{13}C signals was taken from the broadband decoupled spectra, and their assignment was obtained using the 2D spectra. If the assignment of the signals was not possible, a list of the observed signals is given. Both the numbering of the atoms and the labeling of the compounds do not correspond to the IUPAC nomenclature.

UV/Vis spectroscopy

The measurements of absorption spectra in the UV/Vis range of the electromagnetic spectrum was carried out with the LAMBDA 900 instrument (*Perkin Elmer*). For these measurements in solutions, quartz glass cuvettes with a path length of 1 cm are used, for film glass substrates are used, respectively. The solvent and the respective concentration are considered in connection with the spectra in the appendix.

Photoluminescence (PL) and Photoluminescence Quantum Yield (PLQY)

Photoluminescence spectra (PL), as well as the photoluminescent quantum yield (PLQY), were measured with the FLUOROLOG®-3 (*Horiba*). The computer program FLUORESSENCE (*Horiba*) was used to process the measured data. For PL measurements, a quartz glass cuvette was used for solutions, and a quartz glass substrate was used for films that were spin-coated on the surface after UV/ozone treatment (same treatment as for device fabrication). To measure PLQY, an integration sphere was used. Therefore, a small glass tube was used for solutions and a small quartz glass substrate for films. The excitation wavelength and the solvents with the respective concentration are considered in connection with the spectra in the appendix.

Profilometer

The thickness of spin-coated films on glass-substrates was investigated using a DEKTAKXT STYLUS PROFILER (*Bruker*). The films were scratched with a needle, exposing the glass substrate. The surface profiler could then measure the height difference between the film and the glass substrate.

Atomic force microscopy (AFM)

Surface topography of spin-coated molecules films was investigated with a VEECO DIMENSION 3100 AFM system (*Veeco Digital Instruments* by *Bruker*). The morphology was performed using a sharp scanning probe in tapping mode. During measurement, a laser beam is reflected from a cantilever and detected in the electronic feedback loop. The topographical results were depicted in height imaging modes and processed with GWYDDION 2.55 (*Gwyddion*).

Mass spectrometry (MS)

APCI-MS spectra were measured with an EXPRESSION L COMPACT MASS SPECTROMETER quadrupole mass spectrometer (*Advion*). The resulted spectra were processed with the computer program ADVION DATA EXPRESS 4.0.13.8 (*Advion*) and plotted with ORIGIN PRO 9.1 (*Originlab*).

MALDI-TOF MS spectra were measured with a RAPIFLEX MALDI-TOF/TOF MASS SPECTROMETER (*Bruker*). The resulted spectra were processed with the computer program MMASS 5.5.0 (*Bruker*) and plotted with ORIGIN PRO 9.1 *(Originlab*).

X-ray crystallographic analysis

Diffraction data for the compound (B-oCz)-4,9-Br_2 were collected on an STOE IPDS 2T (*Stoe*) diffractometer equipped with graphite monochromated Mo Kα radiation (λ = 0.71073 Å). The structure was solved by the integration method and refined by the full-matrix least-squares method. Hydrogen atoms were added in idealized positions, and all non-hydrogen atoms were refined anisotropically. Details of crystal and structure refinement are listed in Table 6.1.

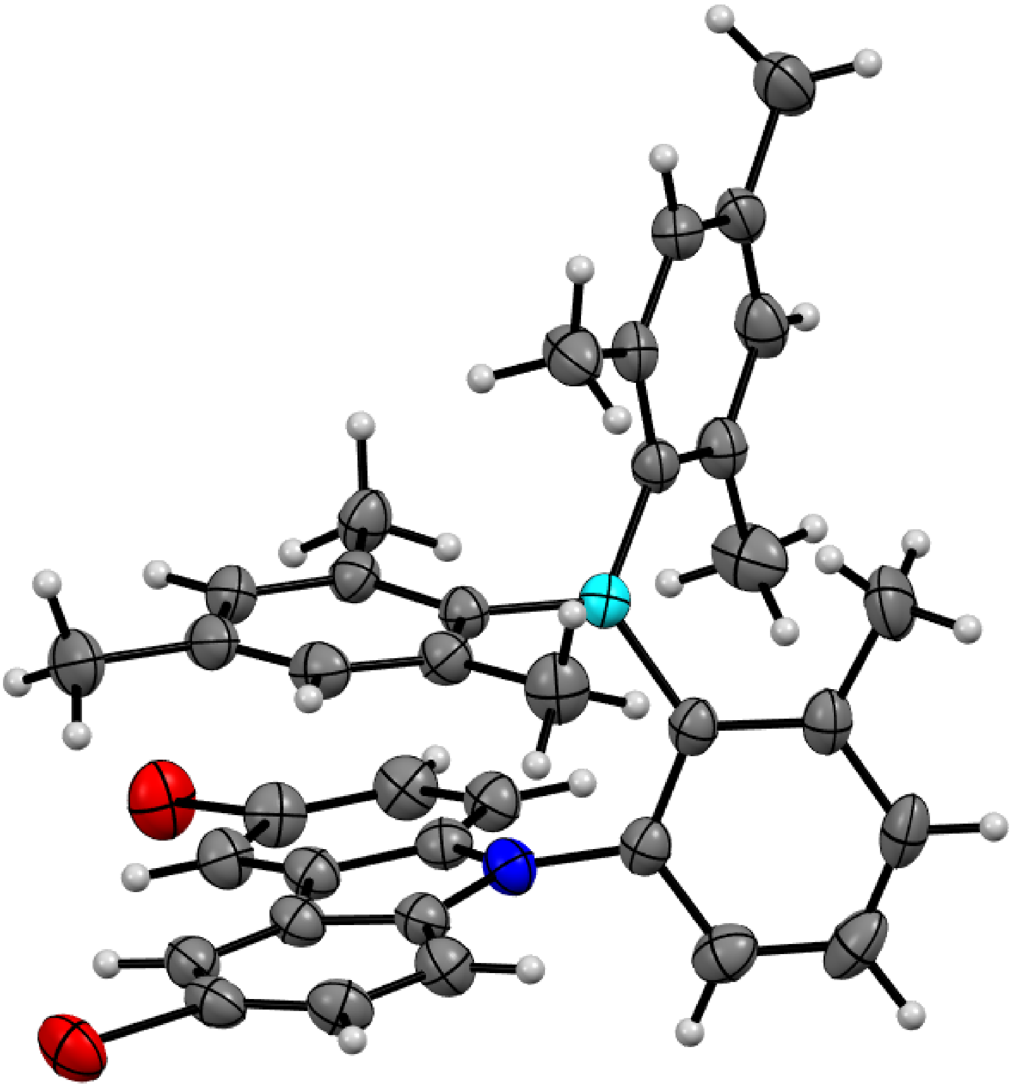

Figure 6.1: Crystal structure of (B-oCz)-4,9-Br_2. Grey: carbon, white: hydrogen, dark-blue: nitrogen, blue: borane, red: bromine.

Table 6.1: Crystal data and structure refinement for (B-oCz)-4,9-Br_2.

Compound	**(B-oCz)-4,9-Br_2**
Empirical formula	$C_{37}H_{34}BBr_2N$
Formula weight	663.28
Crystal system	monoclinic
Space group (Number)	P 21/c, (14)
a (Å)	8.2683(2)
b (Å)	13.4320(5)
c (Å)	27.5514(9)
λ (°)	90
β (°)	93.198(2)
γ (°)	90
V (Å^3)	3055.09(17)
Z	4
ρ_{calc} (g cm^{-3})	1.442
μ (mm^{-1})	2.681
F(000)	1352
Shape and color	colorless block
R_{int}	0.0239
Θ-range (°)	2.806-27.919
GOF on F^2	1.130
R_1 | wR_2 [$l \geq 2\sigma(l)$]	0.0464 | 0.1013
R_1 | wR_2 (all data)	0.0671 | 0.1135

6.2 Device fabrication and characterization

In this project, different devices for the photophysical characterization of the materials were fabricated. Therefore, different layers were used and deposited on the substrates by using different techniques such as spin-coating and thermally-evaporation under a high vacuum.

Hole-only devices (HOD) and organic light-emitting diodes (OLEDs) were fabricated on a 3x3 cm glass substrate with a pre-patterned ITO layer. Electron-only devices (EOD) were fabricated on a 3x3 cm glass substrate for the anode structure aluminum (99 %, *Umicore*) was deposited by thermally-evaporation under high vacuum and subsequently oxidized under air.

Cleaning of the substrates

The preparation of the different substrates was done in the cleanroom (cleanroom class regarding *ISO-14644-1*: *ISO*-3/4). Before further active layers were applied to the ITO-glass substrates, the substrates must be subjected to the following standard cleaning procedure to remove dirt and dust particles from the surface:

1) Cleaning with soap solution with hands for at last 2 min
2) Washing substrates under warm demi water spray shower for 2 min
3) Cleaning the substrates in an ultrasonic bath for 5 min and put them between the single steps in warm demi water
    a. Acetone
    b. Isopropanol
4) Drying the substrates under a nitrogen stream
5) Drying the substrates in HORO-oven (*Horo Dr. Hofmann GmbH*) for 10 min at 140 °C

Afterward, the surface of the cleaned ITO-glass substrates was activated under a UV/ozone stream in a UVOH 150 oven (*FHR*) for 20 min.

Spin-coating of different layers

The preparation of the PEDOT:PSS layer was done directly after the substrate cleaning inside the cleanroom. An aqueous PEDOT:PSS layer (CLEVIOS PH 1000, *Heraeus*) was applied with a spin coater (*Süss MicroTec*) at 4000 rpm for 60 s. This solution is first filtered to remove dried and agglomerated particles (polyvinylidene fluoride (PVDF) filter with a pore size of 0.45 μm). To remove the residual water after spin-coating, the substrates are annealed at 140 °C for 10 min.

As an alternative hole-transport layer, pTFF (*National University of Singapore*) was prepared in a glove box (*mbraun*) of the preparation laboratory. Therefore, around 10 mg of the material were weight into a small vessel and suspended in 1 mL acetonitrile. To dissolve pTFF, it was heated up to 60 °C in an oil bath (without stirring plate/bar). For spin-coating, the solution was transferred to a glovebox in the fabrication laboratory and was applied with a spin coater (*Süss MicroTec*) at 2000 rpm for 30 s.

15 mg of B-oCz or B-oTC were dissolved in 1 mL anhydrous chloroform inside a glovebox of the preparation laboratory (*mbraun*) and filtered (polytetrafluorethylene(PTFE)-filter, pore size 0.22 μm). After transferring these solutions into a glovebox (*mbraun*), 130 μL were applied with a spin coater (*Süss MicroTec*) at 1500 rpm for 60 s and as an additional step for drying at 4000 rpm for 30 s on the hole-transport layer. For HOD and EOD layer thicknesses of 200 nm were necessary, so the concentration was doubled for the two small molecules B-oCz and B-oTC. All spin-coating parameters are summed up in Table 6.2.

Table 6.2: Parameters of spin-coating of different layers.

material	**solvent**	**concentration / mg/mL**	**rotation speed / rpm**	**rotation time / s**	**layer thickness / nm**
PEDOT:PSS	water	-	4000	60	55
pTFF	acetonitrile	10	2000	30	30
B-oCz	chloroform	15	1500	60	100
	chloroform	30	1500	60	200
B-oTC	chloroform	15	1500	60	100
	chloroform	30	1500	60	200

Thermally-evaporation under high-vacuum

To deposit metals (Mo_3O, Ba, Al), a high-vacuum evaporator (COAT 340, *Vactec*) was used. Different masks built the different structures of the substrates on the rotary substrate holder. The material was sublimated with the current-controlled resistance vaporizers, and the thickness of the sublimated layer is measured using a reference measurement with oscillating quartz. The evaporation rate is given in Å/s and is adjusted via the current output.

For depositing small organic compounds (B-oCz, B-oTC, TPBi (*Ossila*), TmPyTZ (*Mr. Dongcheng Chen*)), a high-vacuum evaporator (COAT 340-ORG, *Vactec*) was used. Different masks built different substrate structures on the rotary substrate holder. The material was sublimated with the temperature-controlled resistance vaporizers, and the thickness of the sublimated layer is measured using a reference measurement with oscillating quartz. The evaporation rate is given in Å/s and is adjusted via the temperature output.

Characterization of the devices

After the device fabrication, they were transferred into a glovebox (*mbraun*) of the measurement laboratory. After scratching free the contacts of the anode, the devices were placed into a special sample holder (Figure 6.2).

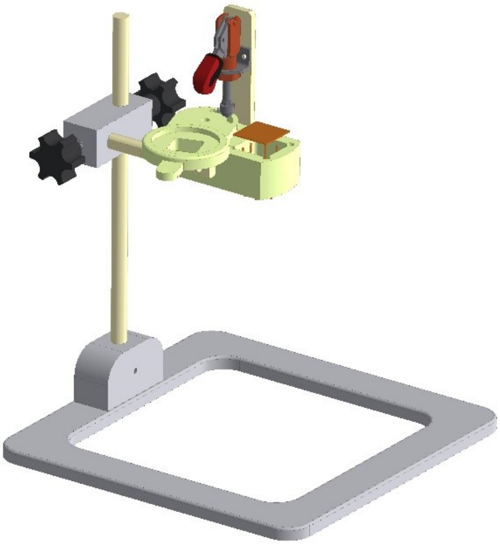

Figure 6.2: Device holder for photophysical characterizations inside the glovebox.

The (photo-)current density was measured with a Si-photodiode (S1336-8BQ, *Hamamatsu*) and detected outside the glovebox with a DIGITAL SOURCEMETER (*Keithley*) and. The results were processed with the LABVIEW 15.0 DEVELOP (*LabView*) program and plotted with ORIGIN PRO 9.0 (*Originlab*). The electroluminescence spectrum was measured with an ELECTROMETER AT 220 V (*Keithley*) in combination with OCEANVIEW (*Ocean Optics*) and processed with ORIGIN PRO 9.0 (*Originlab*), too. To calculate different physical parameters (luminance, luminous efficacy, EQE), a calculation script (written by *Mr. Dr. Yunghui Li*) for PYTHON 3.8 (*Python*) was used.

6.3 Experimental section

6.3.1 General procedure for the coupling of phenyl linker and donor (GP 1)

According to a literature procedure[3], 1.00 eq. of 2-bromo-3-fluorotoluene was suspended under argon atmosphere in anhydrous DMF together with 1.00 eq. of the carbazole derivative and 2.00 eq. of Cs_2CO_3. The suspension was stirred at 150 °C overnight. Afterward, the reaction mixture was poured into deionized water, and the organic layer was separated. The aqueous layer was extracted three times with dichloromethane. The combined organic phases were evaporated entirely to afford the crude product, which was purified by column chromatography on silica gel with a solvent mixture of *n*-hexanes/ethyl acetate (20:1, v:v).

6.3.2 General procedure for the synthesis of TADF small molecules (GP 2)

According to a literature procedure[3], 1.00 eq. of a compound, following GP 1, was diluted under argon atmosphere in anhydrous cyclopentyl methyl ether. To this solution, 1.00 eq *n*-butyl lithium in hexanes (2.5 M) was added dropwise at 0 °C. After stirring this solution at the same temperature for an additional 30 min, 1.00 eq. fluorodimesitylborane (Mes_2BF) dissolved in anhydrous cyclopentyl methyl ether (CPME) was added. The reaction mixture was stirred overnight at room temperature and was poured into a saturated aqueous NH_4Cl solution, subsequently. After separating the organic layer, the aqueous layer was extracted three times with dichloromethane. The collected organic phase was washed with brine, dried over anhydrous magnesium sulfate, and evaporated to dryness. The afforded crude product was purified by washing the solid with 250 mL *n*-hexanes to obtain the TADF small molecules.

6.3.3 General procedure for the halogenation of the small molecules (GP 3)

According to a literature procedure[51], 1.00 eq. of the corresponding small molecule and 1.00 eq. or 2.00 eq. of the halogenation reagent were diluted under argon atmosphere in an adequate amount of anhydrous chloroform and heated up to boiling temperature over different times. Afterward, the reaction mixture was extracted with deionized water and dried over anhydrous magnesium sulfate. The organic phase was isolated by filtration over neutral Al_2O_3, evaporated to dryness, and purified by a preparative gel permeation chromatography.

6.3.4 General procedure for the Suzuki cross-coupling reaction (GP 4)

1.00 eq. of a mono-halogenated small molecule was added under argon atmosphere to 1.00 eq. of 4,4,5,5-tetramethyl-2-(4-vinylphenyl)-1,3,2-dioxaborolane (4-BPinSt) dissolved in a solvent mixture of degassed water and degassed toluene (1:1, v:v). To this solution, 4.00 eq. of Na_2CO_3 and catalytical amounts of $Pd(PPh_3)_4$ were added. The reaction mixture was stirred for 2 d at 120 °C and quenched by adding methanol, subsequently. The reaction mixture was extracted with deionized water, dried over anhydrous magnesium sulfate, and filtered over neutral Al_2O_3. A preparative gel permeation chromatography purified the afforded organic phase.

6.3.5 General procedure for the Yamamoto cross-coupling reaction (GP 5)

According to a literature procedure[49], the Yamamoto catalytic system of $Ni(COD)_2$ / COD / and 2,2'-bipyridyl (each 2.5 eq.) was prepared inside a nitrogen-filled glove box in a 15 mL bottle with a septum and dissolved in anhydrous DMF. A Schlenk tube was charged with 1.00 eq. monomer dissolved in anhydrous toluene. The catalyst solution was heated at 50 °C for 30 min before it was transferred to the monomer solution. The reaction mixture was stirred for 2 d at 90 °C (oil bath temperature). Then, the reaction mixture was diluted with chloroform and later precipitated in a mixture of aqueous HCl, acetone, and methanol (1:1:1, v:v:v). The suspension was stirred for 2 h, and then the polymer was collected by filtration and dried under high vacuum for 4 h. Finally, the polymer was successively extracted with methanol and acetone, each for 3 d in a Soxhlet apparatus. The residue was dissolved in THF, and after evaporation of the solvent, the yellowish-green polymer could be afforded.

6.4 Synthesis of molecules

6.4.1 Synthesis of 9-(2-bromo-3-methylphenyl)-9*H*-carbazole

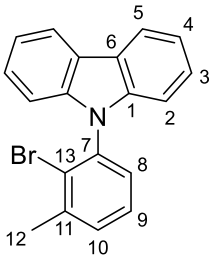

The synthesis of 9-(2-bromo-3-methylphenyl)-9*H*-carbazole (Br-oCz) is accorded to GP 1. In the following Table, the weights of starting materials, reagents, and solvent are shown.

material	M / g mol^{-1}	equivalents	n / mmol	m / mg	V / mL	*yield* / %
2-bromo-3-fluorotoluene	189.03	1.0	11.99	-	1.58	-
9*H*-carbazole	167.21	1.0	11.99	2000.0	-	-
Cs_2CO_3	325.82	2.0	24.18	7878.4	-	-
anhyd. DMF	-	solvent	-	-	20.0	
Br-oCz	336.23	-	9.21	3095.5	-	**76.7**

R_f (ethyl acetate/hexanes = 1:10):	0.81
^{1}H-NMR (298 K, 700 MHz, CD_2Cl_2):	δ = 2.58 (s, 12-H_3), 7.05 (d, J = 8.1 Hz, 2-H_2), 7.29 – 7.31 (m, 4-H_2), 7.22 (dd, J = 7.4 Hz, 9-H_1), 7.39 – 7.42 (m, 3-H_2), 7.45 – 7.49 (m, 8/10-H_2), 8.17 (d, J = 7.8 Hz, 5-H_2) ppm.
^{13}C-NMR (298 K, 176 MHz, CD_2Cl_2):	δ = 24.12 (12-C), 110.53 (2-C), 120.39 (4-C), 120.80 (5-C), 123.59 (6-C), 126.46 (3-C), 126.83 (13-C), 128.77 (10-C), 128.93 (9-C), 131.7 (8-C), 137.25 (11-C), 141.46 (7-C), 141.48 (1-C) ppm.

6.4.2 Synthesis of 9-(2-bromo-3-methylphenyl)-3,6-di-*tert*-butyl-9*H*-carbazole

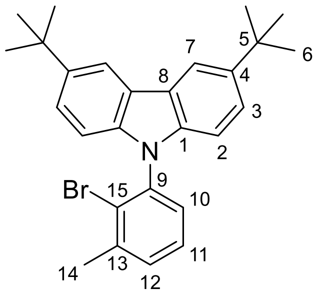

The synthesis of 9-(2-bromo-3-methylphenyl)-3,6-di-*tert*-butyl-9*H*-carbazole (Br-oTC) is accorded to GP 1. In the following Table the weights of starting materials, reagents and solvent are shown.

material	***M*** **/ g mol^{-1}**	**equivalents**	***n*** **/ mmol**	***m*** **/ mg**	***V*** **/ mL**	***yield*** **/ %**
2-bromo-3-fluorotoluene	189.03	1.0	7.13	-	0.94	-
3,6-di-*tert*-butyl-9*H*-carbazole	279.43	1.0	7.16	2000.1	-	-
Cs_2CO_3	325.82	2.0	14.22	4634.3	-	-
anhyd. DMF	-	solvent	-	-	20.0	
Br-oTC	448.45	-	4.14	1856.7	-	**57.7**

***R*$_f$** (ethyl acetate/hexanes = 1:10):	0.79
^{1}H-NMR (298 K, 700 MHz, CD_2Cl_2):	δ = 1.47 (s, 6-H_{18}), 2.57 (s, 14-H_3),6.96 (dd, J = 8.6 Hz, 2-H_2), 7.28 (m, 11-H_1), 7.41-7.46 (m, 3/10/12-H_4), 8.18 (dd, J = 1.8 Hz, 7-H_2) ppm.
^{13}C-NMR (298 K, 176 MHz, CD_2Cl_2):	δ =24.15 (14-C), 32.35 (6-C), 35.21 (5-C), 109.93 (2-C), 116.9 (7-C), 123.55 (1-C), 124.16 (3-C), 126.78 (13-C), 128.69 (12-C), 128.86 (11-C), 131.42 (10-C), 137.74 (9-C), 139.96 (8-C), 141.31 (15-C), 143.3 (4-C) ppm.

6.4.3 Synthesis of 9-(2-(dimesitylboraneyl)-3-methylphenyl)-9*H*-carbazole

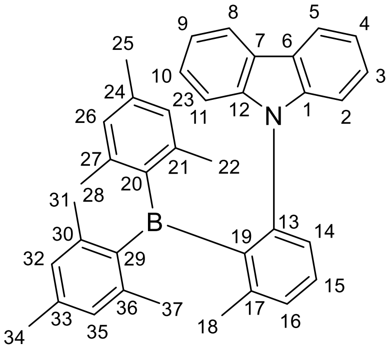

The synthesis of 9-(2-(dimesitylboraneyl)-3-methylphenyl)-9*H*-carbazole (B-oCz) is accorded to GP 2. In the following Table the weights of starting materials, reagents and solvent are shown.

material	***M* / g mol^{-1}**	**equivalents**	***n* / mmol**	***m* / mg**	***V* / mL**	***yield* / %**
Br-oCz	336.23	1.0	5.01	1684.5	-	-
n-BuLi (1.5 M in hexanes)	64.06	1.2	6.00	-	2.4	-
Mes_2BF	284.23	1.0	5.00	1350.8	-	-
anhyd. CPME	-	solvent	-	-	20.0	
B-oCz	505.51	-	3.66	1851.4	-	**73.2**

R_f (ethyl acetate/hexanes = 1:2): 0.85

^{1}H-NMR (298 K, 700 MHz, CD_2Cl_2): δ =0.69 (s, 22-H_3), 1.79 (s, 37-H_3), 1.86 (s, 25-H_3), 2.04 (s, 28-H_3), 2.19 (s, 18-H_3), 2.22 (s, 34-H_3), 2.37 (s, 31-H_3), 5.78 (s, 23-H_1), 6.07 (s, 26-H_1), 6.65 (d, J = 7.6 Hz, 10-H_1), 6.68 (s, 35-H_1), 6.77 (s, 32-H_1), 6.96-7.00 (m, 9/11-H_2), 7.10 (d, J = 7.6 Hz, 14-H_1), 7.15-7.17 (m, 2/4-H_2), 7.27 (pt, 3-H_1), 7.37 (d, J = 7.7 Hz, 16-H_1), 7.51 (pt, 15-H_1), 7.70 (d, J = 7 Hz, 8-H_1), 7.93 (d, J = 7.8 Hz, 5-H_1) ppm.

^{13}C-NMR (298 K, 176 MHz, CD_2Cl_2): δ = 21.15 (25-C), 21.17 (22-C), 21.41 (34-C), 23.31 (28-C), 23.44 (37-C), 24.08 (18-C), 25.37 (31-C), 111.23 (4-C), 111.53 (10-C), 118.92 (11-C), 119.14 (8-C), 119.41 (2-C), 120.22 (5-C), 122.87 (7-C), 124.24 (6-C), 125.12 (3-C), 125.14 (9-C), 128.01 (23-C), 128.08 (26-C), 129.10 (32-C), 129.43 (14-C), 130.15 (35-C), 131.70 (16-C), 131.90 (15-C), 137.59 (27-C), 137.75 (20-C), 138.56 (21-C), 140.86 (24/33-C), 142.18 (13-C), 142.36 (29-C), 143.03 (30/36-C), 143.62 (12-C), 143.78 (1-C), 144.54 (17-C), 147.85 (19-C) ppm.

6.4.4 Synthesis of 3,6-di-*tert*-butyl-9-(2-(dimesitylboraneyl)-3-methylphenyl)-9*H*-carbazole

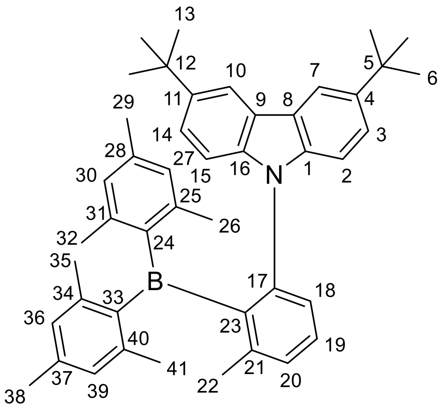

The synthesis of 3,6-di-*tert*-butyl-9-(2-(dimesitylboraneyl)-3-methylphenyl)-9*H*-carbazole (B-oTC) is accorded to GP 2. In the following Table the weights of starting materials, reagents and solvent are shown.

material	***M* / g mol^{-1}**	**equivalents**	***n* / mmol**	***m* / mg**	***V* / mL**	***yield* / %**
Br-oTC	448.45	1.0	3.86	1731.1	-	-
n-BuLi (1.5 M in hexanes)	64.06	1.2	4.75	-	1.9	-
Mes_2BF	284.23	1.0	3.84	1031.0	-	-
anhyd. CPME	-	solvent	-	-	20.0	
B-oTC	617.73	-	1.89	566.8	-	**49.2**

R_f (ethyl acetate/hexanes = 1:2):	0.85
^{1}H-NMR (298 K, 700 MHz, CD$_2$Cl$_2$):	δ =0.72 (s, 26-H$_3$), 1,39 (s, 6-H$_9$), 1.42 (s, 13-H$_9$), 1.75 (s, 41-H$_3$), 1.88 (s, 29-H$_3$), 2.04 (s, 32-H$_3$), 2.18 (s, 22-H$_3$), 2.22 (s, 38-H$_3$), 2.37 (s, 35-H$_3$), 5.82 (s, 27-H$_1$), 6.06 (s, 30-H$_1$), 6.57 (d, J = 8.6 Hz, 2-H$_1$), 6.67 (s, 39-H$_1$), 6.78 (s, 36-H$_1$) 7.05 (d, J = 7.7 Hz, 18-H$_1$), 7.06-7.07 (m, 3/15-H$_2$), 7.31 (dd, J = 8.5 Hz, 14-H$_2$), 7.35 (d, J = 7.7 Hz, 20-H$_1$), 7.48 (pt, 19-H$_1$), 7.71 (s, 7-H$_1$), 7.93 (s, 10-H$_1$) ppm.
^{13}C-NMR (298 K, 176 MHz, CD$_2$Cl$_2$):	δ = 21.34 (26-C), 21.41 (29-C), 21.54 (38-C), 23.39 (32/41-C), 24.06 (22-C), 25.38 (35-C), 32.40 (6-C), 32.44 (13-C), 34.93 (5-C), 35.06 (12-C), 110.51 (15-C), 111.04 (2-C), 114.94 (7-C), 119.24 (10-C), 122.67 (14-C), 122.80 (3-C), 124.22 (8/9-C), 127.51 (30-C), 127.83 (27-C), 129.05 (36-C), 129.34 (18-C), 130.13 (39-C), 131.46 (20-C), 131.85 (19-C), 137.37 (28-C), 138.42 (25-C), 138.75 (31-C), 140.68 (37-C), 141.70 (4-C), 142.32 (11-C), 142.46 (16/17-C), 142.87 (34/40-C), 143.23 (33-C), 143.72 (24-C), 144.46 (21-C), 147.84 (23-C) ppm.

6.4.5 Monohalogenation of 9-(2-(dimesitylboraneyl)-3-methylphenyl)-9*H*-carbazole

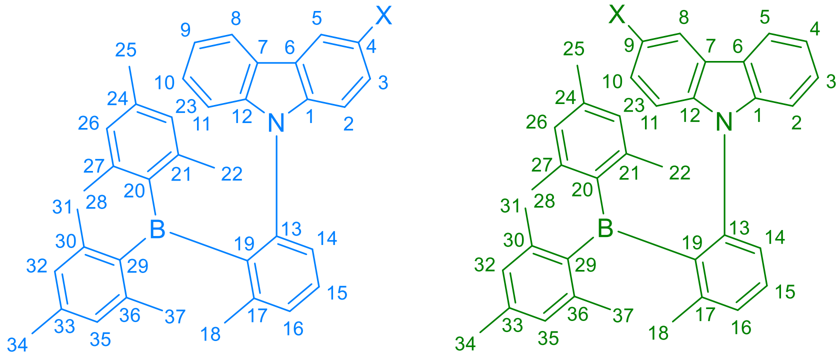

The monohalogenation of 9-(2-(dimesitylboraneyl)-3-methylphenyl)-9*H*-carbazole (B-oCz) is accorded to GP 3. In the following Table the weights of starting materials, reagents and solvent are shown.

material	*M* / g mol^{-1}	equivalents	*n* / μmol	*m* / mg	*V* / mL	*yield* / %
B-oCz	505.51	**a)** 1.0	99.3	50.2	-	-
		b) 1.0	395.5	200.0	-	-
		c) 1.0	198.4	100.3	-	-
N-bromo-succinimide	177.99	**a)** 1.0	99.4	17.7	-	-
		b) 1.0	400.6	71.3	-	-
N-iodo-succinimide	224.99	**c)** 1.0	198.2	44.6	-	-
$AuCl_3$	303.32	**b)** 0.03	11.2	3.4	-	-
anhyd. $CHCl_3$	-	solvent	-	-	**a)** 5.0	-
		solvent	-	-	**b)** 15.0	-
					c) 10.0	
anhyd. DMF	-	solvent	-	-	**c)** 2.0	-
(B-oCz)-4-Br +	584.41	-	**a)** 69.3	40.5	-	**69.8**
(B-oCz)-9-Br		-	**b)** 51.0	29.8	-	**12.9**
(B-oCz)-4-I +	631.41	-	-	**c)** -	-	**-**
(B-oCz)-9-I						

***R*$_f$** (ethyl acetate/hexanes = 1:2): 0.85

^{1}H-NMR[**]
(297 K, 300 MHz, CD$_2$Cl$_2$):
(assignment for monobromination)

δ =0.67 (s, 22-H$_3$), 0.76 (s, 22-H$_{1.6}$), 1.81 (s, 37/37-H$_{5.5}$), 1.86 (s, 25-H$_{2.3}$), 1.99 (s, 25-H$_3$), 2.03 (s, 28/28-H$_5$), 2.19 (s, 18/18-H$_5$), 2.22 (s, 34/34-H$_6$), 2.35 (s, 31/31-H$_5$), 5.85 (s, 23/23-H$_{1.6}$), 6.06 (s, 30-H$_{0.6}$), 6.14 (s, 30-H$_1$), 6.55 (d, *J* = 8.5, 10-H$_1$), 6.69 (s, 35/10/35-H$_{2.4}$), 6.78 (s, 32/32-H$_2$), 6.98-7.12 (m, 11/14/9/11/14-H$_5$), 7.19 (pt, 3/3-H$_3$[*]), 7.32 (pt, -H$_3$), 7.36-7.40 (m, -H$_3$), 7.52 (pt, 15/15-H$_2$), 7.67 (d, *J* = 6.7 Hz, -H$_{0.6}$), 7.84 (s, -H$_1$), 7.90 (d, *J* = 7.5 Hz, 5-H$_1$), 8.07 (s, 5-H$_{0.6}$) ppm.

^{13}C-NMR[***]
(297 K, 75 MHz, CD$_2$Cl$_2$):
(assignment for monobromination)

δ = 21.15 (-C), 21.23 (-C), 21.44 (-C), 23.27 (-C), 23.32 (-C), 23.48 (-C), 24.09 (-C), 25.35 (-C), 111.51 (-C), 111.81 (-C), 112.09 (-C), 112.76 (-C), 113.10 (-C), 118.74 (-C), 119.42 (-C), 119.95 (-C), 120.52 (-C), 121.84 (-C), 122.96 (-C), 123.12 (-C), 124.55 (-C), 126.01 (-C), 127.70 (-C), 127.74 (-C), 128.02 (-C), 128.07 (-C), 128.13 (-C), 128.18 (-C), 128.23 (-C), 129.16 (-C), 129.29 (-C), 130.22 (-C), 131.98 (-C), 137.74 (-C), 137.98 (-C), 138.60 (-C), 141.03 (-C), 141.43 (-C), 142.17 (-C), 142.27 (-C), 142.35 (-C), 143.08 (-C), 143.11 (-C), 143.97 (-C), 144.71 (-C) ppm.

APCI-MS spectrum

predicted: m/z((B-oCz)-Br) = 584.41
found: m/z = 583.95

[**] CHCl$_3$ under the signal.
[**] not all assignments were possible.
[***] assignments without 2D-NMR spectra not possible.

6.4.6 Monohalogenation of 3,6-di-*tert*-butyl-9-(2-(dimesitylboraneyl)-3-methylphenyl)-9*H*-carbazole

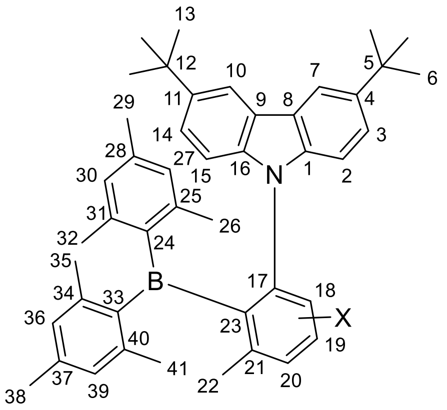

The monohalogenation of 3,6-di-*tert*-butyl-9-(2-(dimesitylboraneyl)-3-methylphenyl)-9*H*-carbazole (B-oTC) is accorded to GP 3. In the following Table the weights of starting materials, reagents and solvent are shown.

material	***M*** **/ g mol^{-1}**	**equivalents**	***n*** **/ µmol**	***m*** **/ mg**	***V*** **/ mL**	***yield*** **/ %**
B-oTC	617.73	**a)** 1.0	80.9	50.0	-	-
		b) 1.0	809.6	500.1	-	-
		c) 1.0	162.4	100.3	-	-
N-bromo-succinimide	177.99	**a)** 1.0	81.5	14.5	-	-
		b) 1.0	839.9	149.5	-	-
N-iodo-succinimide	224.99	**c)** 1.0	163.1	36.7	-	-
$AuCl_3$	303.32	**b)** 0.09	13.9	4.0	-	-
anhyd. $CHCl_3$	-	solvent	-	-	**a)** 5.0	-
		solvent	-	-	**b)** 20.0	-
					c) 10.0	
anhyd. DMF	-	solvent	-	-	**c)** 2.0	-
(B-oTC)-x-Br	696.62	-	**a)** 57.9	40.34	-	**71.6**
		-	**b)** 37.2	25.91	-	**4.6**
(B-oTC)-x-I	743.62	-	**-**	**c)** -	-	**-**

***R*$_f$** (ethyl acetate/hexanes = 1:2): -

^{1}H-NMR and **^{13}C-NMR** (297 K, 300/75 MHz, CD_2Cl_2): assignment not possible (spectra for X = Br in the appendix, Figure **9.26** and Figure **9.27**)

APCI-MS spectrum: predicted: m/z((B-oTC)-Br) = 696.62

found: m/z = 697.05

6.4.7 Dihalogenation of 9-(2-(dimesitylboraneyl)-3-methylphenyl)-9*H*-carbazole

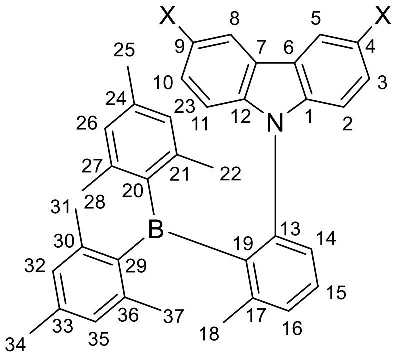

The dibromination of 9-(2-(dimesitylboraneyl)-3-methylphenyl)-9*H*-carbazole (B-oCz) is accorded to GP 3. In the following Table the weights of starting materials, reagents and solvent are shown.

material	***M* / g mol^{-1}**	**equivalents**	***n* / µmol**	***m* / mg**	***V* / mL**	***yield* / %**
B-oCz	505.51	**a)** 1.0	99.1	50.06	-	-
		b) 1.0	593.5	300.0	-	-
		c) 1.0	198.4	100.3	-	-
N-bromo-succinimide	177.99	**a)** 2.0	197.8	35.2	-	-
		b) 2.0	1197.3	213.1	-	-
N-iodo-succinimide	224.99	**c)** 2.0	397.4	89.4	-	-
$AuCl_3$	303.32	**b)** 0.01	4.6	1.4		
anhyd. $CHCl_3$	-	solvent	-	-	**a)** 7.5	-
		solvent	-	-	**b)** 20.0	-
		solvent	-	-	**c)** 12.0	-
anhyd. DMF	-	solvent	-	-	**c)** 2.0	-
(B-oCz)-4,9-Br_2	663.30	-	**a)** 76.7	50.9	-	**77.4**
		-	**b)** 486.4	322.6	-	**82.0**
(B-oCz)-4,9-I_2	757.30	-	**c)** -	-	-	**-**

R_f (ethyl acetate/hexanes = 1:2):	0.85
^{1}H-NMR (298 K, 700 MHz, CD_2Cl_2): (assignment for dibromination)	δ =0.72 (s, 22-H_3), 1.79 (s, 37-H_3), 1.98 (s, 25-H_3), 2.00 (s, 28-H_3), 2.18 (s, 18-H_3), 2.22 (s, 34-H_3), 2.30 (s, 31-H_3), 5.87 (s, 23-H_1), 6.12 (s, 26-H_1), 6.55 (d, J = 8.7 Hz, 10-H_1), 6.69 (s, 35-H_1), 6.77 (s, 32-H_1), 7.05-7.14 (m, 2/11/14-H_3), 7.38-7.41 (m, 3/16-H_2), 7.52 (pt, 15-H_1), 7.78 (s, 8-H_1), 8.02 (s, 5-H_1) ppm.
^{13}C-NMR*** (298 K, 176 MHz, CD_2Cl_2): (assignment for dibromination)	δ = 21.19 (25-C), 21.39 (22-C), 21.42 (34-C), 23.24 (28-C), 23.46 (37-C), 24.07 (18-C), 25.29 (31-C), 112.27 (4-C), 112.58 (10-C), 113.05 (11-C), 113.38 (8-C), 122.06 (2-C), 123.22 (5-C), 123.39 (7-C), 124.85 (6-C), 128.16 (-C), 128.32 (-C), 128.63 (14-C), 129.12 (-C), 129.20 (-C), 130.27 (-C), 132.04 (16-C), 132.25 (15-C), 137.72 (-C), 138.14 (-C), 138.66 (-C), 140.81 (-C), 141.18 (-C), 142.15 (-C), 142.51 (-C), 142.60 (-C), 143.15 (-C), 144.85 (-C) ppm.
APCI-MS spectrum	predicted: m/z ((B-oCz)-4,9-Br_2) = 663.30 found: m/z = 663.80

***assignments without 2D-NMR spectra not possible.

6.4.8 SUZUKI cross-coupling reaction of monobrominated 9-(2-(dimesitylboraneyl)-3-methylphenyl)-9*H*-carbazole

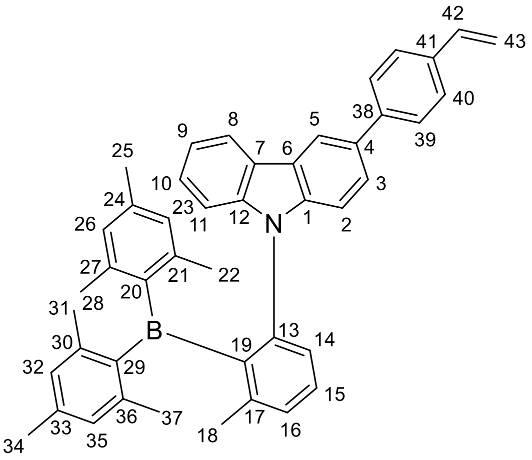

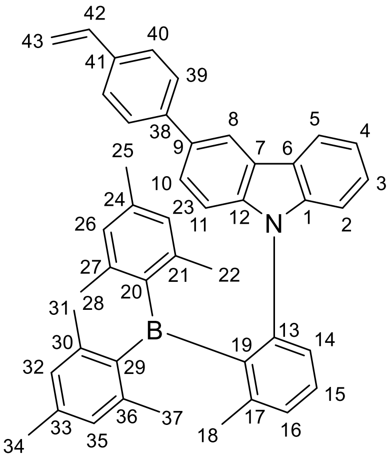

The SUZUKI cross-coupling reaction of the mono-brominated 9-(2-(dimesitylboraneyl)-3-methylphenyl)-9*H*-carbazole ((B-oCz)-Br) with 4-BPinSt is accorded to GP 4. In the following Table, the weights of starting materials, reagents, and solvent are shown.

material	*M* / g mol^{-1}	equivalents	*n* / μmol	*m* / mg	*V* / mL	*yield* / %
(B-oCz)-Br	617.73	1.0	32.7	20.2	-	-
4-BPinSt	230.11	1.1	34.8	8.0	-	-
Na_2CO_3	105.99	4.2	136.8	14.5	-	-
$Pd(PPh_3)_4$	1155.59	0.1	3.6	4.2	-	-
degassed H_2O	-	solvent	-	1.0		
degassed THF	-	solvent	-	1.0		-
(B-oCz)-4-St + (B-oCz)-9-St	607.65	-		~1.0 mg	-	**4.9**

R_f (ethyl acetate/hexanes = 1:2): -

^{1}H-NMR (297 K, 300 MHz, CD_2Cl_2): assignment not possible (spectra in the appendix Figure 9.32)

APCI-MS spectrum: predicted: m/z((B-oCz)-4-St) = 607.65
found: m/z = 607.95

6.4.9 YAMAMOTO condensation reaction of dibrominated 9-(2-(dimesitylboraneyl)-3-methylphenyl)-9*H*-carbazole

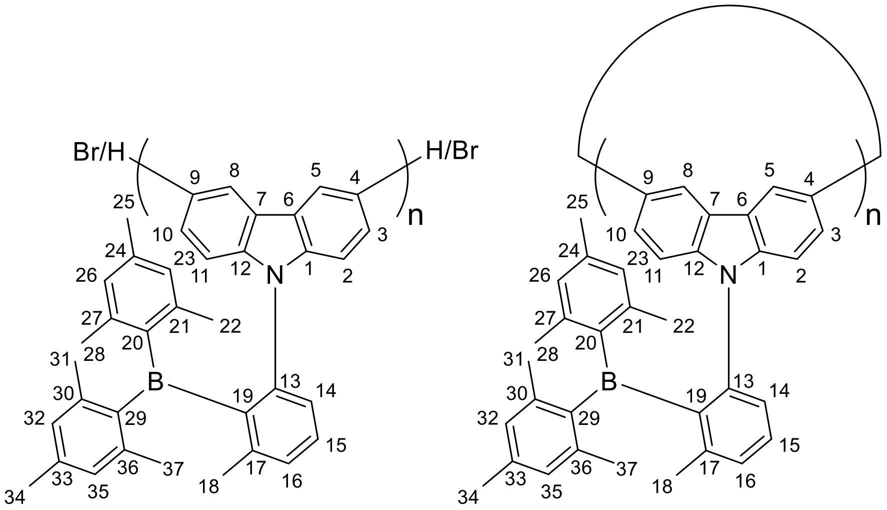

The YAMAMOTO condensation reaction of the dibrominated 9-(2-(dimesitylboraneyl)-3-methylphenyl)-9*H*-carbazole ((B-oCz)-4,9-Br$_2$) is accorded to GP 5. In the following Table, the weights of starting materials, reagents, and solvent are shown.

material	*M* / g mol^{-1}	equivalents	*n* / µmol	*m* / mg	*V* / µL	*yield* / %
(B-oCz)-4,9-Br$_2$	663.30	1.0	63.6	42.2	-	-
Ni(COD)$_2$	275.06	2.5	161.8	44.5	-	-
COD	108.18	2.4	151.6	-	18.6	-
BPY	156.18	2.7	172.9	27.0	-	-
degassed toluene	-	solvent	-	-	400.0	-
degassed DMF	-	solvent	-		400.0	-
Poly-(B-oCz)	M_n = 3179.77	-	7.3	23.1[a]	-	**11.5**
	M_n =4344.34	-	2.3	10.1[b]	-	**3.6**

[a] yield after filtration of the crude product through a syringe filter (polytetrafluorethylene(PTFE)-filter, pore size 0.22 µm).

[b] yield after the final Soxhlet extraction (extraction thimbles MN645 20x80 mm (*Macherey Nagel*)).

^{1}H-NMR**** (298 K, 700 MHz, CD_2Cl_2):	δ =0.88 (22), 1.29-2.49 (18, 25, 28, 31, 34 37), 5.8 (23), 6.18 (26), 6.65-6.76 (10, 35), 6.91 (11), 7.16-7.72 (2, 3, 14, 15, 16), 8.04-8.25 (5, 8 for n>4), 8.47 (5, 8 for n = 4) ppm.
^{13}C-NMR**** (298 K, 176 MHz, CD_2Cl_2):	δ =21.40 (-C), 21.55 (-C), 23.64 (-C), 23.79 (-C), 30.91 (-C), 35.27 (-C), 111.80 (-C), 112.15 (-C), 124.54 (-C), 125.32 (-C), 126.06 (-C), 128.69 (-C), 129.00 (-C), 129.69 (-C), 130.07 (-C), 130.76 (-C), 132.16 (-C), 132.58 (-C), 138.33 (-C), 138.96 (-C), 141.20 (-C), 141.24 (-C), 142.79 (-C), 143.18 (-C), 143.54 (-C), 143.98 (-C), 152.84 (5,8-C for n = 4) ppm.
GPC	M_n = 4344.34 g/mol M_w = 6704.76 g/mol $Đ$ = 1.54
MALDI-TOF MS	$[M^{+\cdot}]$ = 2013.27 m/z

****for better assignments more substance and 2D-NMR spectra are needed.

7 References

[1] H. Uoyama, K. Goushi, K. Shizu, H. Nomura, C. Adachi, *Nature* **2012**, *492*, 234–238.

[2] Y. Im, M. Kim, Y. J. Cho, J. A. Seo, K. S. Yook, J. Y. Lee, *Chem. Mater.* **2017**, *29*, 1946–1963.

[3] X. L. Chen, J. H. Jia, R. Yu, J. Z. Liao, M. X. Yang, C. Z. Lu, *Angew. Chemie - Int. Ed.* **2017**, *56*, 15006–15009.

[4] Y. Tao, R. Chen, H. Li, C. Zheng, W. Huang, in *Highly Effic. OLEDs - Mater. Based Therm. Act. Delayed Fluoresc.* (Ed.: H. Yersin), Wiley-VCH Verlag GmbH & Co. KGaA, Weinheim, **2018**, pp. 377–424.

[5] Q. Wei, Z. Ge, B. Voit, *Macromol. Rapid Commun.* **2019**, *40*, 1–19.

[6] Y. Xie, Z. Li, *J. Polym. Sci. Part A Polym. Chem.* **2017**, *55*, 575–584.

[7] S. Izumi, H. F. Higginbotham, A. Nyga, P. Stachelek, N. Tohnai, P. de Silva, P. Data, Y. Takeda, S. Minakata, *J. Am. Chem. Soc.* **2020**, DOI 10.1021/jacs.9b11578.

[8] S. Shao, J. Hu, X. Wang, L. Wang, X. Jing, F. Wang, *J. Am. Chem. Soc.* **2017**, *139*, 17739–17742.

[9] J. Hu, Q. Li, X. Wang, S. Shao, L. Wang, X. Jing, F. Wang, *Angew. Chemie* **2019**, *230026*, 8493–8497.

[10] H. Shirakawa, E. J. Louis, A. G. MacDiarmid, C. K. Chiang, A. J. Heeger, *J. Chem. Soc. Chem. Commun.* **1977**, 578–580.

[11] A. Tillemans, "Chemie-Nobelpreis 2000: Elektrisch leitende Kunststoffe könnten die Technik des 21. Jahrhunderts bestimmen," can be found under https://www.wissenschaft.de/umwelt-natur/chemie-nobelpreis-2000-elektrisch-leitende-kunststoffe-koennten-die-technik-des-21-jahrhunderts-bestimmen/, **2000**.

[12] C. W. Tang, S. A. Vanslyke, *Appl. Phys. Lett.* **1987**, *51*, 913–915.

[13] D. Z. Garbuzov, V. Bulović, P. E. Burrows, S. R. Forrest, *Chem. Phys. Lett.* **1996**, *249*, 433–437.

[14] B. Geffroy, P. le Roy, C. Prat, *Polym. Int.* **2006**, *55*, 572–582.

[15] J. H. Burroghes, D. D. C. Bradley, A. R. Brown, R. N. Marks, K. Mackay, R. H. Friend, P. L. Burns, A. B. Holmes, *Nature* **1990**, *347*, 539–541.

[16] C. D. Müller, A. Falcou, N. Reckefuss, M. Rojahn, V. Wiederhirn, P. Rudati, H. Frohne, O. Nuyken, H. Becker, K. Meerholz, *Nature* **2003**, *421*, 829–833.

[17] S. M. Lee, J. H. Kwon, S. Kwon, K. C. Choi, *IEEE Trans. Electron Devices* **2017**, *64*, 1922–1931.

[18] J.-H. Jou, S. Kumar, A. Agrawal, T.-H. Li, S. Sahoo, *J. Mater. Chem. C* **2015**, *3*, 2974–3002.

[19] R. Young, *Inf. Disp. (1975).* **2019**, *35*, 24–29.

[20] S. R. Forrest, *Nature* **2004**, *428*, 911–918.

[21] M. Schwoerer, H. C. Wolf, *Organic Molecular Solids*, Wiley-VCH-Verlag, **2005**.

[22] D. Hertel, C. D. Müller, K. Meerholz, *Chemie Unserer Zeit* **2005**, *39*, 336–347.

[23] J. C. Scott, G. G. Malliaras, *Chem. Phys. Lett.* **1999**, *299*, 115–119.

[24] B. N. Limketkai, M. A. Baldo, *Phys. Rev. B - Condens. Matter Mater. Phys.* **2005**, *71*, 1–9.

[25] P. Mark, W. Helfrich, *Space-Charge-Limited Currents in Organic Crystals*, **1962**.

[26] T. Tsujimura, *OLED Displays - Fundamentals and Applications*, Wiley, New Jersey (USA), **2017**.

[27] D. Poplavskyy, W. Su, F. So, *J. Appl. Phys.* **2005**, *98*, DOI 10.1063/1.1941482.

[28] J. Shinar, Ed. , *Organic Light-Emitting Devices: A Survey*, Springer-Verlag, New York, **2004**.

[29] H. Bässler, A. Köhler, in *Unimolecular Supramol. Electron. I - Chem. Phys. Meets Met. Interfaces* (Ed.: R.M. Metzger), Springer-Verlag Berlin Heidelberg, Berlin, Heidelberg, **2012**, pp. 1–66.

[30] H. Yersin, *Topics in Current Chemistry*, **2004**.

[31] F.-F. Hartmann, Neuartige Organische Funktionsmaterialien Zum Einsatz in Flüssigphasen-Prozessierten OLEDs, Technische Universität Darmstadt, **2019**.

[32] R. B. Sekar, A. Periasamy, *J. Cell Biol.* **2003**, *160*, 629–633.

[33] D. L. Dexter, *J. Chem. Phys.* **1953**, *21*, 836–850.

[34] H. Yersin, A. F. Rausch, R. Czerwieniec, T. Hofbeck, T. Fischer, *Coord. Chem. Rev.* **2011**, *255*, 2622–2652.

[35] T. Takahashi, S. Seo, H. Nowatari, S. Hosoumi, T. Ishisone, T. Watabe, S. Mitsumori, N. Ohsawa, S. Yamazaki, *J. Soc. Inf. Disp.* **2016**, *24*, 360–370.

[36] A. Monkman, *Highly Effic. OLEDs Mater. Based Therm. Act. Delayed Fluoresc.* **2018**, 425–463.

[37] P. W. M. Blom, M. J. M. De Jong, *Philips J. Res.* **1998**, *51*, 479–494.

[38] P. W. M. Blom, M. J. M. De Jong, J. J. M. Vleggaar, *Appl. Phys. Lett.* **1996**, *68*, 3308–33010.

[39] G. N. Lewis, D. Lipkin, T. T. Magel, *J. Am. Chem. Soc.* **1941**, *63*, 3005–18.

[40] E. Spuling, N. Sharma, I. D. W. Samuel, E. Zysman-Colman, S. Bräse, *Chem. Commun.* **2018**, *54*, 9278–9281.

[41] J. Lee, N. Aizawa, M. Numata, C. Adachi, T. Yasuda, *Adv. Mater.* **2017**, *29*, 1–6.

[42] Q. Zhang, D. Tsang, H. Kuwabara, Y. Hatae, B. Li, T. Takahashi, S. Y. Lee, T. Yasuda, C. Adachi, *Adv. Mater.* **2015**, *27*, 2096–2100.

[43] T. Huang, W. Jiang, L. Duan, *J. Mater. Chem. C* **2018**, *6*, 5577–5596.

[44] R. S. Nobuyasu, Z. Ren, G. C. Griffiths, A. S. Batsanov, P. Data, S. Yan, A. P. Monkman, M. R. Bryce, F. B. Dias, *Adv. Opt. Mater.* **2016**, *4*, 597–607.

[45] J. G. Jang, H. J. Ji, H. S. Kim, J. C. Jeong, *Curr. Appl. Phys.* **2011**, *11*, S251–S254.

[46] N. B. Kotadiya, H. Lu, A. Mondal, Y. Ie, D. Andrienko, P. W. M. Blom, G. J. A. H. Wetzelaer, *Nat. Mater.* **2018**, *17*, 329–334.

[47] A. G. Ricciardulli, B. Van Der Zee, K. Philipps, G. A. H. Wetzelaer, R. Q. Png, P. K. H. Ho, L. L. Chua, P. W. M. Blom, *APL Mater.* **2020**, *8*, 8–12.

[48] J. Ostrauskaite, P. Strohriegl, *Macromol. Chem. Phys.* **2003**, *204*, 1713–1718.

[49] Q. Wei, P. Kleine, Y. Karpov, X. Qiu, H. Komber, K. Sahre, A. Kiriy, R. Lygaitis, S. Lenk, S. Reineke, et al., *Adv. Funct. Mater.* **2017**, *27*, 1–11.

[50] G. R. Fulmer, A. J. M. Miller, N. H. Sherden, H. E. Gottlieb, A. Nudelman, B. M. Stoltz, J. E. Bercaw, K. I. Goldberg, *Organometallics* **2010**, *29*, 2176–2179.

[51] M. Majchrzak, M. Grzelak, B. Marciniec, *Org. Biomol. Chem.* **2016**, *14*, 9406–9415.

8 Erklärung zur Abschlussarbeit

Hiermit versichere ich, Felix Bernt, die vorliegende Master-Thesis ohne Hilfe Dritter und nur mit den angegebenen Quellen und Hilfsmitteln angefertigt zu haben. Alle Stellen, die Quellen entnommen wurden, sind als solche kenntlich gemacht worden. Diese Arbeit hat in gleicher oder ähnlicher Form noch keiner Prüfungsbehörde vorgelegen.

Mir ist bekannt, dass im Falle eines Plagiats (§38 Abs.2 APB) ein Täuschungsversuch vorliegt, der dazu führt, dass die Arbeit mit 5,0 bewertet und damit ein Prüfungsversuch verbraucht wird. Abschlussarbeiten dürfen nur einmal wiederholt werden.

Bei der abgegebenen Thesis stimmen die schriftliche und die zur Archivierung eingereichte elektronische Fassung überein.

English translation for information purposes only:

Thesis Statement pursuant to § 23 paragraph 7 of APB TU Darmstadt

I herewith formally declare that I, Felix Bernt, have written the submitted thesis independently. I did not use any outside support except for the quoted literature and other sources mentioned in the paper. I clearly marked and separately listed all of the literature and all of the other sources which I employed when producing this academic work, either literally or in content. This thesis has not been handed in or published before in the same or similar form.

I am aware, that in case of an attempt at deception based on plagiarism (§38 Abs. 2 APB), the thesis would be graded with 5,0 and counted as one failed examination attempt. The thesis may only be repeated once.

In the submitted thesis the written copies and the electronic version for archiving are identical in content.

Datum / Date: Unterschrift / Signature:

9 Appendix

9.1 NMR spectra

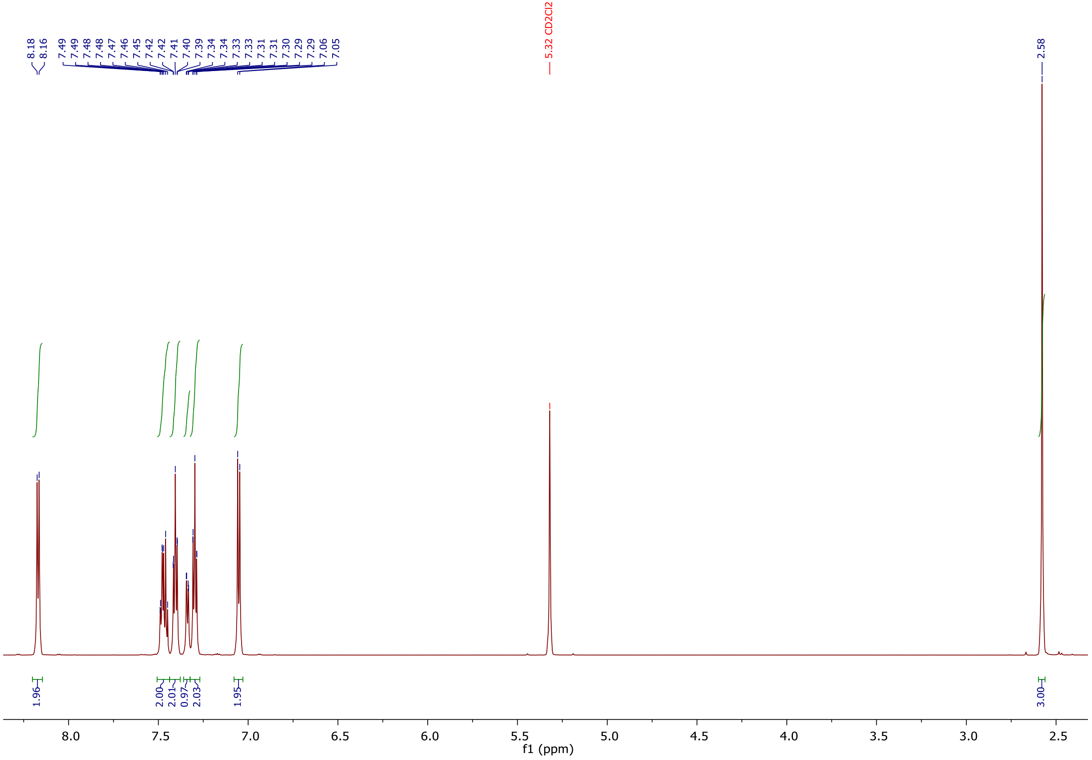

Figure 9.1: ^{1}H-NMR spectrum of 9-(2-bromo-3-methylphenyl)-9*H*-carbazole, 700 MHz, 298 K, CD_2Cl_2.

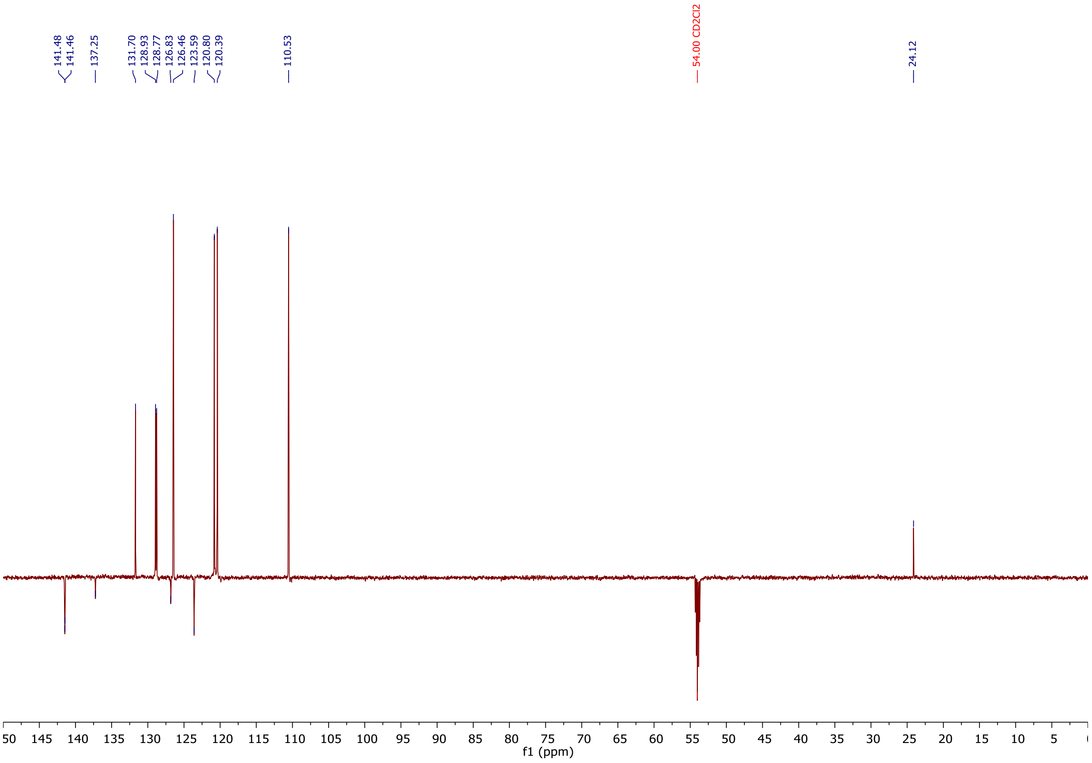

Figure 9.2: ^{13}C-NMR spectrum of 9-(2-bromo-3-methylphenyl)-9*H*-carbazole, 176 MHz, 298 K, CD_2Cl_2.

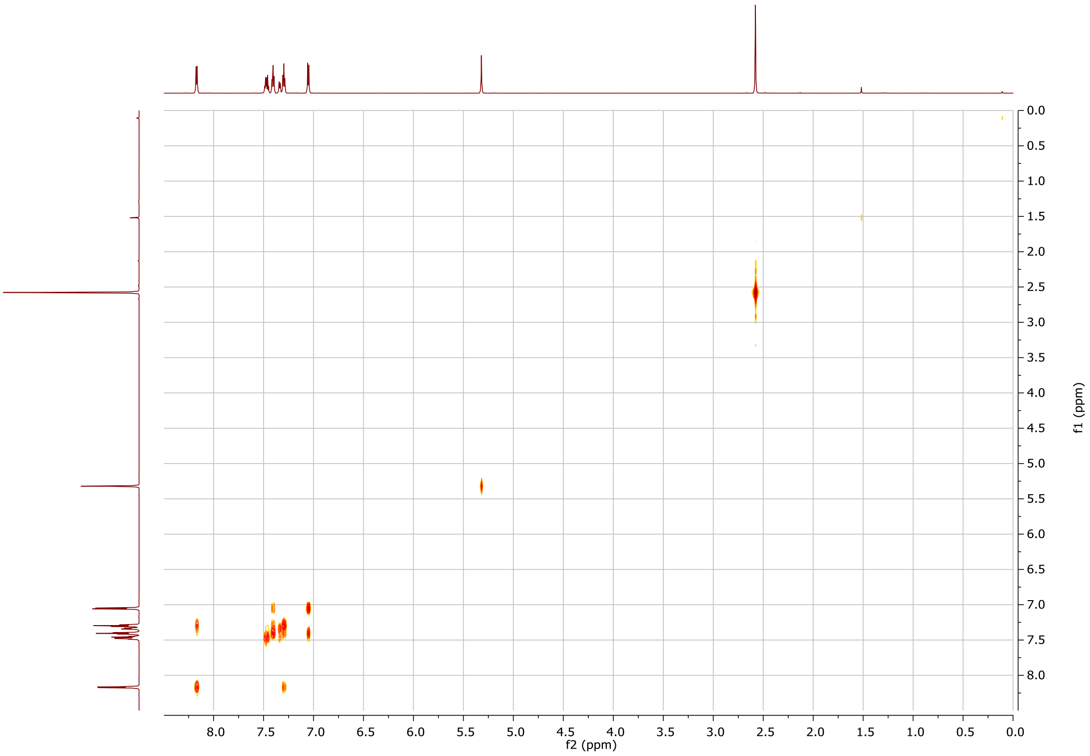

Figure 9.3: COSY NMR spectrum of 9-(2-bromo-3-methylphenyl)-9*H*-carbazole, (700 MHz, 700 MHz), 298 K, CD_2Cl_2.

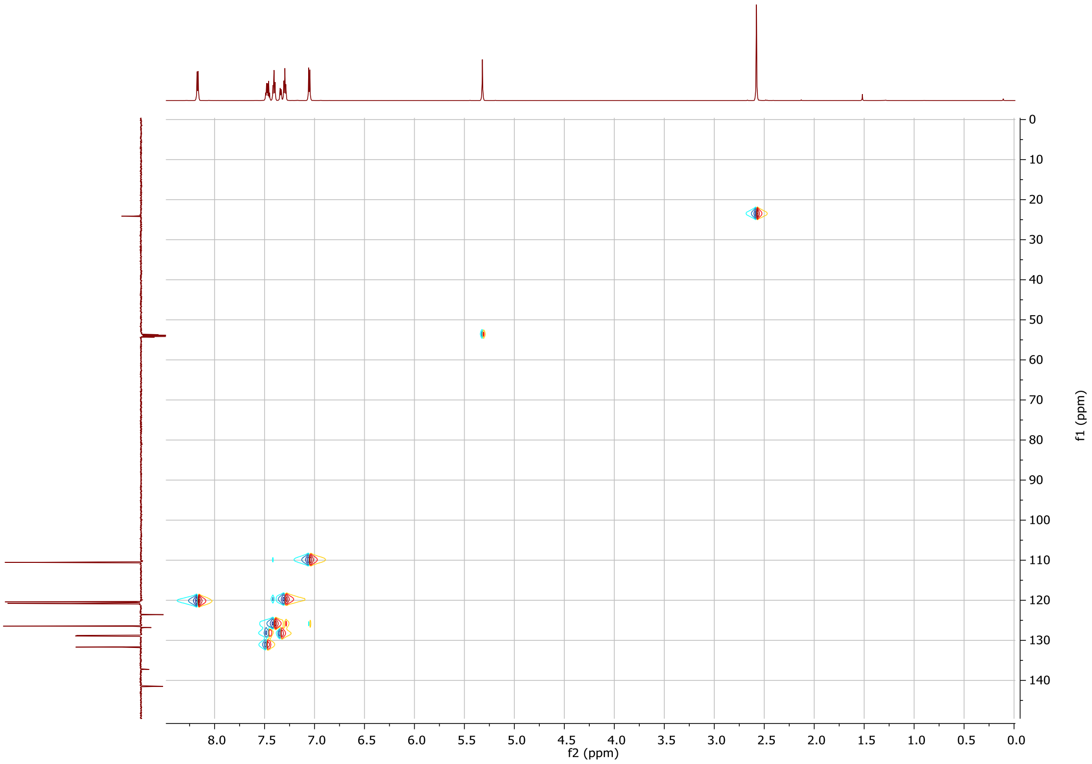

Figure 9.4: HSQC NMR spectrum of 9-(2-bromo-3-methylphenyl)-9*H*-carbazole, (700 MHz, 176 MHz), 298 K, CD_2Cl_2.

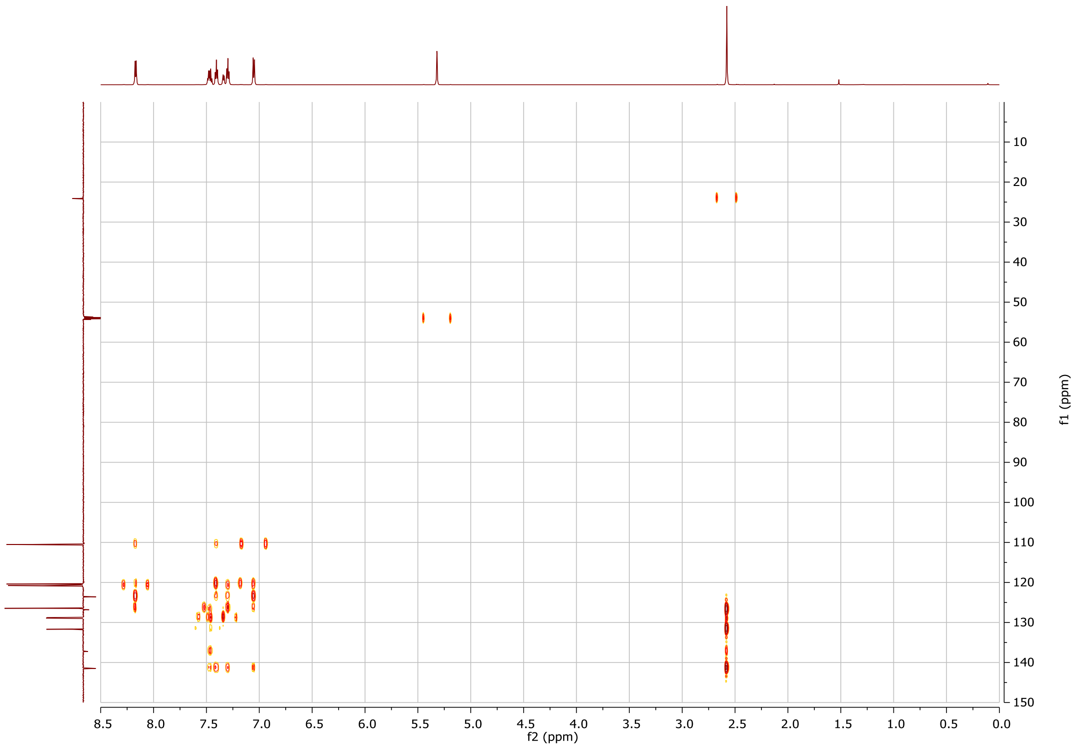

Figure 9.5: HMBC NMR spectrum of 9-(2-bromo-3-methylphenyl)-9*H*-carbazole, (700 MHz, 176 MHz), 298 K, CD_2Cl_2.

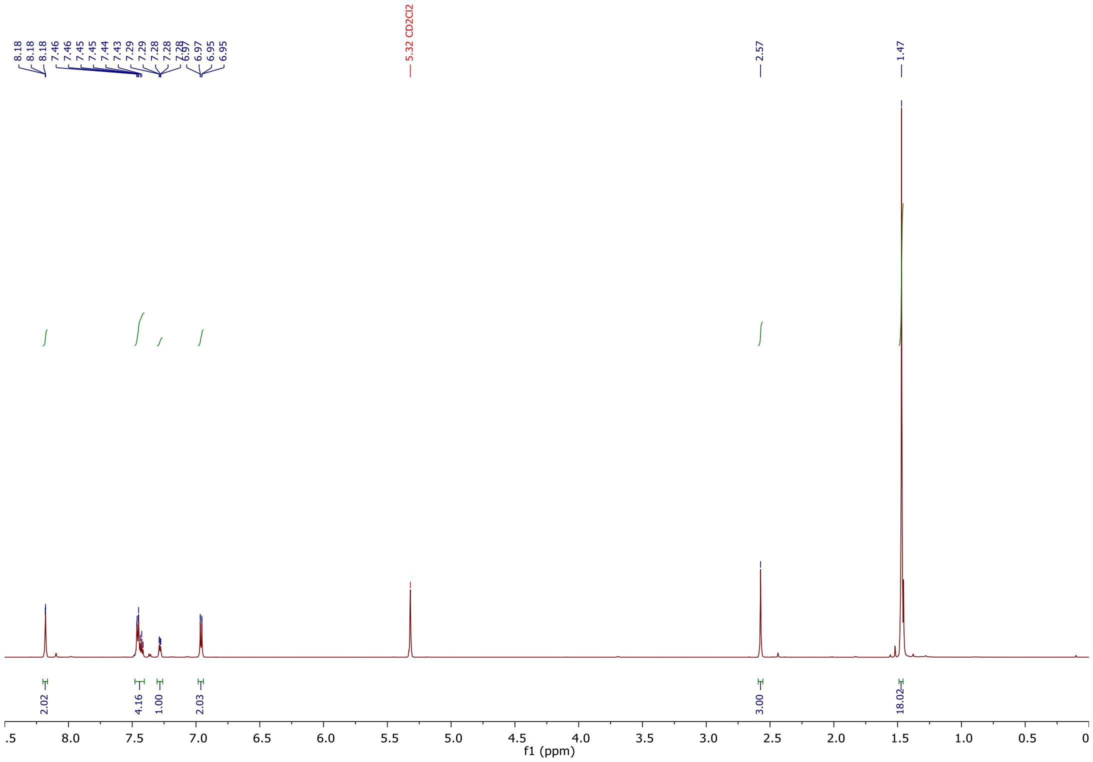

Figure 9.6: ^{1}H-NMR spectrum of 9-(2-bromo-3-methylphenyl)-3,6-di-*tert*-butyl-9*H*-carbazole, 700 MHz, 298 K, CD_2Cl_2.

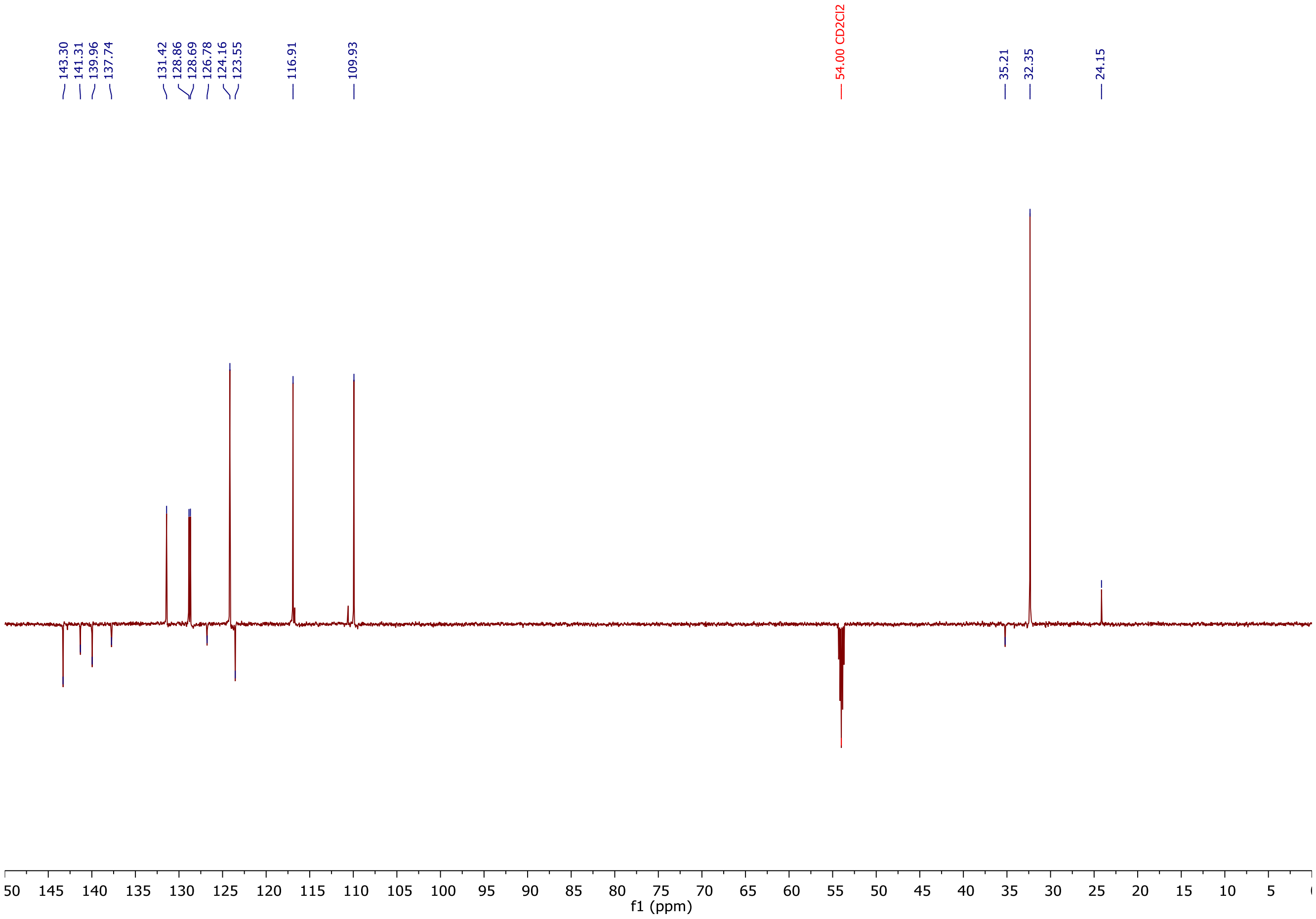

Figure 9.7: ^{13}C-NMR spectrum of 9-(2-bromo-3-methylphenyl)-3,6-di-*tert*-butyl-9*H*-carbazole, 176 MHz, 298 K, CD_2Cl_2.

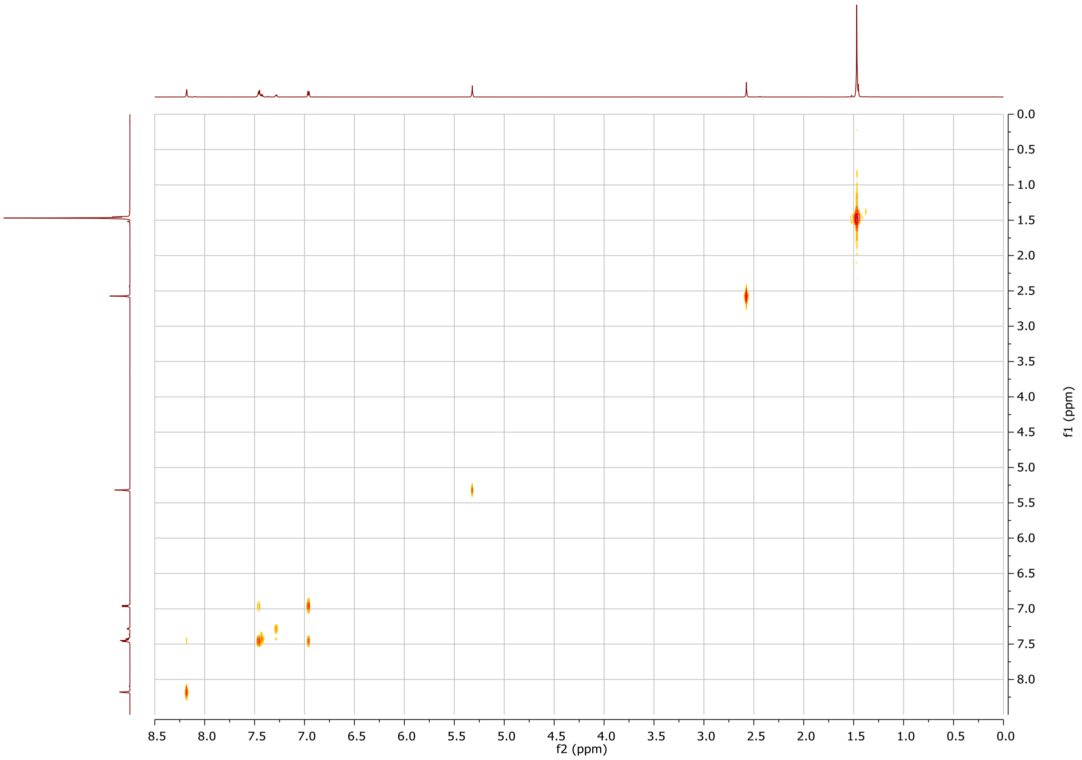

Figure 9.8: COSY-NMR spectrum of 9-(2-bromo-3-methylphenyl)-3,6-di-*tert*-butyl-9*H*-carbazole, (700 MHz, 700 MHz), 298 K, CD_2Cl_2.

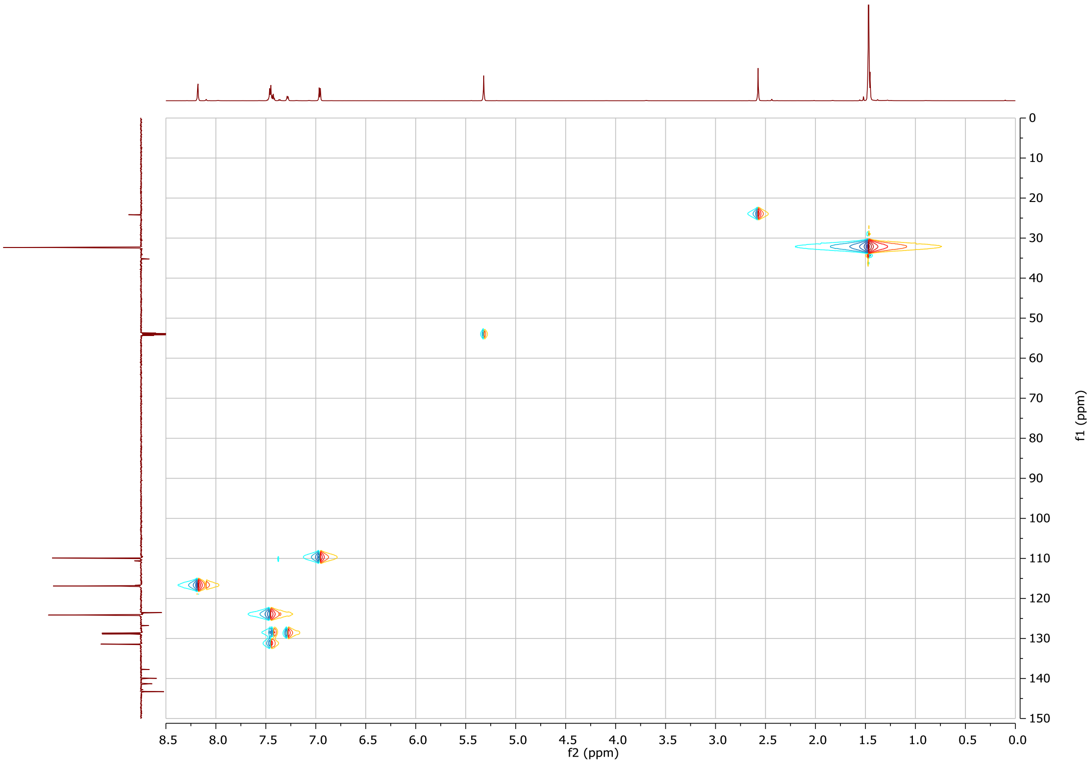

Figure 9.9: HSQC-NMR spectrum of 9-(2-bromo-3-methylphenyl)-3,6-di-*tert*-butyl-9*H*-carbazole, (700 MHz,176 MHz), 298 K, CD_2Cl_2.

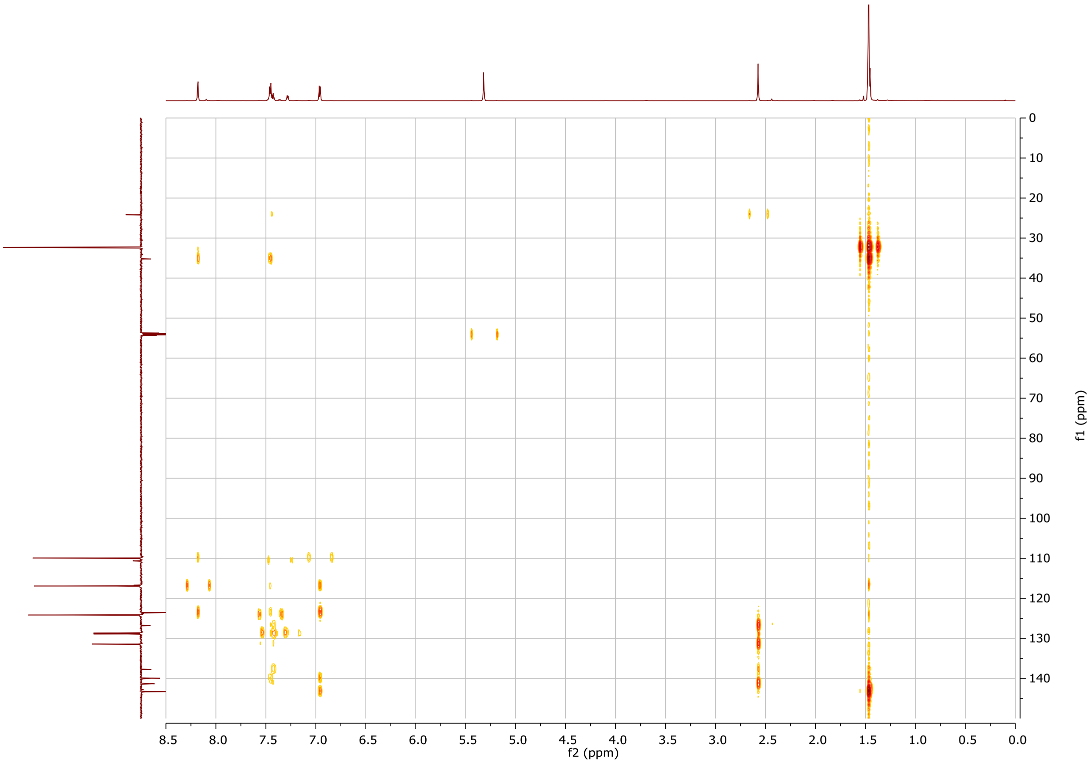

Figure 9.10: HSQC-NMR spectrum of 9-(2-bromo-3-methylphenyl)-3,6-di-*tert*-butyl-9*H*-carbazole, (700 MHz,176 MHz), 298 K, CD_2Cl_2.

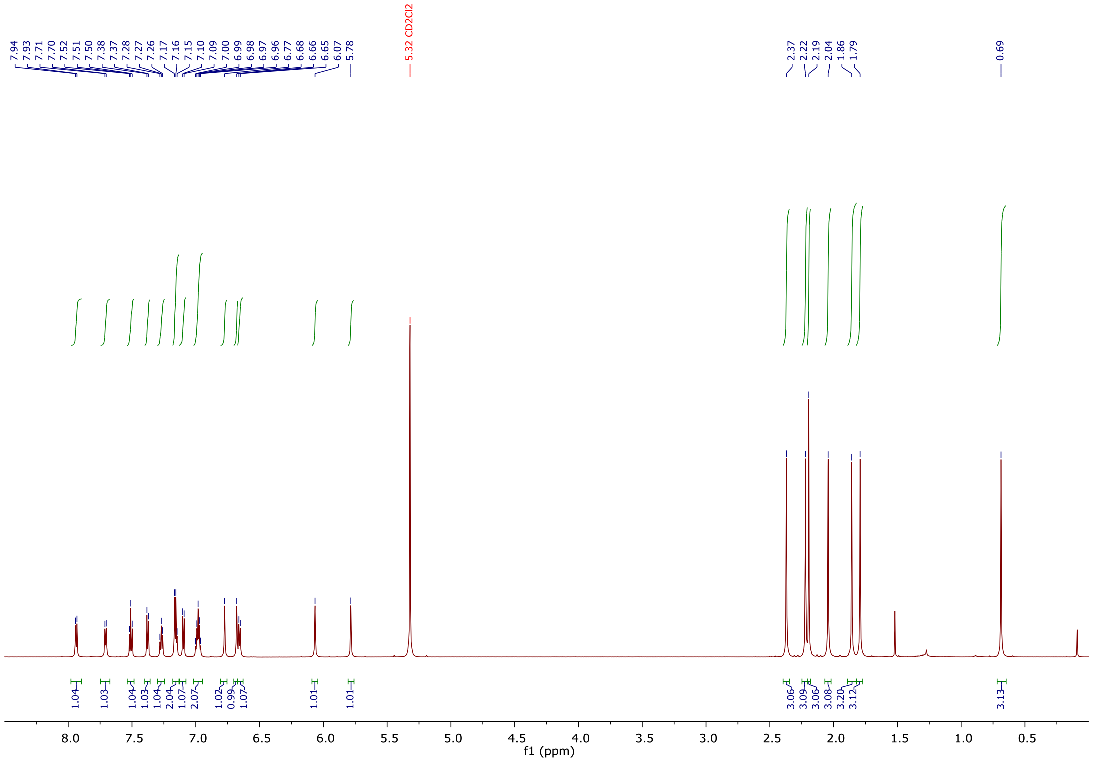

Figure 9.11: ^{1}H-NMR spectrum of 9-(2-(dimesitylboraneyl)-3-methylphenyl)- -9*H*-carbazole, 700 MHz, 298 K, CD_2Cl_2.

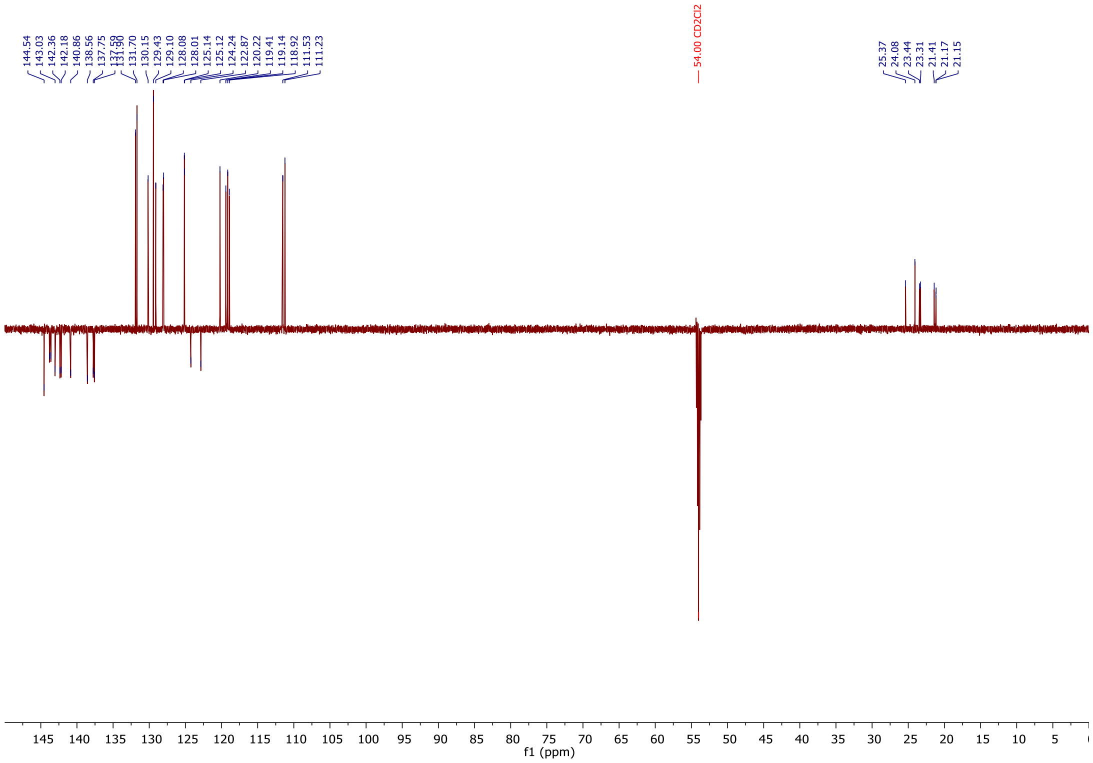

Figure 9.12: ^{13}C-NMR spectrum of 9-(2-(dimesitylboraneyl)-3-methylphenyl)- -9*H*-carbazole, 176 MHz, 298 K, CD_2Cl_2.

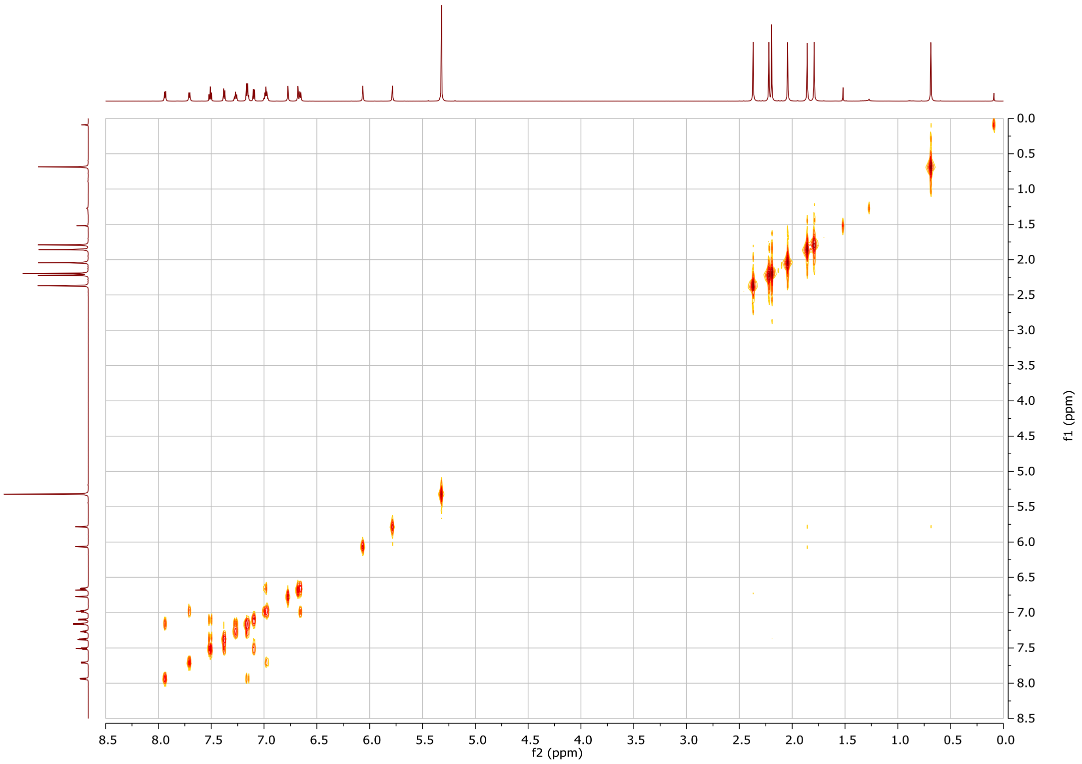

Figure 9.13: COSY-NMR spectrum of 9-(2-(dimesitylboraneyl)-3-methylphenyl)- -9*H*-carbazole, (700 MHz, 700 MHz), 298 K, CD_2Cl_2.

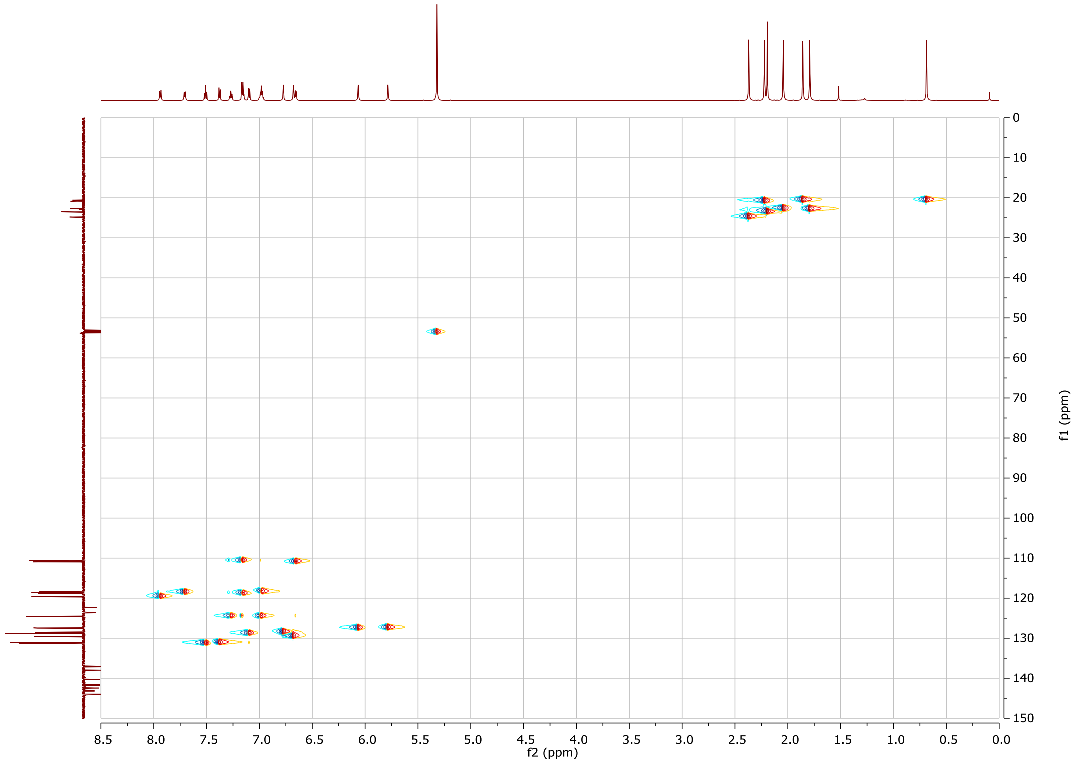

Figure 9.14: HSQC-NMR spectrum of 9-(2-(dimesitylboraneyl)-3-methylphenyl)- -9*H*-carbazole, (700 MHz, 176 MHz), 298 K, CD_2Cl_2.

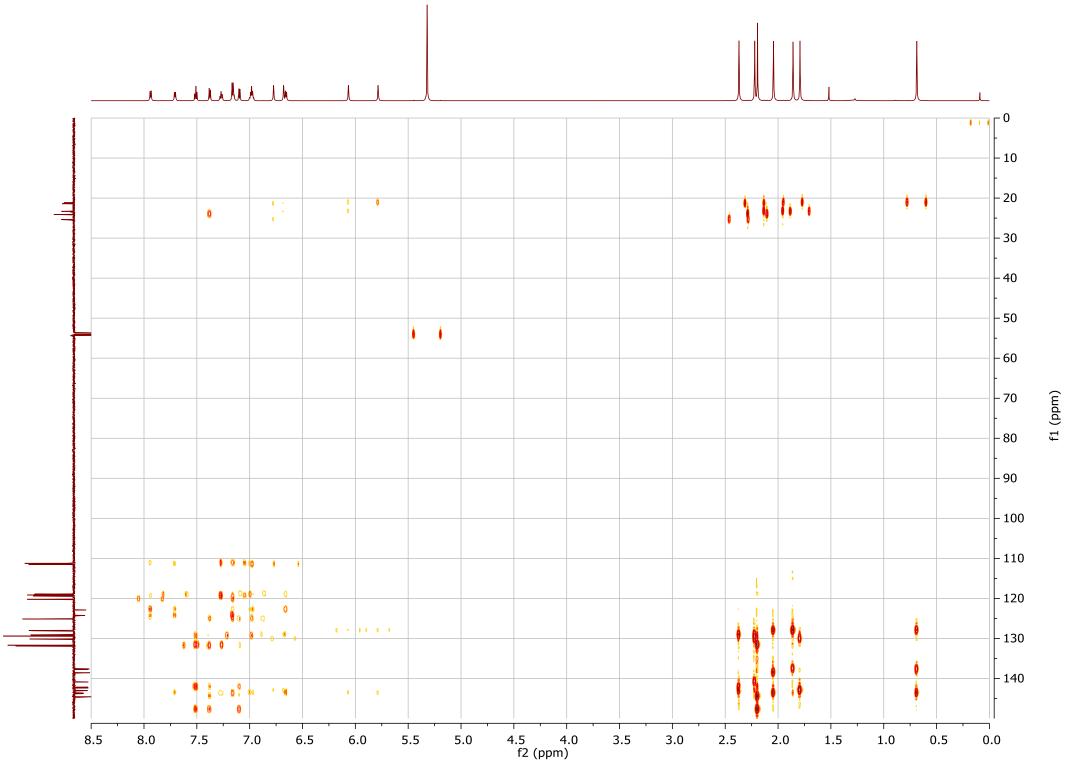

Figure 9.15: HMBC-NMR spectrum of 9-(2-(dimesitylboraneyl)-3-methylphenyl)- -9*H*-carbazole, (700 MHz, 176 MHz), 298 K, CD_2Cl_2.

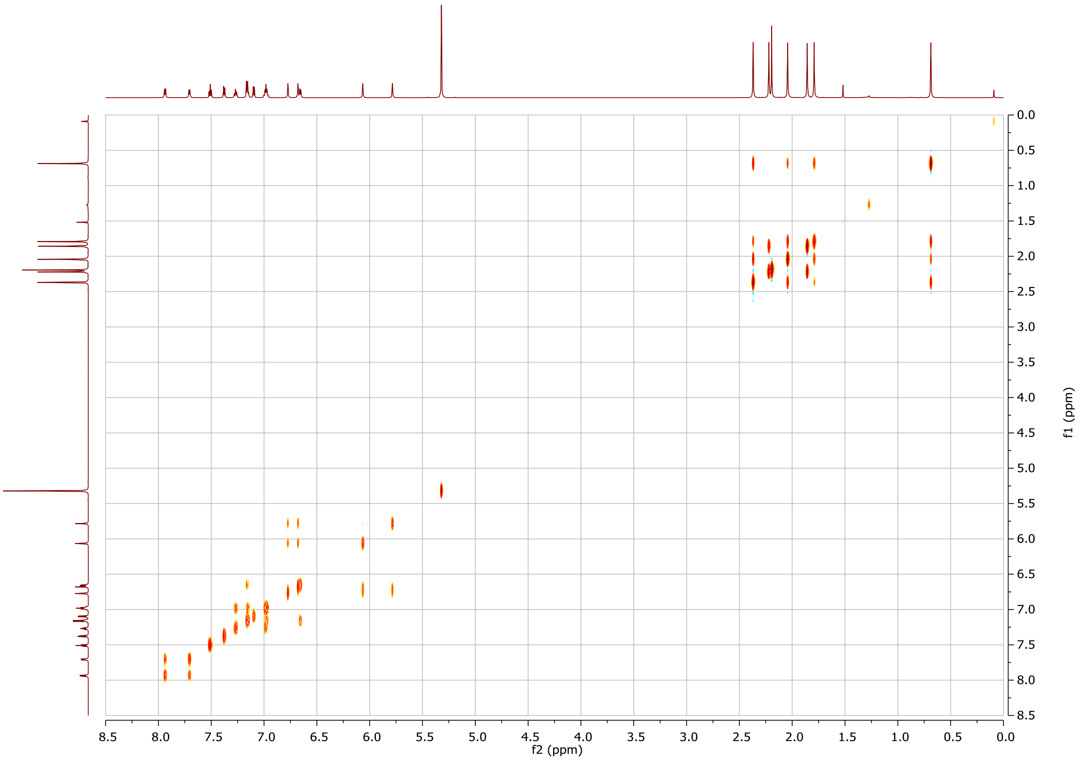

Figure 9.16: NOESY-NMR spectrum of 9-(2-(dimesitylboraneyl)-3-methylphenyl)- -9*H*-carbazole, (700 MHz, 176 MHz), 298 K, CD_2Cl_2.

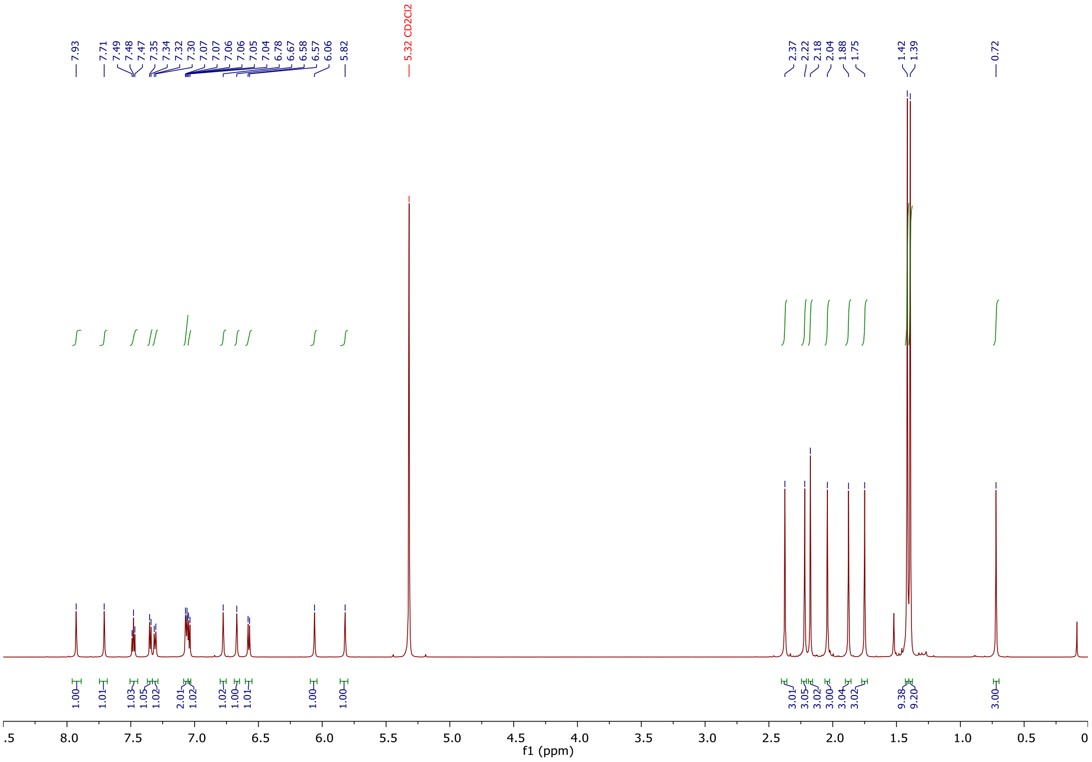

Figure 9.17: ^{1}H-NMR spectrum of 3,6-di-*tert*-butyl-9-(2-(dimesitylboraneyl)-3-methylphenyl)-9*H*-carbazole, 700 MHz, 298 K, CD_2Cl_2.

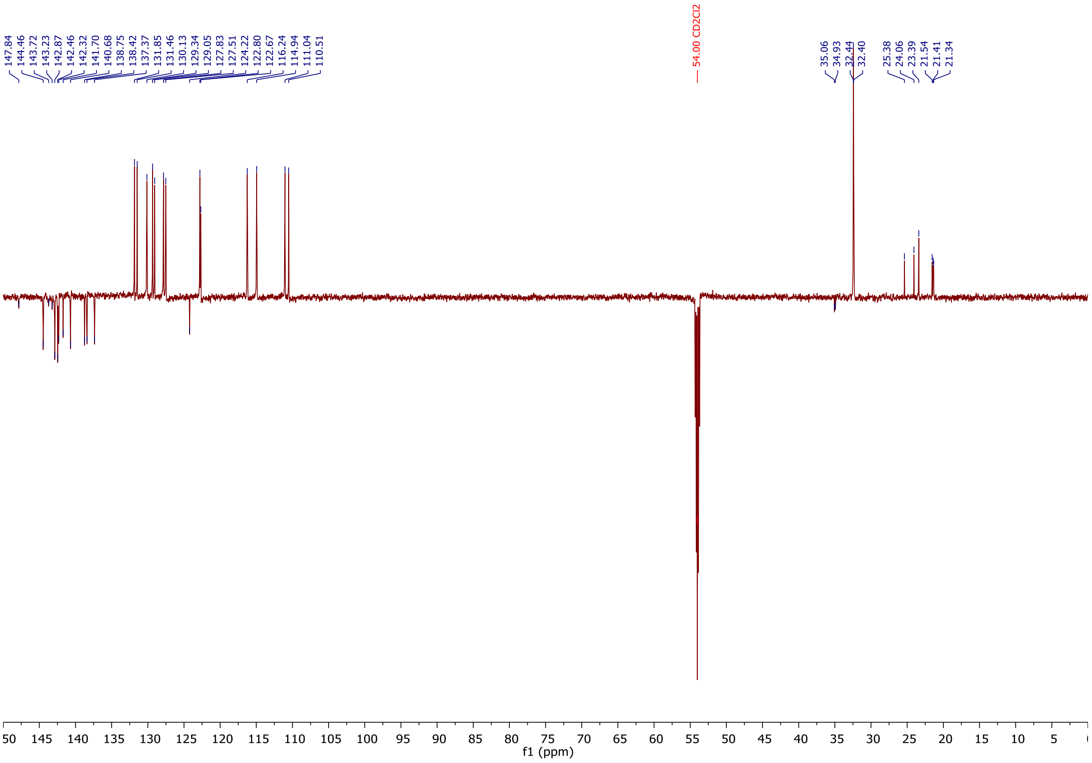

Figure 9.18: ^{13}C-NMR spectrum of 3,6-di-*tert*-butyl-9-(2-(dimesitylboraneyl)-3-methylphenyl)-9*H*-carbazole, 176 MHz, 298 K, CD_2Cl_2.

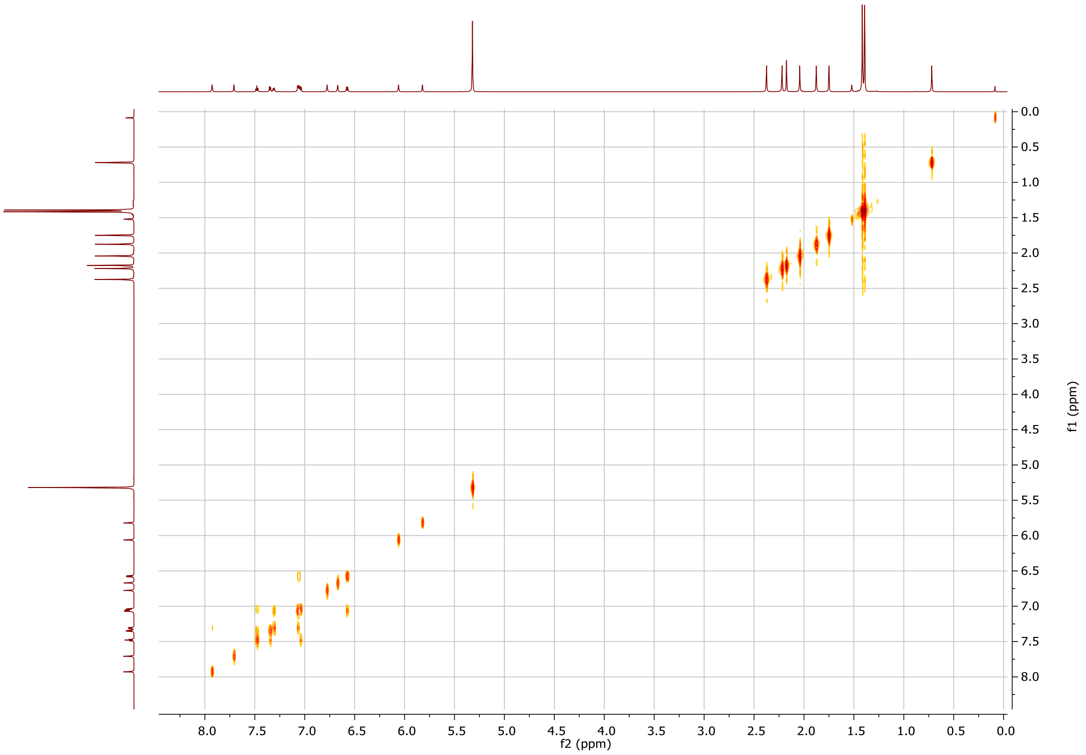

Figure 9.19: COSY-NMR spectrum of 3,6-di-*tert*-butyl-9-(2-(dimesitylboraneyl)-3-methylphenyl)-9*H*-carbazole, (700 MHz, 700 MHz), 298 K, CD_2Cl_2.

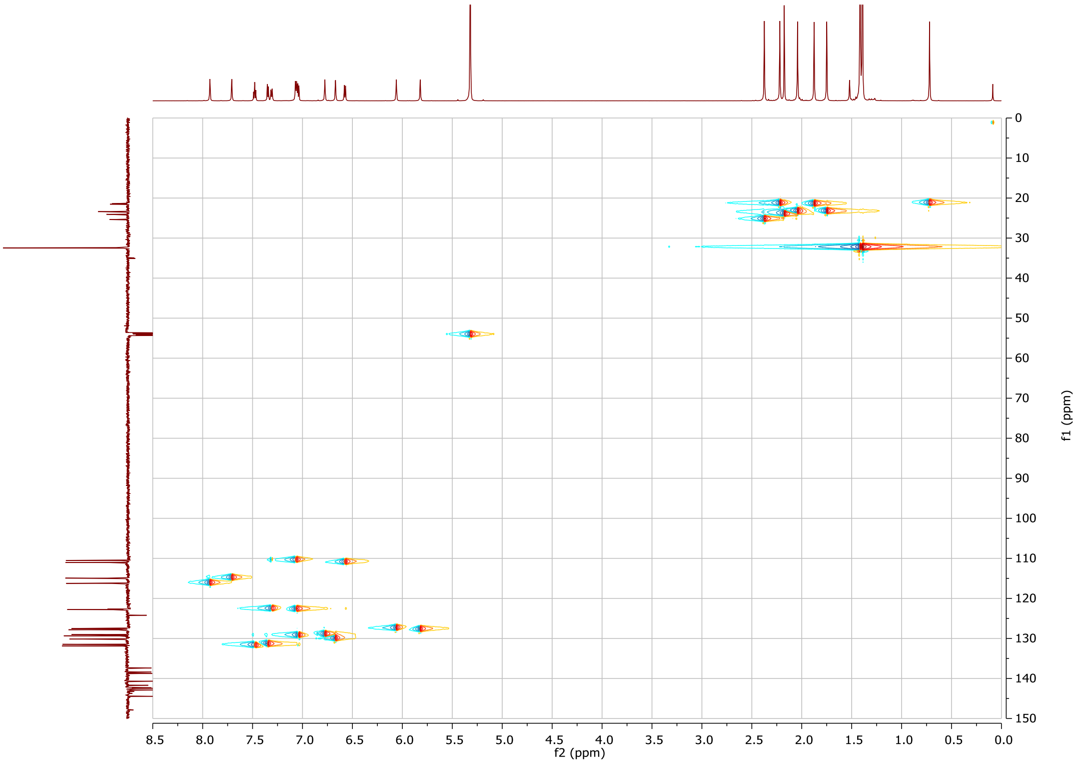

Figure 9.20: HSQC-NMR spectrum of 3,6-di-*tert*-butyl-9-(2-(dimesitylboraneyl)-3-methylphenyl)-9*H*-carbazole, (700 MHz, 176 MHz), 298 K, CD_2Cl_2.

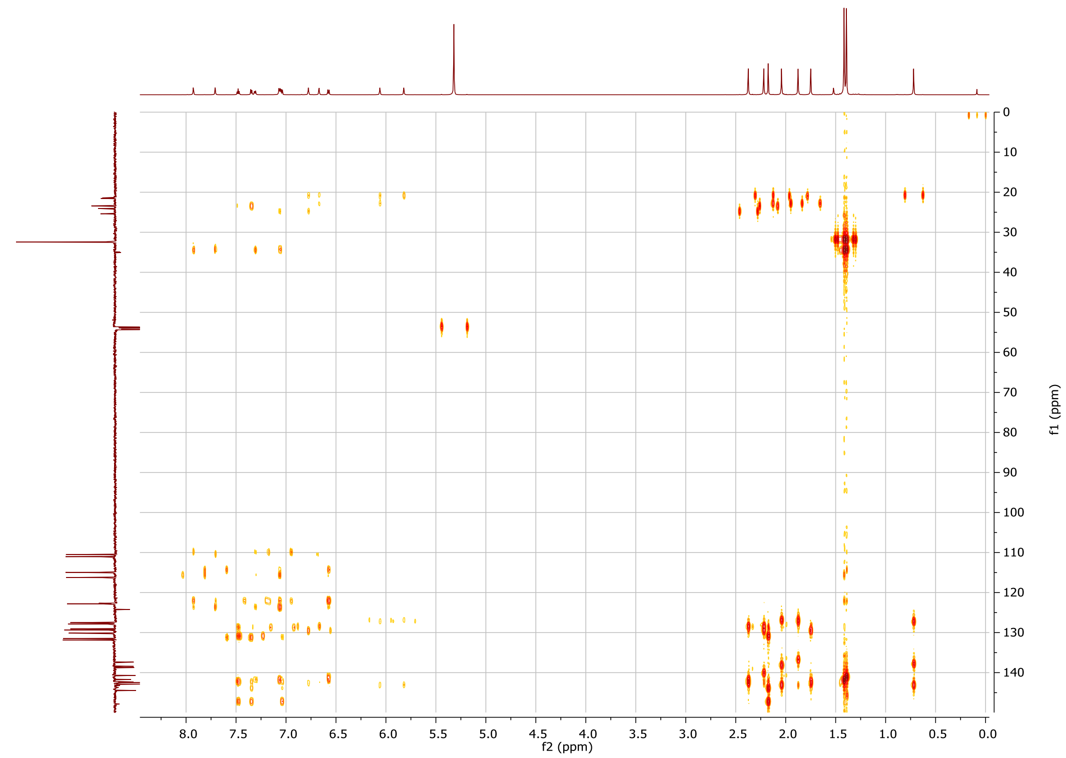

Figure 9.21: HMBC-NMR spectrum of 3,6-di-*tert*-butyl-9-(2-(dimesitylboraneyl)-3-methylphenyl)-9*H*-carbazole, (700 MHz, 176 MHz), 298 K, CD_2Cl_2.

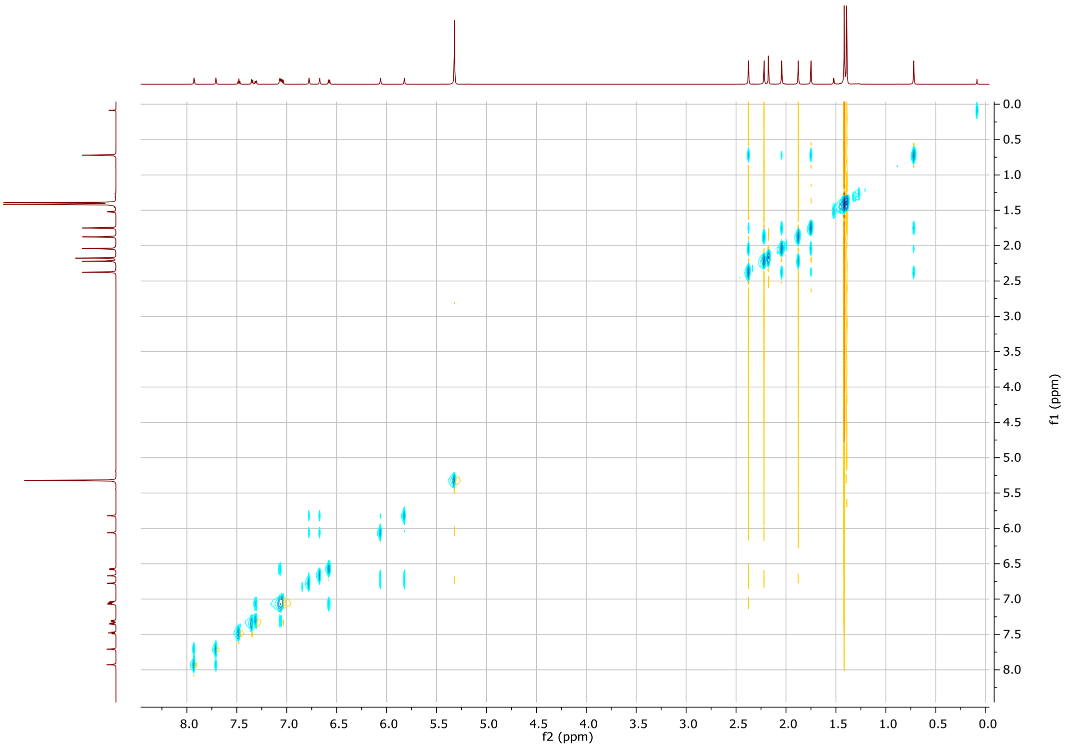

Figure 9.22: NOESY-NMR spectrum of 3,6-di-*tert*-butyl-9-(2-(dimesitylboraneyl)-3-methylphenyl)-9*H*-carbazole, (700 MHz, 700 MHz), 298 K, CD_2Cl_2.

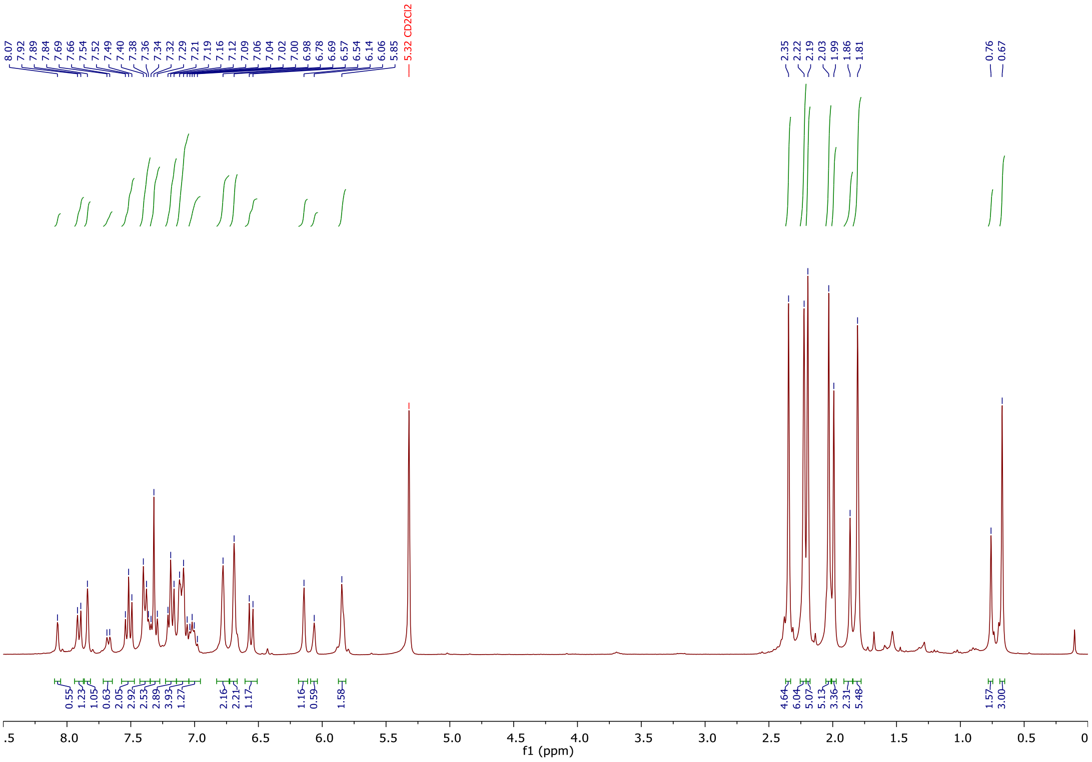

Figure 9.23: ^{1}H-NMR spectrum of monobrominated 9-(2-(dimesitylboraneyl)-3-methylphenyl)-9*H*-carbazole, 300 MHz, 297 K, CD_2Cl_2.

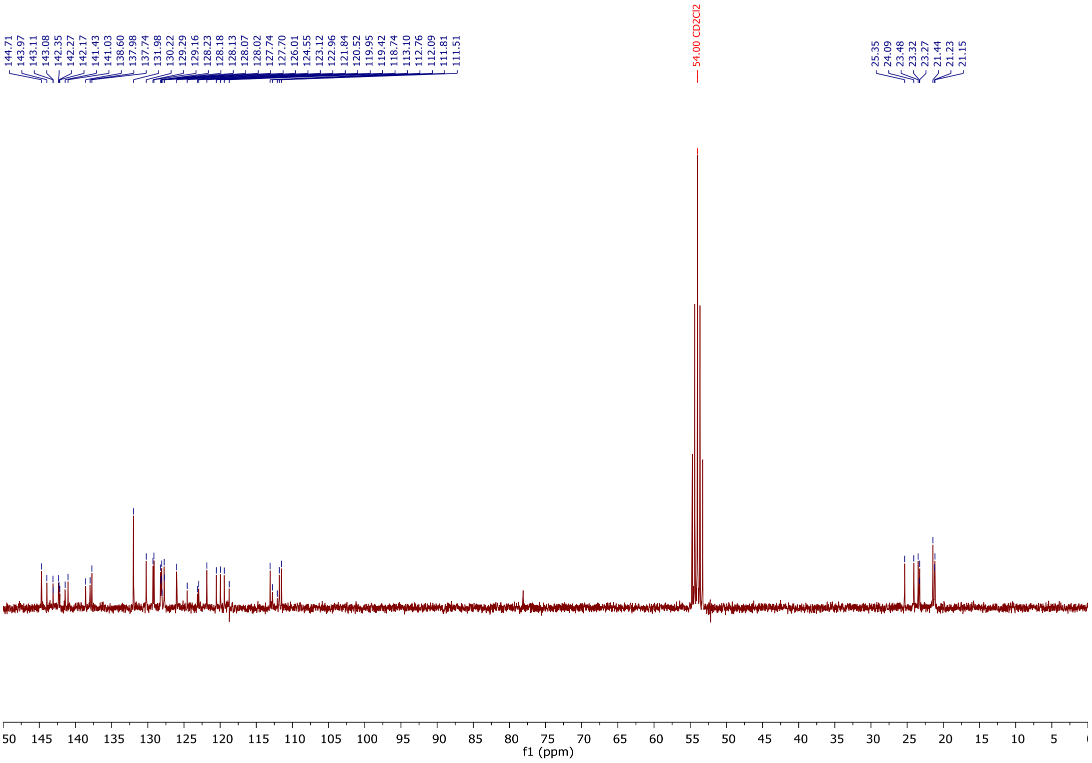

Figure 9.24: ^{13}C-NMR spectrum of monobrominated 9-(2-(dimesitylboraneyl)-3-methylphenyl)-9*H*-carbazole, 75 MHz, 297 K, CD_2Cl_2.

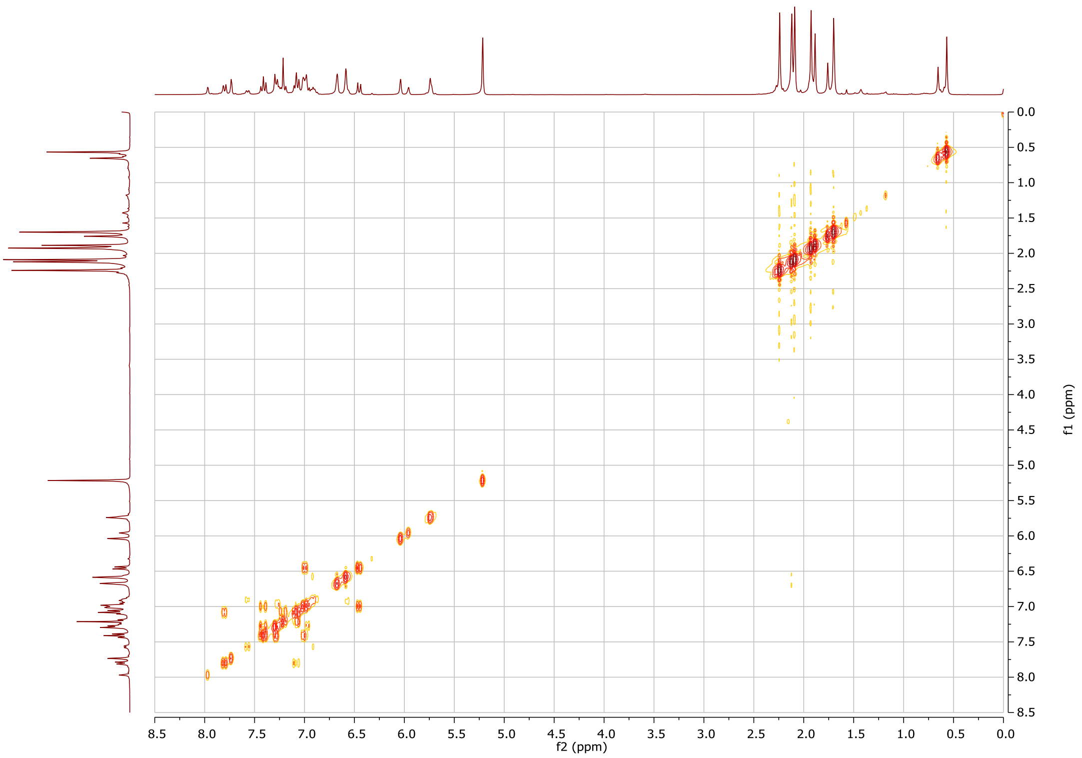

Figure 9.25: COSY-NMR spectrum of monobrominated 9-(2-(dimesitylboraneyl)-3-methylphenyl)-9*H*-carbazole, (300 MHz, 300 MHz), 297 K, CD_2Cl_2.

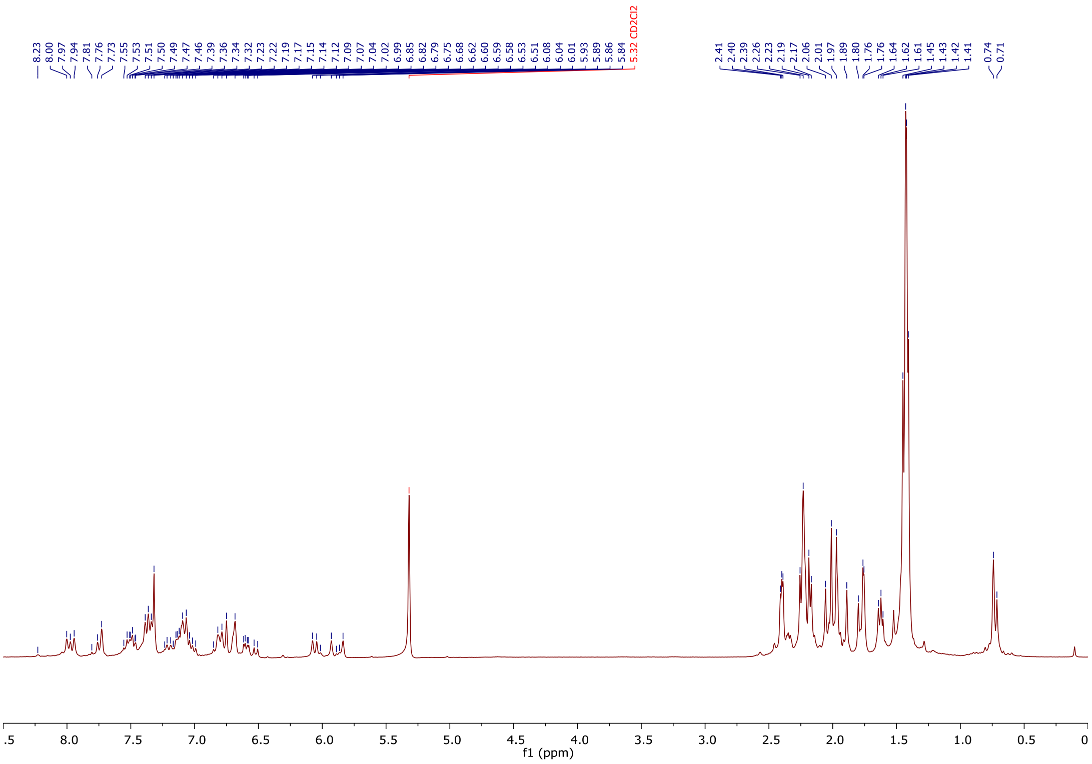

Figure 9.26: ^{1}H-NMR spectrum of monobromination of 3,6-di-*tert*-butyl-9-(2-(dimesitylboraneyl)-3-methylphenyl)-9*H*-carbazole, 300 MHz, 297 K, CD_2Cl_2.

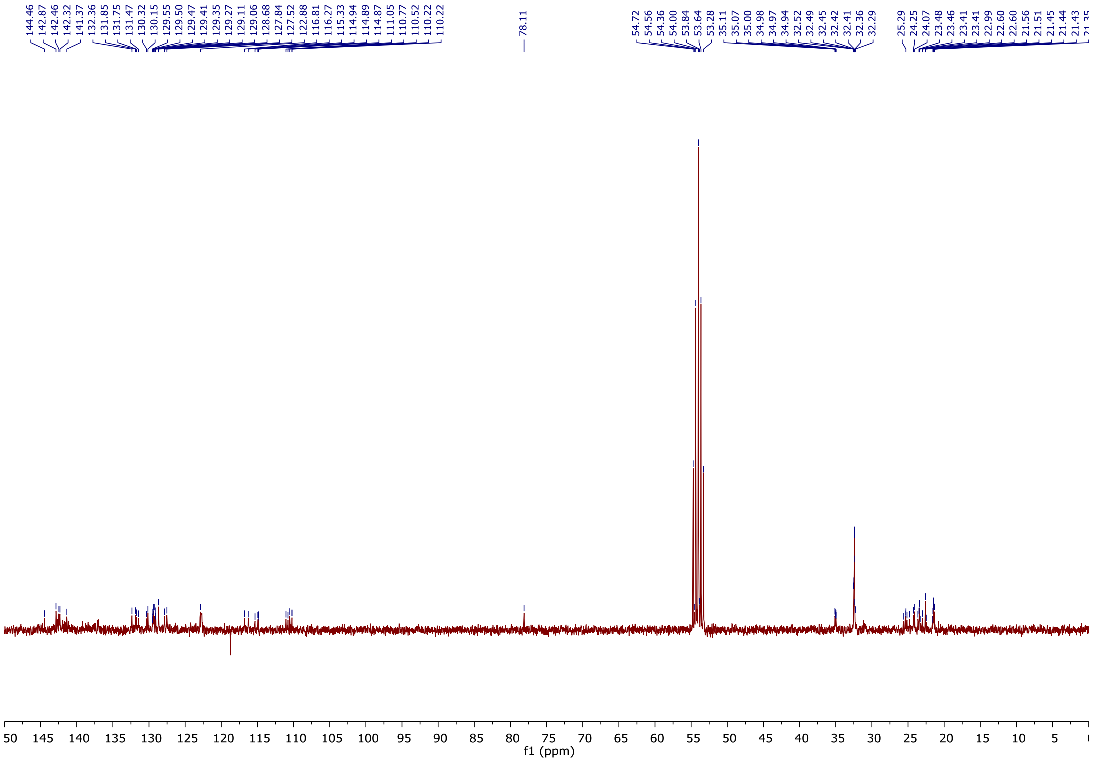

Figure 9.27: ^{13}C-NMR spectrum of 3,6-di-*tert*-butyl-9-(2-(dimesitylboraneyl)-3-methylphenyl)-9*H*-carbazole, 75 MHz, 297 K, CD_2Cl_2.

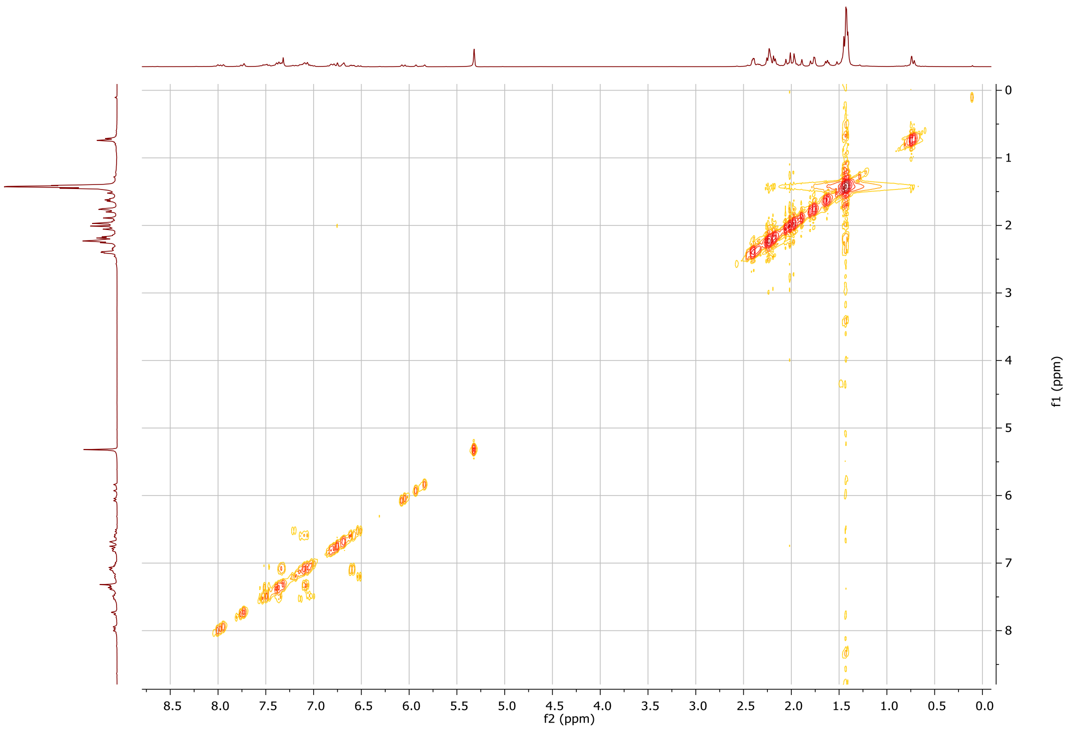

Figure 9.28: COSY-NMR spectrum of 3,6-di-*tert*-butyl-9-(2-(dimesitylboraneyl)-3-methylphenyl)-9*H*-carbazole, (300 MHz, 300 MHz), 297 K, CD_2Cl_2.

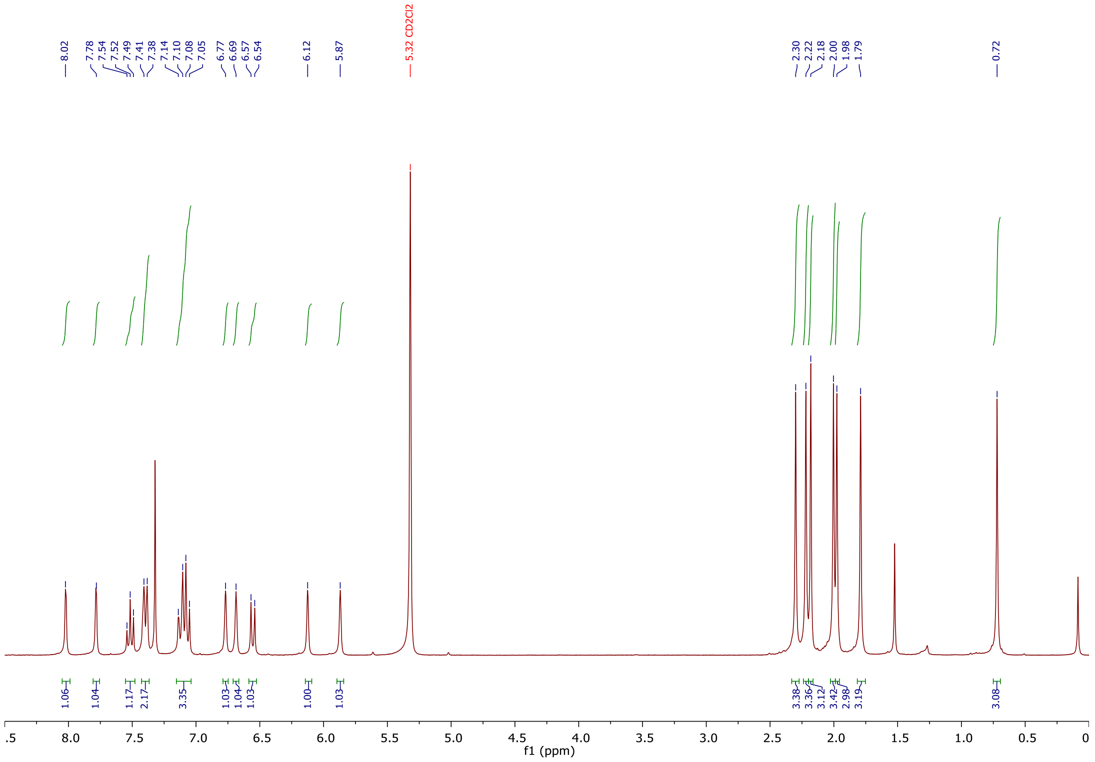

Figure 9.29: ^{1}H-NMR spectrum of dibrominated 9-(2-(dimesitylboraneyl)-3-methylphenyl)-9*H*-carbazole, 300 MHz, 297 K, CD_2Cl_2.

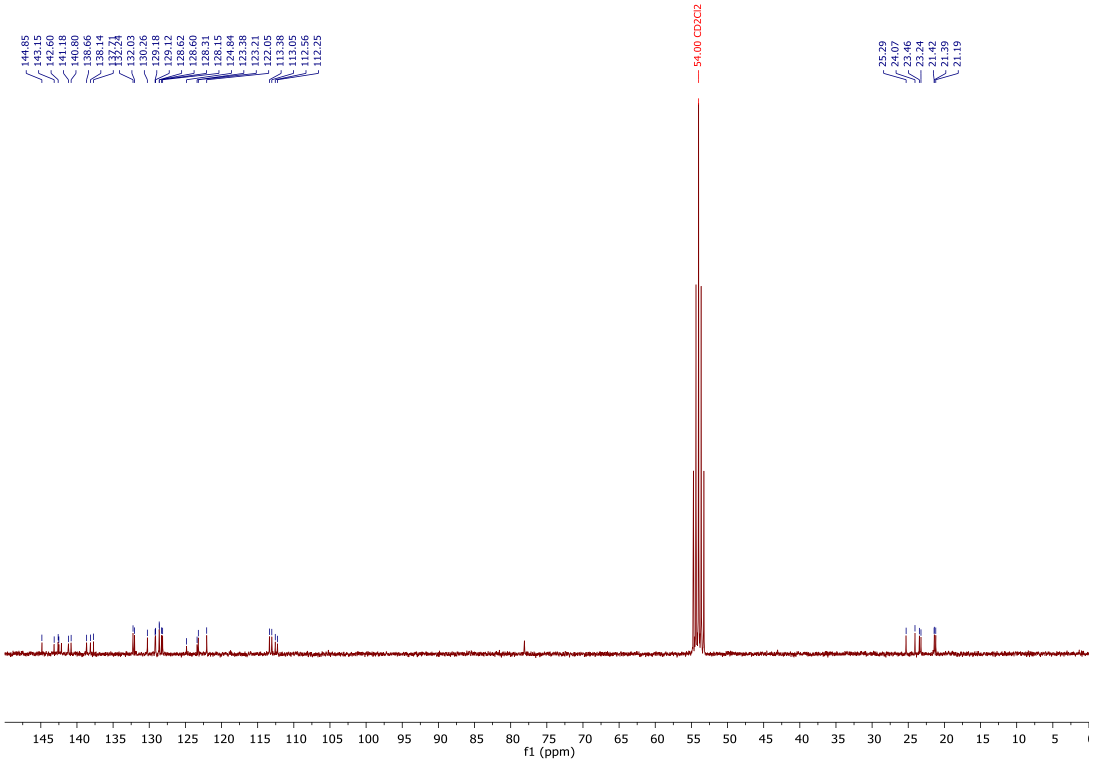

Figure 9.30: ^{13}C-NMR spectrum of dibrominated 9-(2-(dimesitylboraneyl)-3-methylphenyl)-9*H*-carbazole, 75 MHz, 297 K, CD_2Cl_2.

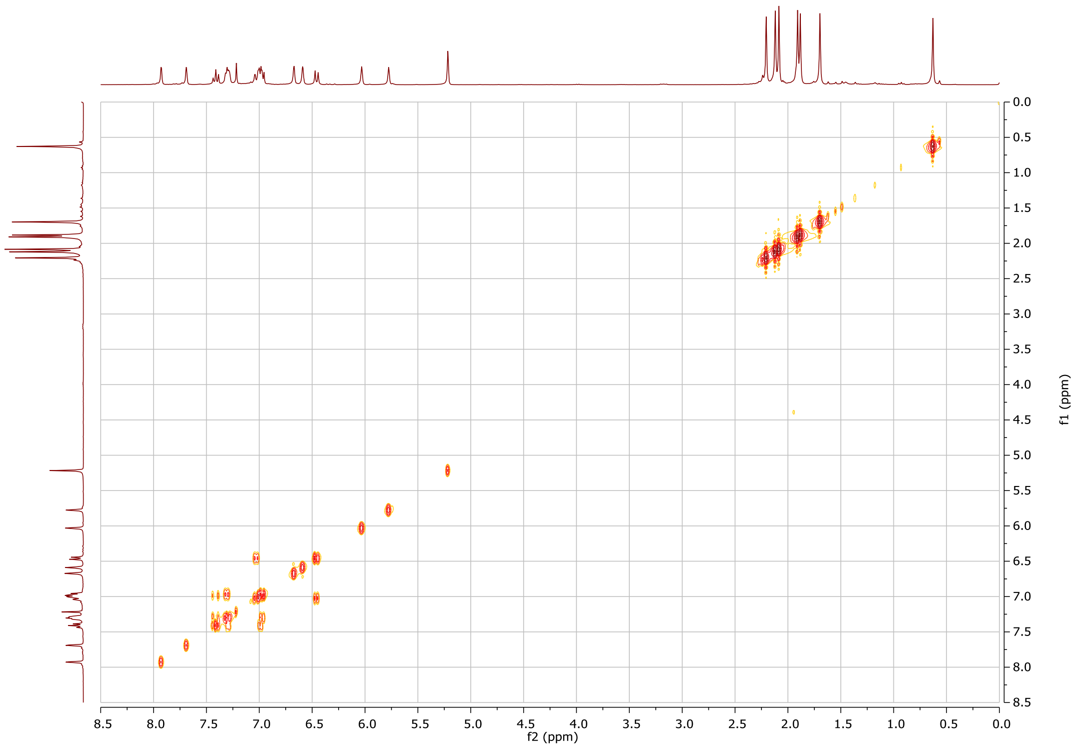

Figure 9.31: COSY-NMR spectrum of dibrominated 9-(2-(dimesitylboraneyl)-3-methylphenyl)-9*H*-carbazole, (300 MHz, 300 MHz), 297 K, CD_2Cl_2.

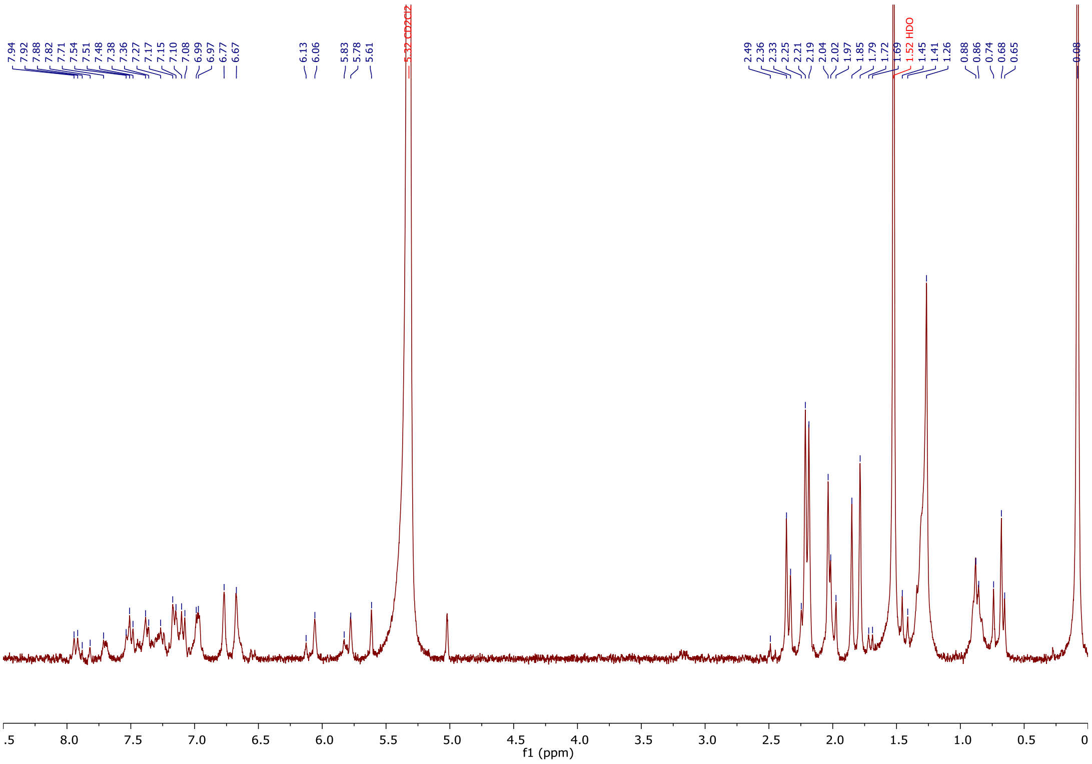

Figure 9.32: ^1H-NMR spectrum of SUZUKI cross-coupling reaction of monobrominated 9-(2-(dimesitylboraneyl)-3-methylphenyl)-9*H*-carbazole with 4,4,5,5-tetramethyl-2-(4-vinylphenyl)-1,3,2-dioxaborolane, 300 MHz, 297 K, CD_2Cl_2.

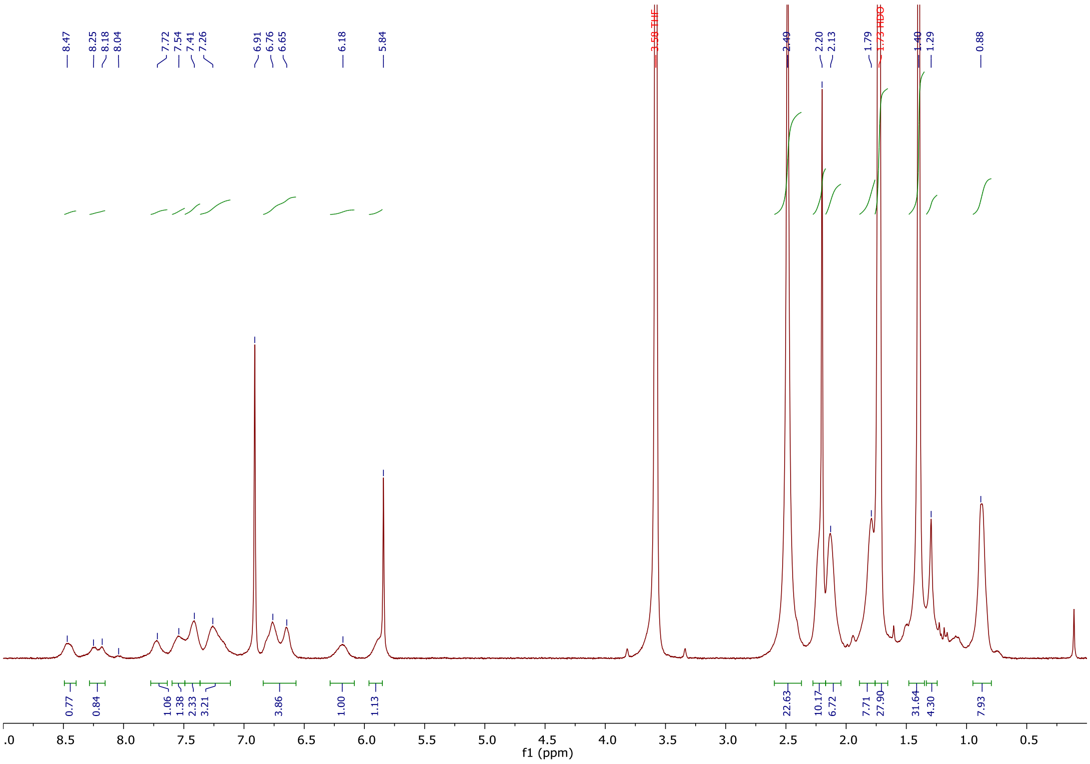

Figure 9.33: ^{1}H-NMR spectrum of poly-(9-(2-(dimesitylboraneyl)-3-methylphenyl)-9*H*-carbazole), 300 MHz, 297 K, THF-d_8.

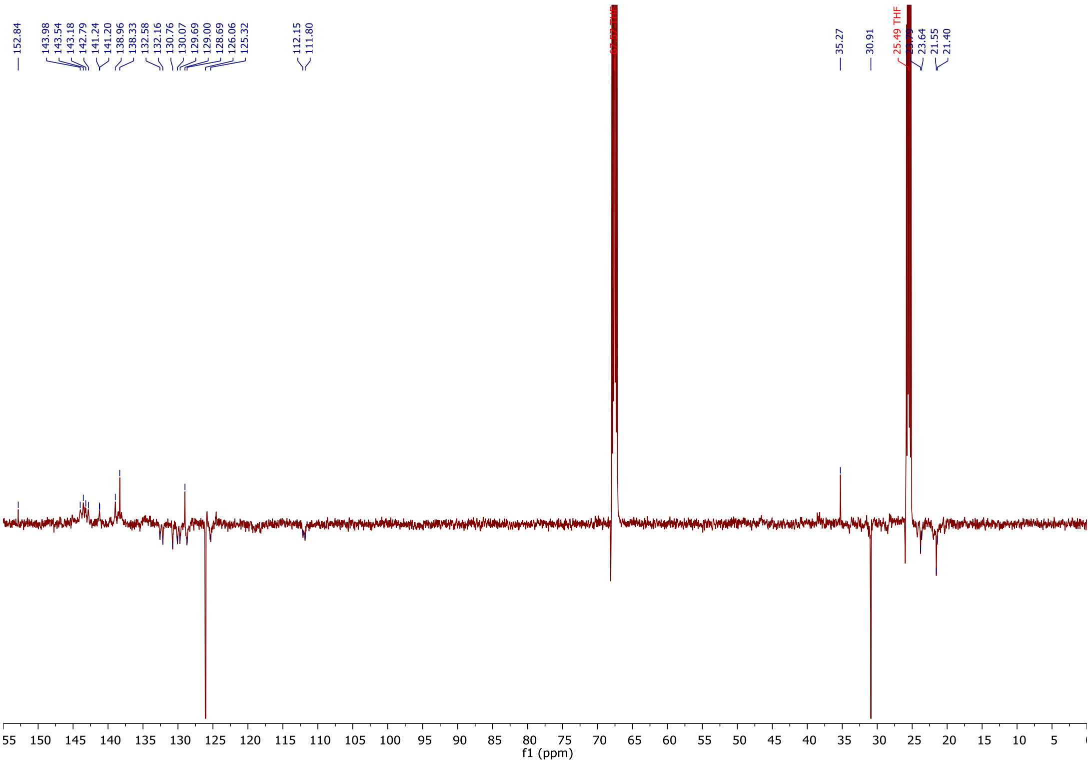

Figure 9.34: ^{13}C-NMR of poly-(9-(2-(dimesitylboraneyl)-3-methylphenyl)-9*H*-carbazole), 75 MHz, 297 K, THF-d_8.

9.2 GPC elugrams

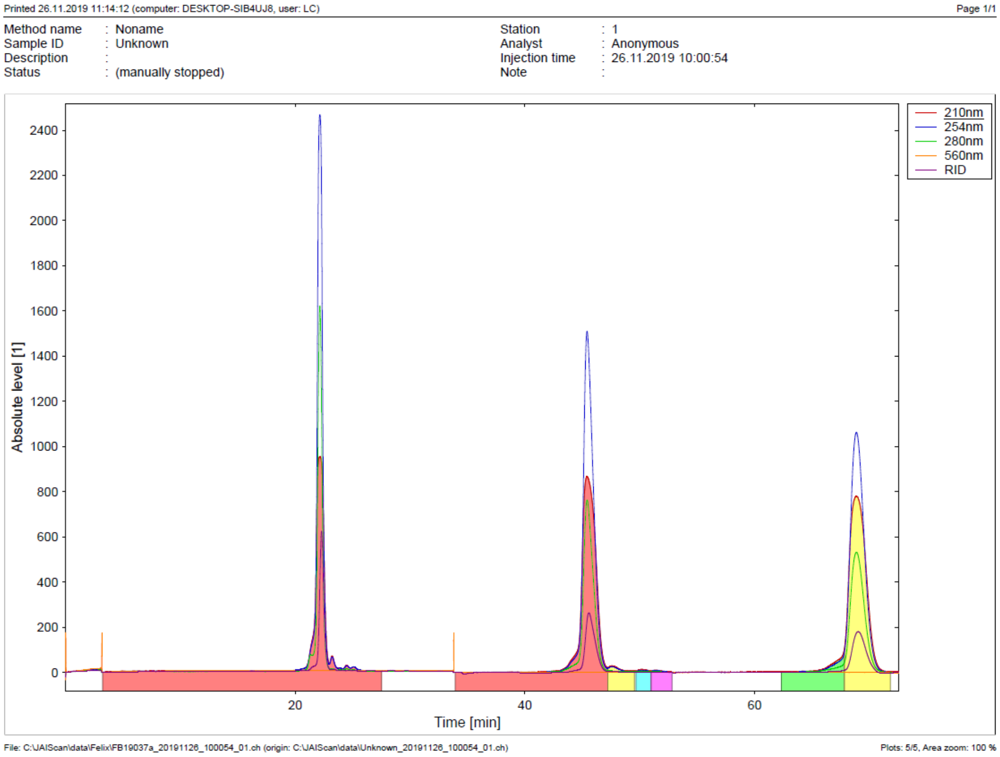

Printed 26.11.2019 11:14:12 (computer: DESKTOP-SIB4UJ8, user: LC) Page 1/1

Method name : Noname
Sample ID : Unknown
Description :
Status : (manually stopped)

Station : 1
Analyst : Anonymous
Injection time : 26.11.2019 10:00:54
Note :

File: C:\JAIScan\data\Felix\FB19037a_20191126_100054_01.ch (origin: C:\JAIScan\data\Unknown_20191126_100054_01.ch)

Plots: 5/5, Area zoom: 100 %

Figure 9.35: Preparative GPC of monobromination of 9-(2-(dimesitylboraneyl)-3-methylphenyl)-9*H*-carbazole. $c = 100$ mg/mL, recycling mode, UV detector, $p = 10$ mL/s.

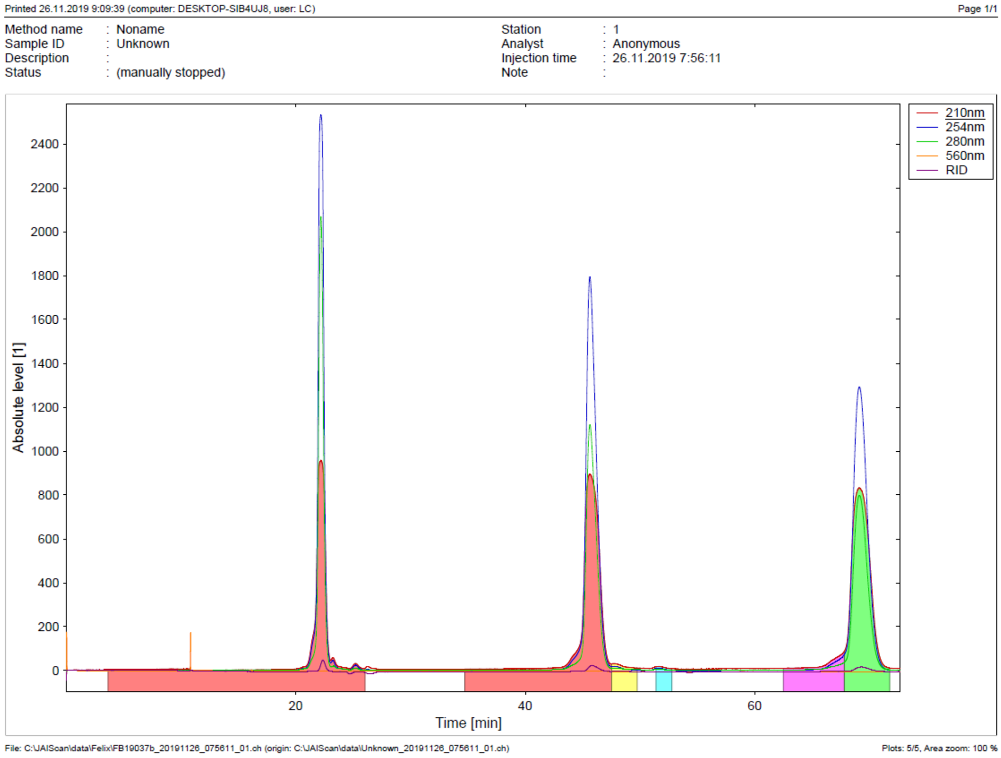

Printed 26.11.2019 9:09:39 (computer: DESKTOP-SIB4UJ8, user: LC) Page 1/1

Method name : Noname
Sample ID : Unknown
Description :
Status : (manually stopped)

Station : 1
Analyst : Anonymous
Injection time : 26.11.2019 7:56:11
Note :

File: C:\JAIScan\data\Felix\FB19037b_20191126_075611_01.ch (origin: C:\JAIScan\data\Unknown_20191126_075611_01.ch)

Plots: 5/5, Area zoom: 100 %

Figure 9.36: Preparative GPC of dibromination of 9-(2-(dimesitylboraneyl)-3-methylphenyl)-9*H*-carbazole. $c = 100$ mg/mL, recycling mode, UV detector, $p = 10$ mL/s.

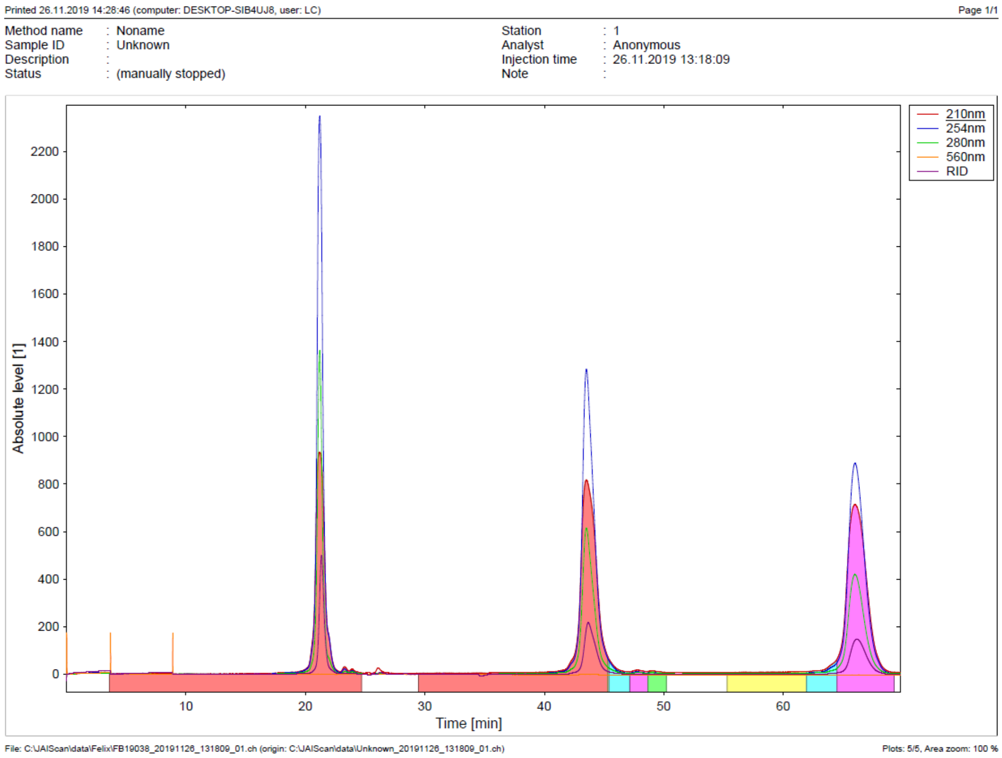

Printed 26.11.2019 14:28:46 (computer: DESKTOP-SIB4UJ8, user: LC) Page 1/1

Method name : Noname
Sample ID : Unknown
Description :
Status : (manually stopped)

Station : 1
Analyst : Anonymous
Injection time : 26.11.2019 13:18:09
Note :

File: C:\JAIScan\data\Felix\FB19038_20191126_131809_01.ch (origin: C:\JAIScan\data\Unknown_20191126_131809_01.ch) Plots: 5/5, Area zoom: 100 %

Figure 9.37: Preparative GPC of monobromination of 3,6-di-*tert*-butyl-9-(2-(dimesitylboraneyl)-3-methylphenyl)-9*H*-carbazole. c = 100 mg/mL, recycling mode, UV detector, p = 10 mL/s.

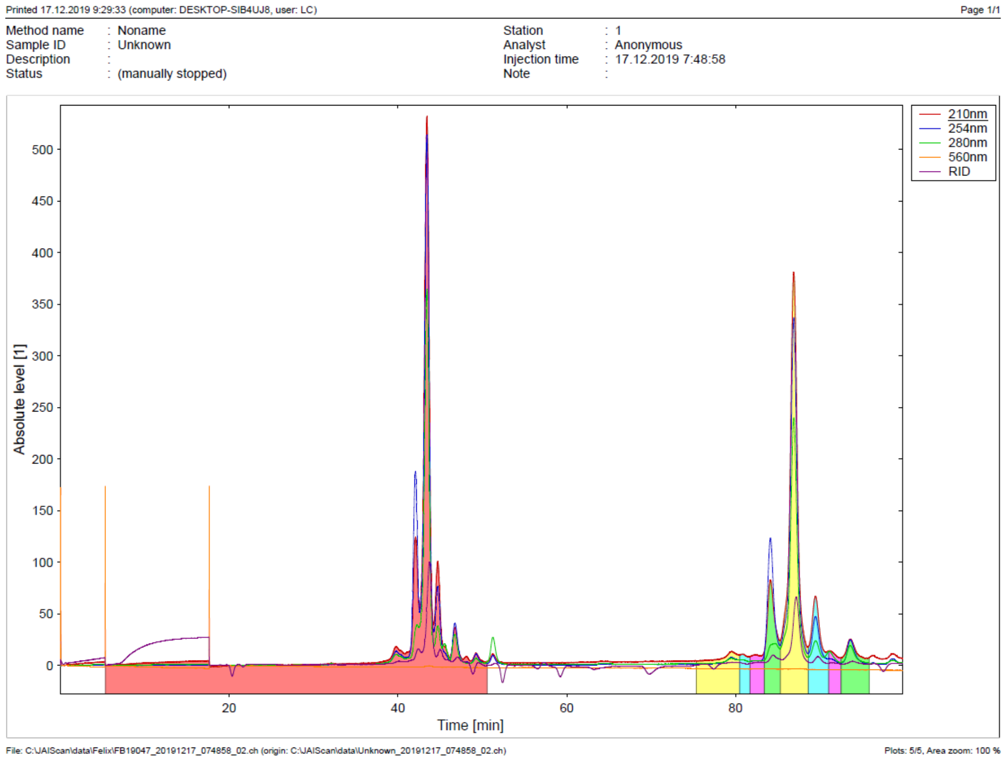

Printed 17.12.2019 9:29:33 (computer: DESKTOP-SIB4UJ8, user: LC) Page 1/1

Method name : Noname
Sample ID : Unknown
Description :
Status : (manually stopped)

Station : 1
Analyst : Anonymous
Injection time : 17.12.2019 7:48:58
Note :

File: C:\JAIScan\data\Felix\FB19047_20191217_074858_02.ch (origin: C:\JAIScan\data\Unknown_20191217_074858_02.ch) Plots: 5/5, Area zoom: 100 %

Figure 9.38: Preparative GPC of Suzuki cross-coupling reaction of monobrominated 9-(2-(dimesitylboraneyl)-3-methylphenyl)-9*H*-carbazole with 4,4,5,5-tetramethyl-2-(4-vinylphenyl)-1,3,2-dioxaborolane. c = 100 mg/mL, recycling mode, UV detector, p = 5 mL/s.

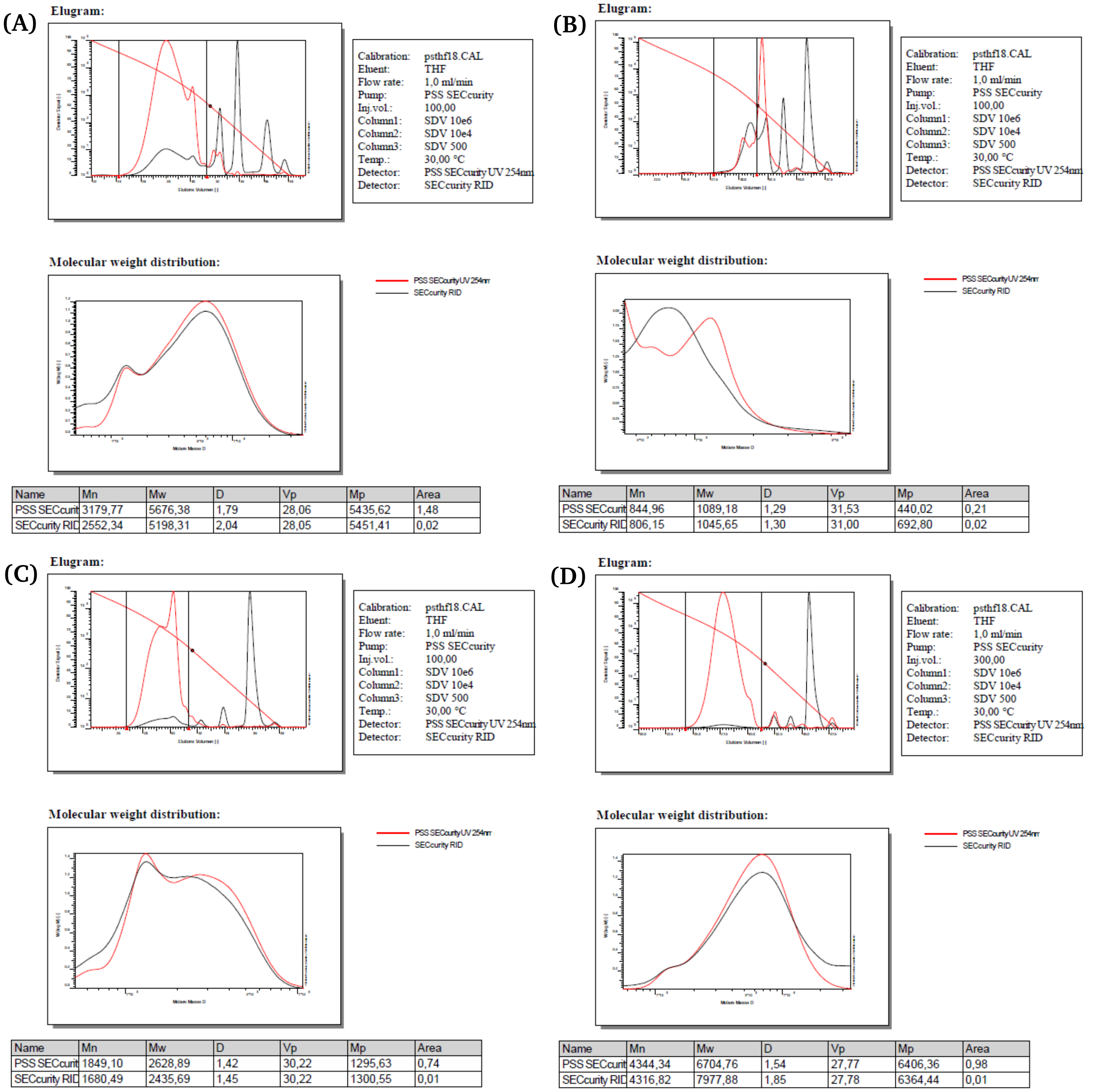

(A)

Calibration: psthf18.CAL
Eluent: THF
Flow rate: 1,0 ml/min
Pump: PSS SECcurity
Inj.vol.: 100,00
Column1: SDV 10e6
Column2: SDV 10e4
Column3: SDV 500
Temp.: 30,00 °C
Detector: PSS SECcurity UV 254nm
Detector: SECcurity RID

Name	Mn	Mw	D	Vp	Mp	Area
PSS SECcurit	3179,77	5676,38	1,79	28,06	5435,62	1,48
SECcurity RID	2552,34	5198,31	2,04	28,05	5451,41	0,02

(B)

Calibration: psthf18.CAL
Eluent: THF
Flow rate: 1,0 ml/min
Pump: PSS SECcurity
Inj.vol.: 100,00
Column1: SDV 10e6
Column2: SDV 10e4
Column3: SDV 500
Temp.: 30,00 °C
Detector: PSS SECcurity UV 254nm
Detector: SECcurity RID

Name	Mn	Mw	D	Vp	Mp	Area
PSS SECcurit	844,96	1089,18	1,29	31,53	440,02	0,21
SECcurity RID	806,15	1045,65	1,30	31,00	692,80	0,02

(C)

Calibration: psthf18.CAL
Eluent: THF
Flow rate: 1,0 ml/min
Pump: PSS SECcurity
Inj.vol.: 100,00
Column1: SDV 10e6
Column2: SDV 10e4
Column3: SDV 500
Temp.: 30,00 °C
Detector: PSS SECcurity UV 254nm
Detector: SECcurity RID

Name	Mn	Mw	D	Vp	Mp	Area
PSS SECcurit	1849,10	2628,89	1,42	30,22	1295,63	0,74
SECcurity RID	1680,49	2435,69	1,45	30,22	1300,55	0,01

(D)

Calibration: psthf18.CAL
Eluent: THF
Flow rate: 1,0 ml/min
Pump: PSS SECcurity
Inj.vol.: 300,00
Column1: SDV 10e6
Column2: SDV 10e4
Column3: SDV 500
Temp.: 30,00 °C
Detector: PSS SECcurity UV 254nm
Detector: SECcurity RID

Name	Mn	Mw	D	Vp	Mp	Area
PSS SECcurit	4344,34	6704,76	1,54	27,77	6406,36	0,98
SECcurity RID	4316,82	7977,88	1,85	27,78	6364,44	0,01

Figure 9.39: Analytical GPC Elugrams and molecular weight distributions after different steps of Soxhlet extraction. **(A)** crude, **(B)** methanol, **(C)** acetone, **(D)** final product.

9.3 AFM pictures

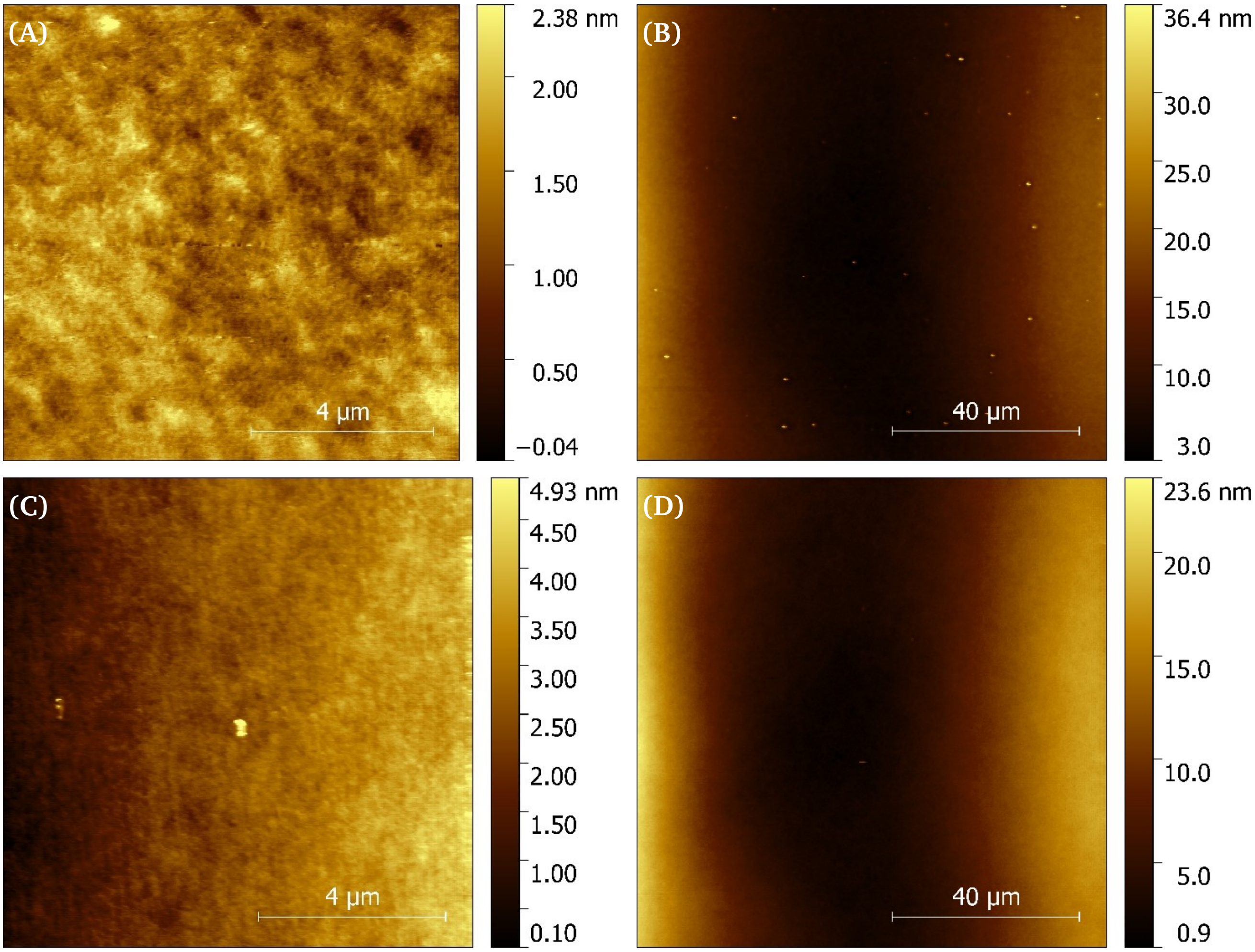

Figure 9.40: AFM-pictures after spin-coating B-oCz and B-oTC on glass substrates treated with UV/ozone. **(A)** B-oCz, 1500 rpm, 10x10 µm^2, RMS = 0.271 nm. **(B)** B-oCz, 1500 rpm, 100x100 µm^2, RMS = 5.643 nm. **(C)** B.oTC, 1500 rpm, 10x10 µm^2, RMS = 0.984 nm. **(D)** B-oTC, 1500 rpm, 100x100 µm^2, RMS = 5.336 nm.

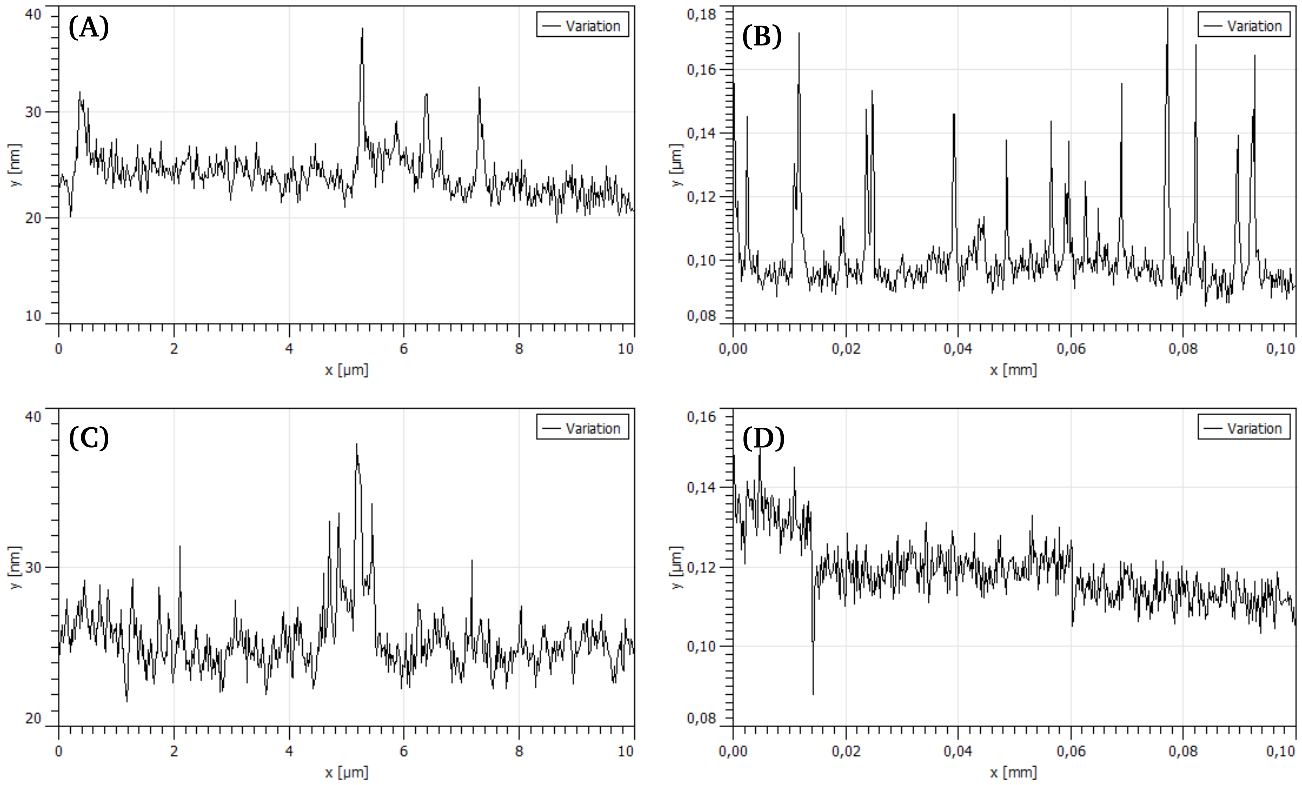

Figure 9.41: AFM-profiles after spin-coating B-oCz and B-oTC on glass substrates treated with UV/ozone. **(A)** B-oCz, 1500 rpm, 10x10 µm^2, RMS = 0.271 nm. **(B)** B-oCz, 1500 rpm, 100x100 µm^2, RMS = 5.643 nm. **(C)** B.oTC, 1500 rpm, 10x10 µm^2, RMS = 0.984 nm. **(D)** B-oTC, 1500 rpm, 100x100 µm^2, RMS = 5.336 nm.

9.4 Photophysical results of 3,6-di-*tert*-butyl-9-(2-(dimesitylboraneyl)-3-methylphenyl)-9*H*-carbazole

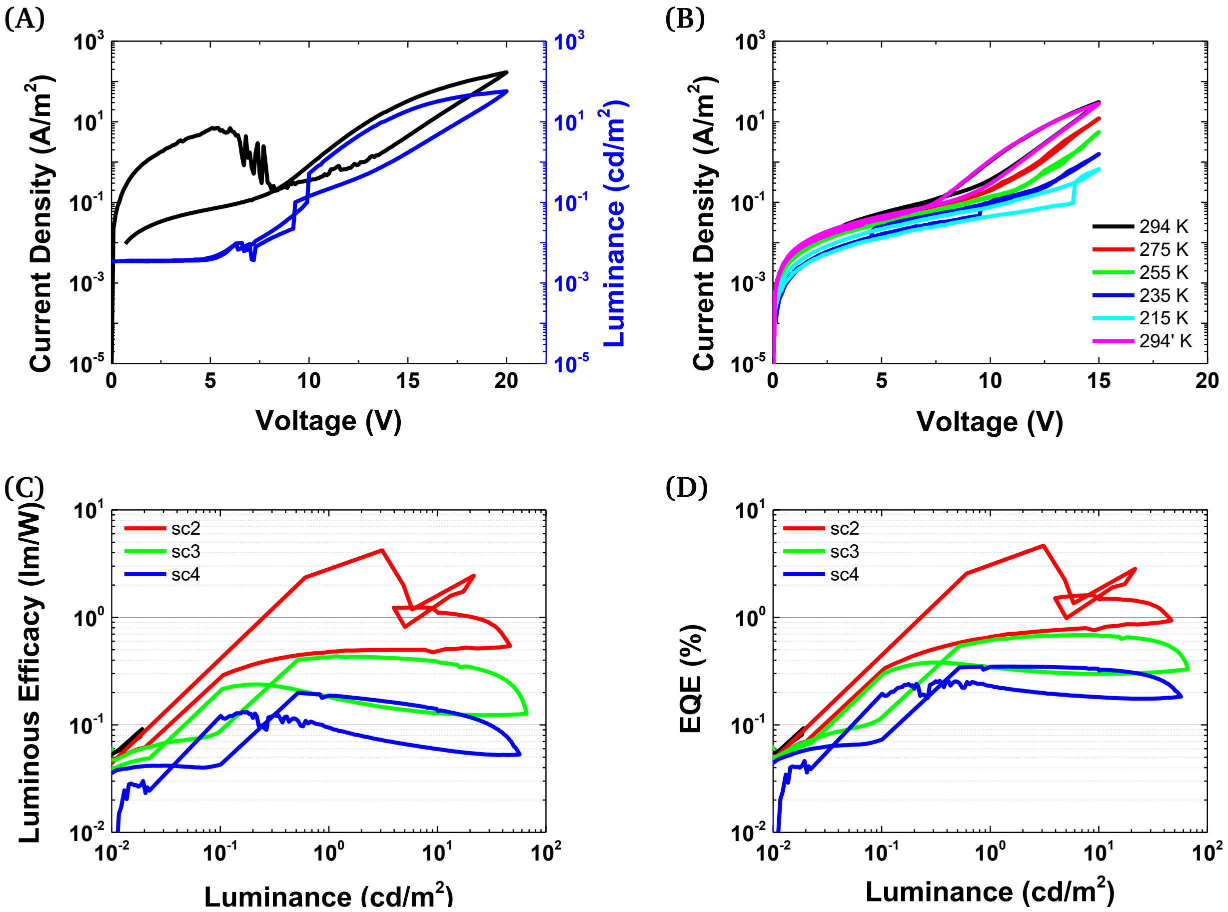

Figure 9.42: Photophysical results of a solution-processed organic light-emitting diode based on B-oTC (**8b**). **(A)** current density (black) and luminance (blue) at 20 V in one plot. **(B)** temperature dependence of current density at 15 V. Luminous efficacy **(C)** and external quantum efficiency **(D)** versus luminance.

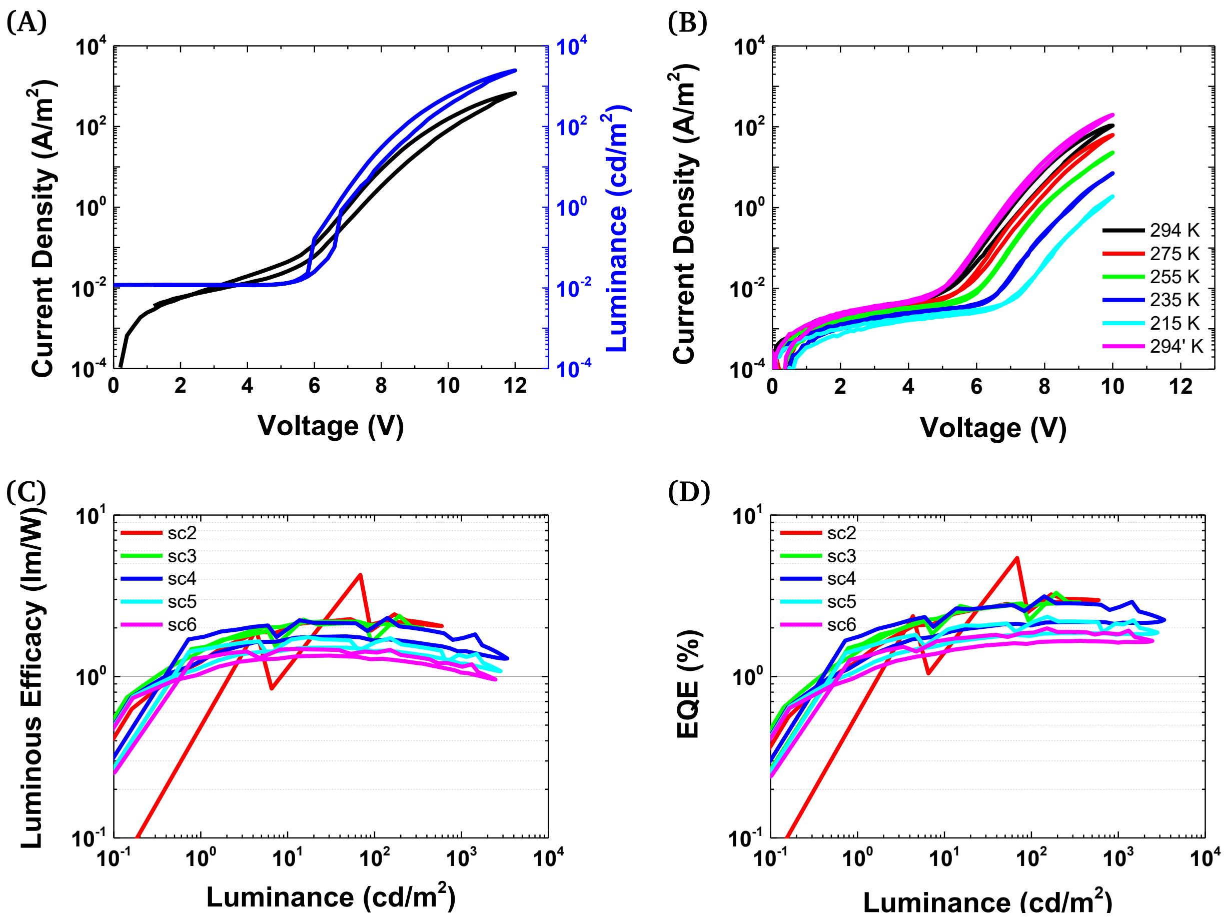

Figure 9.43: Photophysical results of a thermally-evaporated organic light-emitting diode based on B-oTC (**8b**). **(A)** current density (black) and luminance (blue) at 12 V in one plot. (**B**) temperature dependence of current density at 10 V. Luminous efficacy **(C)** and external quantum efficiency **(D)** versus luminance.

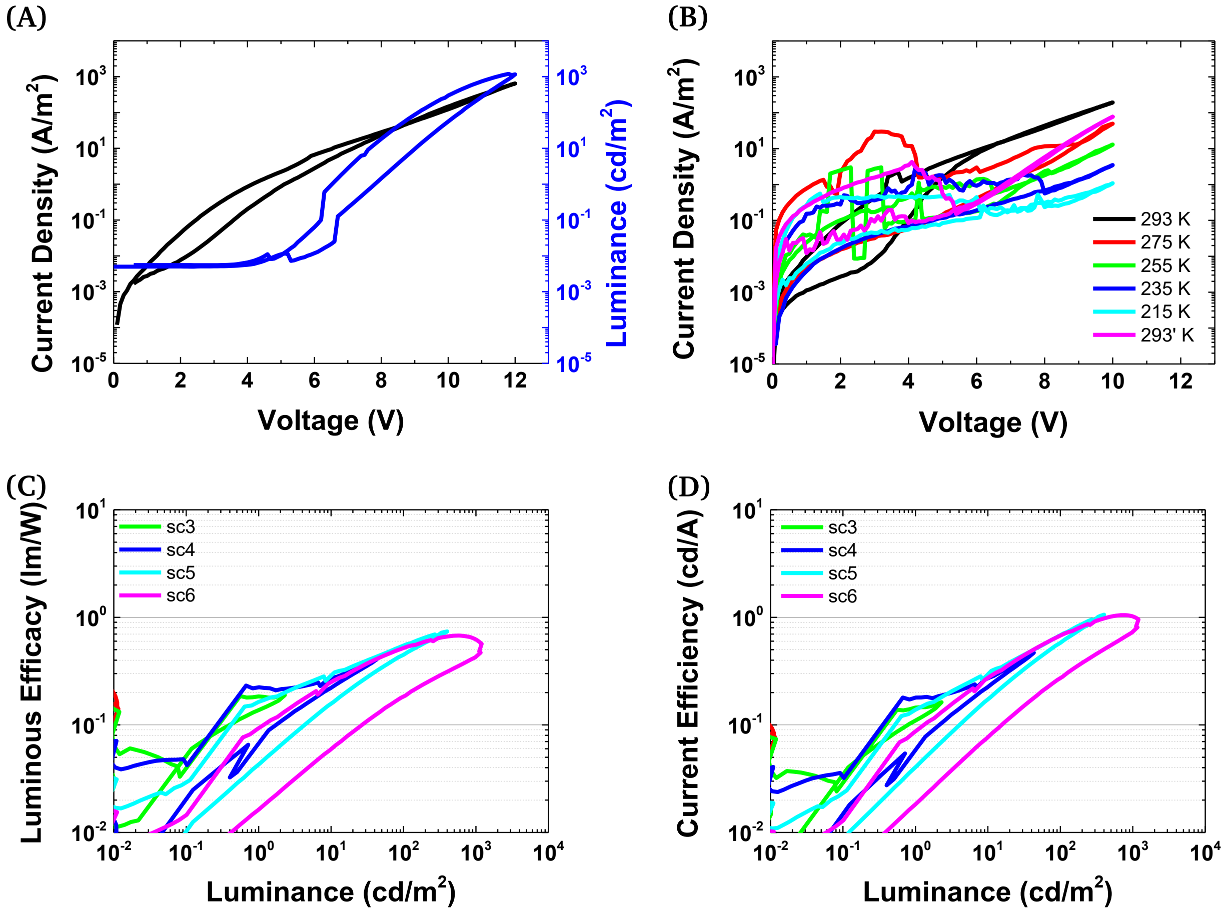

Figure 9.44: Photophysical results of a thermally-evaporated organic light-emitting diode based on B-oTC (**8b**). **(A)** current density (black) and luminance (blue) at 12 V in one plot. **(B)** temperature dependence of current density at 10 V. Luminous efficacy **(C)** and external quantum efficiency **(D)** versus luminance.